Universidad Autónoma de Madrid
Departmento de Física Teórica

METAL ENRICHMENT AND COOLING IN COSMOLOGICAL SIMULATIONS: A NEW PARALLEL CODE AND SOME APPLICATIONS

Memoria presentada por
Francisco Jesús Martínez Serrano
para optar al grado de
Doctor en Ciencias Físicas

Tesis dirigida por el Dr. Arturo Serna Ballester

co-dirigida por la Dra. Rosa Domínguez Tenreiro

9 de Septiembre de 2009

A mi familia.

We do not ask for what useful purpose the birds do sing, for song is their pleasure since they were created for singing. Similarly, we ought not to ask why the human mind troubles to fathom the secrets of the heavens. The diversity of the phenomena of nature is so great and the treasures hidden in the heavens so rich precisely in order that the human mind shall never be lacking in fresh nourishment.

Johannes Kepler

Agradecimientos

Dicen algunos que las tesis son como una aventura, se sabe donde empiezan pero nunca cómo van a acabar, tal es el carácter de la investigación original. No sé si esto es cierto para todo aquel que logra terminar una tesis (siempre hay personas mejor dotadas que otras para según qué tareas), pero en mi caso es cierto; más aún, se trata de una doble aventura, puesto que yo ni siquiera sabía dónde empezaba, no al menos hasta unos días antes de comenzar.

Ante tamaña acumulación de incertudumbre, cabe preguntarse qué serie de afortunadas coincidencias se han encadenado para que ahora estés leyendo estos mal embastados agradecimientos. La solución es fácil, no existe tal cadena de coincidencias, tan sólo una gran dosis de fortuna al comienzo de la aventura, la que me situó rodeado de gente con ganas de hacer cosas, además de con capacidad y con conocimentos para llevar la aventura a buen puerto, gente que además me brindó amistad y compañía durante el trayecto, gente a la que tengo mucho que agradecer[1]. A partir de ese momento, todo fue coser y cantar (con algún inevitable sobresalto, pero ¡qué monótona sería de la vida sin sorpresas!).

Decíamos que hasta unos días antes de comenzar no sabía por dónde iba a empezar. Esto no es del todo cierto: ¡ni siquiera sospechaba que iba a comenzar! Fue mi director, Arturo Serna, quien que me contactó y me ofreció realizar una tesis en una materia tan extraña para mí por aquel entonces como la Astrofísica. Andaba yo finiquitando los últimos exámenes de Ingeniería Industrial cuando vi en la puerta de mi clase un anuncio ofertando la realización de una tesis en la U.M.H. sobre simulaciones de formación de galaxias.

Personalmente siempre me había interesado la Física, en gran parte por culpa de mi padre, que ya estaba interesado en ella antes de nacer yo, y me inculcó el gusanillo de la curiosidad por el funcionamiento de las cosas a nivel fundamental desde bien pequeño. Prueba de ello es que por aquel entonces ya andaba estudiando Física en los ratos libres, tratando (y no siempre consiguiendo) de compaginar dichos estudios con los de Ingeniería. Dado este sustrato, la oferta resultaba extremadamente tentadora, y no tardé en ponerme en contacto con Arturo para aceptarla casi de inmediato.

A partir de aquí todo fue rodado, Arturo me prestó un libro titulado “Structure Formation in the Universe” de un tal Thanu Padmanabhan, yo lo leí del tirón, lo entendí todo a la primera, a pesar de no tener base en los temas allí tratados, y acto seguido me

[1]Ello explica lo extendido de estos agradecimientos, por los que pido disculpas de antemano.

puse a escribir la presente tesis, a la que doy paso sin mayor dilación.

Obviamente, el párrafo anterior es mentira. Y además de las gordas. Si bien Arturo me prestó el mencionado libro, lo cierto es que apenas entendí nada de lo que en él se hablaba. Tuvo Arturo en aquel momento el buen tino de sugerir que marchara durante aquel año a Madrid, a la Universidad Autónoma, a realizar allí los cursos de doctorado llamados "Astrofísica y Cosmología". Fue así como conocí a Rosa Domínguez, organizadora de los cursos, y en su día directora de la tesis de Arturo. Siendo como era la primera vez que yo iba a vivir fuera de mi ciudad, Rosa me abrió, literalmente, las puertas de Madrid y de su casa, y por ello siempre le estaré agradecido. En Madrid tuve la fortuna de conocer a numerosos profesionales de este oficio que nos enseñaron a mis compañeros y a mí lo amplio y maravilloso de la astrofísica, la multitud y riqueza de los fenómenos que en ella se tratan. Aún a riesgo de dejarme a alguien en el tintero mencionaré a Mercedes Mollá y Ángeles Díaz, que nos mostraron lo complejo y variado de las galaxias y los procesos que en ellas ocurren; Rosa y Gustavo Yepes, que trataron de desentrañar los misterios de la formación de estructuras y su estudio mediante simulaciones; Fernando Atrio y David Valls que ahondaron en los misterios y paradojas de la cosmología; y Enrique Pérez, Valentín Bujarrabal y José Cernicharo que abrieron un (al menos para mí) nuevo campo al mostrar la complejidad de los fenómenos que ocurren en el medio interestelar. Todos ellos nos hicieron trabajar duro con el objetivo de que entendiéramos un poco de lo que trataban de explicar con la mejor de sus voluntades.

Aunque los profesores fueron importantes, más lo fueron los compañeros. Fue durante y alrededor de estas clases donde conocí a los que iban a ser mis compañeros de aventuras y desventuras en los próximos años, Mariluz, Mariano, Jose y Héctor, me acompañaron y brindaron su amistad a lo largo de aquel curso. Especialmente Jose y Héctor, con los que comparto co-directora de tesis, me enseñaron no sólo buena parte de lo que sé de astrofísica y computación, sino también y más importante, lecciones de compañerismo y amistad que nunca olvidaré. También, por qué no decirlo, a tratar con todos esos problemas de carácter más mundano y/o burocráctico y a mirar las cosas con más calma. Con ellos he trabajado codo con codo (o al pie del email y el teléfono) para llevar a buen puerto nuestras aventuras. También Mariola, avezada y brillante sucesora, que tiene la no fácil tarea de mantener el negocio funcionando.

A la vuelta de Madrid (y brevemente antes de ir) compartí despacho en Elche con Chus, cuya perseverancia y el amor por la astrofísica siempre me ha inspirado a seguir hacia adelante. La vuelta marcó el verdadero comienzo del desarrollo del presente trabajo, en el que Arturo ha colaborado tanto y del que es parte tan integral, que lo cierto es que no sé por dónde comenzar a agradecer. Suya y de Rosa es la idea de implementar la química

en DEVA, núcleo central de esta tesis, y suya es una primera implementación que me fue de gran ayuda para tener un punto de comienzo e inspiración para desarrollar el modelo aquí descrito. Buena parte del trabajo de paralelización del código fue desarrollado por él mismo y en todas partes ha colaborado con certero y presto consejo y buenas ideas siempre que han sido necesarios. Todo ello sin restar un ápice de libertad y flexibilidad en ningún momento, más bien al contrario, puesto que me ha brindado el tiempo y el espacio necesarios para probar todas las ideas que se me iban ocurriendo, dando siempre consejo y apoyo. Algunas de estas ideas, en principio un poco descabelladas, han acabado formando parte integral de la presente tesis, otras no fructificaron, pero Arturo siempre estuvo ahí regalando libertad, apoyo y consejo.

El otro gran pilar del presente trabajo es Rosa, cuya incansable dedicación a la investigación y gran exigencia para consigo y los demás siempre me ha impulsado a ir un paso más allá en la realización de todas las partes de la tesis. Sin sus aportaciones en forma de ideas originales, correcciones y consejos experimentados esta tesis probablemente sería muy diferente o no sería.

Otra persona que ha colaborado de forma particularmente importante es Mercedes Mollá, que además de explicar de forma muy instructiva la evolución química durante los cursos de galaxias, ha ayudado con sus códigos, su tiempo y su paciencia a implementar el modelo de evolución química explicado en este trabajo.

Durante el viaje que ha representado esta tesis he tenido la fortuna de conocer a gente muy interesante y especial, algunos de los cuales pasaron por mi vida y se fueron y otros que llegaron para quedarse. Aparte de los ya mencionados, no puedo olvidarme de María y Mariola, que hacen más llevaderas las horas en la U.M.H.; Javi, Vero, Jose e Irene, siempre dispuestos a subirse a cualquier pared o ir a cualquier fiesta; Viví, que siempre me acompaña, y otros tantos que me estaré dejando en el tintero. También la gente que conocí en Potsdam, durante una estancia que sacudió muchas cosas en mi cabeza: Alex, que me acogió allí; Jochen, Steffen, Christian y Juan Carlos, en cuya compañía pasé numerosas horas de trabajo y esparcimiento; Kristin, Manenee, Timur, Heike, Rob, Franziska, Gabi y tantos otros buenos compañeros. Mención especial de parte de mi corazón para Dasha, lo mejor de Potsdam. Del mismo modo, agradecer a los que siempre han estado y estarán ahí, encabezados por mi familia (a la cual esta tesis va dedicada), Leoncio, Antonia y María José, además de todos mis tíos, primos y abuelos, alguno de los cuales estaba a mi lado al comienzo de esta tesis y ahora va siempre comigo. También David M., Josegas, José Luis C., Álex y María, Pablo L., Pablo G., Pedro, David B., Víctor, Marian, y la gente de siempre, ellos saben quienes

son.

Contents

List of Figures

List of Tables

Chapter 1

Introduction

> The wind is never favorable to those
> who don't know where they are going
>
> Seneca minor

1.1 Theoretical and observational framework

Extragalactic astronomy has come a long way since spiral nebulae were definitely recognised as independent galaxies in the 1920s (*e.g.* Curtis, 1920). Fifty years later, the presence of a hierarchical clustering of matter in the universe spanning several orders of magnitude in mass, was already well recognised (Press & Schechter, 1974). Currently the hierarchical structure is well established by systematic surveys such as 2dF or SDSS. In this hierarchical structure, galaxies remain as the main building block of the universe, spanning a range of $\sim 10^8 - 10^{13} M_\odot$ in stellar mass. Within this mass range there is a broad variety of morphological types, ranging from low surface luminosity dwarfs to giant ellipticals and passing through irregular or grand-design spiral galaxies. What happened during those fifty years?

The astronomical discovery of a plethora of galaxy types during the last decades was performed in parallel to the development of cosmology. Starting with Hubble's publication of his eponymous law (Hubble, 1929), the cosmological theories of Friedman (1922) and Lemaître (1927) found strong support, and the expansion of the universe was established[1]. From this point two alternative theories emerged as the main candidates to

[1] Although Hubble's value of the expansion rate of the universe was overestimated by almost a factor 7 due to the small size of his sample of galaxies, the confirmation of the expansion of the universe remains of capital importance. It was not until Sandage (1968) that an accurate value for the expansion rate of the universe was given.

explain the expansion of the universe: on one side the model of Lemaître (1927), with the universe starting from a hotter and denser state and expanding with a constant amount of matter; on the other side Hoyle (1948) (among others) introduced the possibility that the universe is in a steady state, with matter being constantly created and thus keeping the density constant withing an expanding universe. In the same year, Alpher, Bethe & Gamow (1948) presented their theory of the origin of the chemical elements. This theory, also known as Big-Bang nucleosynthesis, is based upon Lemaître's work and gives accurate predictions for the primordial abundances of hydrogen and helium[2]; it is so far one of the most accurate predictions of the Big-Bang theory. The last "nail in the coffin" for steady state theory was put by the discovery (Penzias & Wilson, 1965) of the cosmic microwave background (CMB), a relic radiation from the hotter past of our universe. This radiation had already been predicted by Alpher & Herman (1949), and it signaled the definitive settlement of the hot Big-Bang hypothesis as the standard cosmological theory.

Possibly, the next milestone in the development of the current standard cosmological model happened in the 1970s, with the proliferation of signs that pointed towards the existence of more matter in galaxies and clusters than was observed with telescopes. It was already in the 1930s when Zwicky (1933) pointed towards the large velocity dispersion of galaxies in the Coma cluster, a fact that could only be accounted for by the presence of more matter than was visible if the system was virialised. Smith (1936) made similar remarks for the Virgo cluster, and six years after Zwicky's paper, Bowen & Wyse (1939) obtained the rotation curve of the Andromeda galaxy, which showed that the outer regions of M31 were rotating with an unexpectedly high velocity, indicating either a high outer mass-to-light ratio or strong dust absorption.

These signs of the presence of additional mass or a very high M/L ratio in the outer part of disk galaxies remained unexplained until more than thirty years later, when Ostriker & Peebles (1973) openly spoke of the need for a very massive dark halo in disk galaxies in order for cold disks to be stable. Notably, this result was obtained by means of N-body simulations, one of the subjects of this Thesis. By 1975 the majority of astronomers were already convinced that missing mass existed in cosmologically

[2]Although the original paper also tried to give a cosmological origin for the abundance of all the elements, the theory was later refined to explain the cosmic origin of isotopes until ^{7}Li only. The origin of the rest of the elements was later recognised to have stellar origin only, as Bethe (1939) had explained. Interestingly Bethe did not contribute to the Alpher et al. (1948) paper and was included as an author only for alphabetical reasons.

significant amounts (van den Bergh, 1999). This does not mean that the existence of dark matter was unanimously accepted by that time. To this day there are proposed alternatives such as MOND (see Milgrom, 2008, for a recent review) or conformal gravity (Mannheim, 2006) that (according to some authors) work better at explaining the rotation curves of observed spiral galaxies. Both theories have covariant formulations and also have implications for the cosmological model.

Another important development of the 1970s is the Zel'dovich (1970) theory (see Shandarin & Sunyaev, 2009, for a comment on the paper) of non-linear evolution of perturbations in the early universe. This first-order lagrangian approximation allowed for the first time to devise an extension of the linear theory for the growth of perturbations, transforming the power spectrum given by linear theory into a real-space density (or particle) distribution. This introduced for the first time the concept of a cosmic web, where pancakes are first formed and then collapse into filaments. The hypothesis was confirmed in the 1980s with galaxy surveys such as the CfA survey (Davis et al., 1982). Zel'dovich theory is also specially relevant for N-body simulations. The approximation devised in his work is routinely used to generate initial conditions from an initial spectrum of perturbations derived from the cosmological model.

The next big development in cosmology is more recent and has come to be termed as "precision cosmology"[3]. Starting with the COBE determination of the existence of anisotropies in the CMB (Smoot et al., 1992), the anisotropies, together with data from distant type Ia supernovae and recent galaxy surveys such as 2dF (Peacock et al., 2001) or SDSS (Abazajian et al., 2003) have been analysed to obtain the parameters of the cosmological model. These parameters have been later refined with the CMB observations performed by the WMAP satellite (Komatsu et al., 2009). The current errors stated for the cosmological parameters are very low when compared with the uncertainties for the same parameters in the mid 1990s. The study of the type Ia supernovae (Riess et al., 1998; Perlmutter et al., 1999), which can be considered as standard candles, allowed to measure the expansion rate of the universe and its derivative. This resulted in the surprising result that the universe expansion rate is accelerating. This has been interpreted as either (1) a cosmological constant (Λ), such as the one introduced by Einstein; (2) a fluid with negative ratio $w = p/\rho$ for the equation of state; (3) a "backreaction" from a lower than average local universe (Kolb et al., 2008); or (4) even a need for the modification of the Einstein equations at cosmological distances (Sotiriou & Faraoni, 2008; Mannheim, 2006).

[3]Note that precision does not imply accuracy.

Given the current estimates for the cosmological parameters, the mysterious fluid with negative w (also termed dark energy) would account for ~ 73 % of the energy in the universe ($\Omega_\Lambda \simeq 0.73$), and dark matter for ~ 23 % ($\Omega_c \simeq 0.23$), with ordinary baryonic matter accounting for only $4-5$ % ($\Omega_c \simeq 0.04$) of the matter and energy in the universe. Since the Ω_Λ and Ω_c terms are the most relevant, the standard cosmological model is commonly called ΛCDM, where CDM stands for Cold Dark Matter. Dark matter is assumed to be cold (*i.e.* moving at non-relativistic velocities), and currently the most important dark matter candidate particles (such as neutralinos) are believed to have a mass of at least $\gtrsim 100$ GeV (Battaglia et al., 2001). The cold hypothesis for the dark matter is however not well established, and it has problems at explaining the low number of satellites observed in the Milky Way, or the ubiquity of disk galaxies with small or no bulges. Alternatives such as Warm Dark Matter (WDM) (Bode et al., 2001) have been proposed, but these in turn have their own issues. Recent studies indicate that it may be possible to reconcile the missing satellite problem with the CDM hypothesis (Madau et al., 2008).

1.2 N-body cosmological simulations

N-body simulations are a very important tool for the study of the formation of cosmic structures and galaxies. The density fluctuations in the primordial universe grow until they become non-linear. At that point, only approximations can be made with analytical theory following the Zel'dovich (1970) approximation and trying to extend it in order to avoid the difficulties posed by shell-crossing (Gurbatov & Saichev, 1984; Vergassola et al., 1994; Domínguez, 2000). A more direct approach (albeit not exempt of pitfalls) relies on the explicit computation of the interaction between mass elements (or particles). Simulations thus can be regarded as a tool that converts basic cosmological theory into structures that are directly comparable with observations.

The first N-body simulation of interacting galaxies was performed even before digital computers were readily available. Holmberg (1941) used light bulbs with attached photocells in place of particles to derive the interaction strength between such elements[4] and manually integrated the forces to obtain the 2-D trajectories of the "particles".

The first computer N-body simulations were run in the 1960s (von Hoerner, 1960, 1963; Aarseth, 1963), albeit these were simulations of isolated systems with a hundred

[4]The device takes advantage of the fact that the radiation flux decays as $1/r^2$ as does the gravitational force.

of particles. The exponential increase in the density of transistors in integrated circuits (Moore, 1965) made possible an equally exponential increase in the number of particles that could be used in simulations. Already in 1974, Press & Schechter in their influential work, introduced their model of mass condensation and their derivation of their eponymous mass function using around a thousand mass elements. This work represents probably the first truly cosmological N-body simulation.

The field progressed rapidly from that point and several works studying the two-point correlation function of galaxies using simulations followed (Peebles & Groth, 1976; Fall, 1978; Efstathiou et al., 1979). From that moment, the techniques applied in order to solve the gravity equations became increasingly elaborate and direct summation methods were replaced by more elaborate grid methods. These require a computational effort that scales as $O(N \log(N))$ with the number of particles, instead of $O(N^2)$ for direct summation methods, only at the expense of small accuracy losses. The bump provided by these methods to the number particles available for a simulation effectively halves the e-folding time at which the number of particles in simulations increases over time due to Moore's law. The main methods are (in no particular order):

1. **Particle-Mesh (PM) methods**: These methods take advantage of the fast Poisson solvers that can be constructed using the FFT transform (Heideman et al., 1984; Cooley & Tukey, 1965) and is well described in Hockney & Eastwood (1981). They are very well suited to cosmological applications since the FFT transform automatically implies periodic conditions. They work by assigning the mass of the particles onto a regular mesh and solving the Poisson equation for the obtained density field in Fourier space. The computed force field is interpolated back to the particles. The basic PM method has the disadvantage of limiting the resolution to the size of cells in the mesh. This is solved by the Partice-Particle Particle-Mesh (P^3M) and the Adaptive P^3M (AP^3M) methods that use either a direct evaluation of the forces at the sub-mesh level (P^3M) or refinements where the PM method is applied recursively in order to obtain higher force resolution with less computational cost than a direct sum (AP^3M). Our implementation of a parallel version of the AP^3M method is described in Chapter 2.

2. **Barnes & Hut Tree method**: This method (Barnes & Hut, 1986) works by recursively partitioning the simulation box into a hierarchy of cells (the tree) with the leaf cells of the tree containing one or more particles. If a given cell of size s is at a distance d from the point where the gravitational field is to be computed,

and the angle $s/d < \theta$, where θ is the aperture criterion, then all the particles in that cell can be replaced by a pseudo-particle located at the center of the cell. The pseudo-particle is assumed to have monopolar, dipolar, quadrupolar, etc. terms, depending on the trade-off between precision and computational cost. θ also affects the precision: the smaller it is the less cells will be replaced by pseudo-particles. The original code was made publicly available by the authors and the method became rapidly popular. The algorithm has the advantage of naturally adapting to clustered distributions of matter such as the ones appearing in simulations of galaxy formation. However it has two main drawbacks: (1) it needs a relatively large amount of memory in order to build the tree and (2) unlike the PM method it needs a special treatment to be able to produce periodic conditions. Currently the most widely used implementation of this method is the Gadget-2 (or 3) code (Springel, 2005).

3. **Adaptive Mesh Refinement**: This family of methods are also based on solving the Poisson equation on a mesh. However, unlike P^3M or AP^3M they completely skip the particle-particle calculation and instead uses finer meshes. The gravity on the base mesh can be solved by means of either FFT methods (PM) or by relaxation methods. The base mesh is refined in high density regions forming a nested tree of grids. Gravity in these grids is solved by the relaxation method. Since this method uses only the grid to solve for gravitational forces, the effective resolution at any given point of the simulation box is set by the grid resolution and effectively changes from region to region of the box. Examples of implementations of this method include Jessop et al. (1994); Suisalu & Saar (1995); Gelato et al. (1997); Kravtsov et al. (1997); Knebe et al. (2001) and Knollmann & Knebe (2009).

1.2.1 Hydrodynamic forces: including the gas

Once the ever-increasing computational resources allowed for it, gas dynamics was included in cosmological simulations. Besides some one-dimensional first efforts to study the effects of gas and additional physics (such as cooling) in pancake formation (Shapiro et al., 1983; Bond et al., 1984; Shapiro & Struck-Marcell, 1985), the first true three-dimensional cosmological simulations including the effects of gas dynamics were performed by Evrard (1988) and Hernquist & Katz (1989) using the smoothed particle hydrodynamics (SPH) technique. This lagrangian algorithm was invented by Lucy (1977) and Gingold & Monaghan (1977) (for a review, see Monaghan, 1992). Shortly afterwards,

Ryu et al. (1990); Cen et al. (1990) and Yuan et al. (1991) used eulerian algorithms to perform cosmological simulations. Both methods have strengths and downsides, as we describe below.

1. **Smoothed particle hydrodynamics**: This method discretises the fluid equations using particles. Each particle is assumed to have a constant mass and samples the underlying density, velocity and internal energy (or entropy) fields. The values of any such field at a given point in space is computed by averaging over the values stored in the neighbouring particles, using a suitable smoothing kernel. Hydrodynamic forces on a given particle are likewise computed by averaging the effects of the interaction with each of its neighbours.

   The size of the kernel of each particle, or smoothing length, is changed in order to maintain approximately constant the number of neighbours. The resolution at each point is given by the smoothing length and thus adapts to the local density, with a constant mass resolution. The ability to put computational resources where the density is higher, together with the ease of implementation in N-body codes are the main strengths of this method.

   The downsides are mainly related to the smoothing procedure (Agertz et al., 2007; Tasker et al., 2008). Since the properties of the fluid are smoothed by the kernel, areas of discontinuity such as shocks provoked in mergers or Kelvin-Helmholtz and Rayleigh-Taylor dynamical instabilities appearing when a galaxy moves through the intracluster medium are smoothed over at least one kernel smoothing length. Since the size of the smoothing has an inferior limit due to time-stepping restrictions that would otherwise slow the simulation to a halt, the smoothing length effectively washes down the discontinuities and results in different physical results. There has been attempts at addressing this issue. For instance, Shapiro et al. (1996) introduce ASPH, a modification of SPH allowing for non-spherical kernels, in this method the smoothing length becomes a tensor and its changes are tracked in order to detect shocks; Monaghan (1997) develops a formalism that, albeit does not properly resolve the properties of shocks, accounts for their effects on the post-shock regions; Inutsuka (2002) uses a Riemann solver to reformulate the SPH equations; and Pfrommer et al. (2006) explicitly compute the dissipation in shocks and try to account for their effects.

2. **Eulerian methods**: These methods are based on a grid that does not move along with the fluid. The exchange of mass from each grid element to the next and

the fluid properties are obtained by means of a variety of methods and a detailed treatment of discontinuities is possible. Among the most common algorithms for solving the fluid equations are the piecewise linear or parabolic methods (Colella & Woodward, 1984; Leveque, 1992). This methods are respectively second or third order Godunov schemes that capture shocks efficiently using few cell elements.

While the strengths of eulerian methods are related to their shock-capturing abilities, which is the main downside of SPH, their downsides are related to the upsides of SPH. The resolution of eulerian methods is set by the grid size at each point, and unlike SPH, and it is the task of the programmer to ensure that there is high enough resolution in high-density regions. This implies that achieving the same dynamic range that SPH achieves requires more computing resources. Furthermore, as objects such as galaxies move along the box, the mesh structure has to be regenerated in order to track the movement of the object. Also, since the mesh is usually box-aligned, there are preferred directions that can introduce spurious effects in the flow properties.

Another downside is related precisely with the eulerian nature of the method. Since the mesh does not move along with the flow, these methods are not galilean invariant by definition, as SPH is. That means that the same process occurring at different velocities relative to the mesh in otherwise equal conditions will likely result in different outcomes.

Widely known examples of this kind of codes include ART (Kravtsov et al., 1997), FLASH (Fryxell et al., 2000), AMIGA (Knebe et al., 2001) or RAMSES (Teyssier, 2002).

Besides the two main methods briefly described above, there is the possibility of combining both methods by mean of a mesh that moves along with the fluid. This was tried early on by Gnedin (1995) or Pen (1995), but was found to have great mesh distortions that result in degenerate cells once the gravitational force made cosmological simulations highly clustered. These distorted cells introduce large errors in the fluid computation (Gnedin & Bertschinger, 1996). However Springel (2009) has recently introduced a new method that seems to achieve a moving mesh that adaptively follows the flow. He manages to avoid the downsides of mesh distortions by re-creating the mesh with a Voronoi tessellation scheme at each time-step.

1.2.2 Sub-grid physics: enabling galaxy formation

While gravity is the main driving force in the process of galaxy formation, and gas dynamics plays a very important role where densities are high (*i.e.* in collapsed regions such as filaments, clusters or galaxies), there are still ingredients remaining in order to be able to obtain galaxies in simulations with observational counterparts. There are a number of processes such as cooling, star formation, AGN feedback, radiative transfer or gas turbulence that influence the bulk dynamics of the gas happening at scales below the resolution currently achieved by cosmological simulations of galaxy formation. Of these processes cooling and star formation were the first ones to be included in simulations of galaxy formation. Cen et al. (1990), Katz & Gunn (1991) or Thomas & Couchman (1992) studied the cooling effects in simulations. These works already included the cooling of thin plasmas by means of a temperature-dependent cooling function, much in the way it is done today by several cosmological codes.

Once the gas is allowed to cool in a non-adiabatic way, gas particles lose pressure support and tend to collapse and form denser regions. If angular momentum conservation is guaranteed by the N-body code, the collapsed regions with high enough angular momentum will adopt the form of dense gas disks with rotational support. At this point star formation needs to be taken into account. Katz (1992) was the first to include a Schmidt-like law in a semi-cosmological simulation of disk galaxy formation. He took into account the dynamical and cooling time of a given gas particle in order to derive a star forming rate for each gas particle, mimicking the observed Schmidt law (Schmidt, 1959, 1963; Larson, 1969). Currently most codes include a similar prescription to form stars.

Once a star particle is formed, it decouples from the gas and becomes acollisional, in that way the process of star formation happening at sub-resolution scales, alters the dynamics of the gas. Star formation is known to have another effects through the feedback of enriched gas and energy by means of supernova blastwaves and winds. Beginning with Katz (1992) there has been a growing interest in including these sub-resolution effects into large-scale cosmological simulations and there is a long list of works that describe different such models (Cen & Ostriker, 1992; Navarro & White, 1993; Metzler & Evrard, 1994; Steinmetz & Muller, 1995; Yepes et al., 1997; Cen & Ostriker, 1999; Sommer-Larsen et al., 1999; Thacker & Couchman, 2001; Kay et al., 2002; Lia et al., 2002; Semelin & Combes, 2002; Marri & White, 2003; Sommer-Larsen et al., 2003; Springel & Hernquist, 2003; Kobayashi, 2004; Brook et al., 2004; Okamoto

et al., 2005; Oppenheimer & Davé, 2006; Stinson et al., 2006; Governato et al., 2007; Dalla Vecchia & Schaye, 2008; Dubois & Teyssier, 2008; Finlator & Davé, 2008; Scannapieco et al., 2008; Wiersma et al., 2009b). This is due to the fact that there is not a single correct way of implementing such effects. As many have said before, sub-resolution physics is both an art and a science. In Chapter 3 of this Thesis, we will introduce a new model for gas feedback and cooling that aims at including the effects of these two processes in the most precise way known to the authors without imposing a high toll in terms of computing time. We will also include a model for diffusion that mimics the redistribution of chemical elements by sub-resolution turbulence.

1.3 Structure of this work

In the second Chapter of this Thesis, we present the implementation of P-DEVA, a parallel version of DEVA (Serna et al., 2003), an AP^{3}M+SPH cosmological code that puts special emphasis on the conservation laws. The code has been parallelized with OpenMP directives and has already been used to run several large-scale simulations. The design decisions adopted when implementing the code are justified and benchmarks with up to 128 CPUs presented. In the third Chapter, we describe a new model for chemical evolution and cooling that, in the spirit of P-DEVA, tries to achieve a high precision in the treatment of such effects. To that end, the individual abundances of 15 elements are taken into account when computing the effects of stellar evolution and cooling. Several tests of the validity of the implementation are also presented. In the fourth Chapter we use the implemented parallel code, together with the model for chemical evolution and cooling, in order to study the process of disk galaxy formation by means of high-resolution simulations. Realistic disks are obtained with rather small bulges. The disks are found to have broken luminosity profiles in agreement with observations. We use the simulations to study the origin of such profiles.

Chapter 2

P-DEVA: A Parallel Code for Cosmological Simulations

> Give me a place to stand, and I shall move the world
>
> ARCHIMEDES

2.1 Introduction

Cosmological simulations have become a fundamental tool to learn how galaxies form from the field of primordial fluctuations and evolve into the objects we observe today. This problem represents a numerical challenge because the attractive nature of gravitational forces leads to structures with extreme density contrasts: from almost void regions to galactic substructures many orders of magnitude more dense. Cosmological codes must be then able to handle, with reasonable computing times and memory requirements, a very wide dynamical range with enough mass, time and space resolution. However, the speed of the codes must reach a critical compromise with the accuracy and reliability of their results. Conservation laws must be accurately verified, particularly the angular momentum at the scales relevant to disc formation and the entropy of reversible adiabatic processes. Otherwise, galaxy disc formation could meet with some difficulties and spurious effects could appear at galaxy scales.

Presently, there exist a wide variety of both adaptive Eulerian (e.g., Norman & Bryan, 1999; Klein et al., 1999; Kravtsov, 1999; Fryxell et al., 2000; Knebe et al., 2001; Teyssier, 2002; O'Shea et al., 2004) and Lagrangian (e.g., Couchman et al., 1995; Wadsley et al., 2004; Springel, 2005; Wetzstein et al., 2008) codes using different solvers for gravity and hydrodynamics. Both kinds of codes lead to consistent results and comparable performances (Kang et al., 1994; Frenk et al., 1999; Knebe et al., 2000; Tasker et al., 2008).

Lagrangian codes have nevertheless the advantage that they are inherently adaptive and do not require the complex implementation of adaptive Eulerian methods. Furthermore, in problems where orbit crossing occurs, as in galaxy formation and evolution, the tracking of mass inherent to Lagrangian codes easily permits to identify at different redshifts the constituent particles of a given object.

DEVA (Serna et al., 2003) is a Lagrangian code for both cosmological and isolated simulations of structure formation. In this code, gravitational forces are computed by using the AP^3M (Adaptive Particle-Particle, Particle-Mesh) algorithm proposed by Couchman (1991), while hydrodynamical processes are evaluated through the SPH (Smooth Particle Hydrodynamics) technique (Lucy, 1977; Gingold & Monaghan, 1977; Monaghan, 1992). Some differences with respect to other codes based on the same techniques are: 1) It uses an individual integration timestep for each particle. This is a very convenient feature to avoid a possible slow down of cosmological simulations, where very large density contrasts appear, and particles in denser volumes need to be updated with a frequency much higher than in rarified zones; 2) In spite that some loops over particles need to be evaluated twice, and that additional terms must be included in the evolution equations, DEVA is intrinsically constructed to satisfy the conservation laws, particularly angular momentum and the entropy of reversible adiabatic processes. An accurate conservation of such quantities is needed to simulate the formation of galaxy disks and avoid spurious effects at galaxy scales (see Serna et al., 2003, for a detailed discussion of such effects).

Due to the need of codes with a very high efficiency, much effort is now devoted in cosmology to parallel computing. Such a need comes from different aspects (Thacker & Couchman, 2006). Firstly, the desire to complete simulations in the shortest possible time to enable rapid progress. Secondly, the need of simulations with the highest possible resolution, able to simultaneously reproduce the growth of structure on the largest and smallest cosmological scales implied by the hierarchical CDM model. Finally, high resolution is also needed to make low-variance statistical predictions in simulations with the largest possible volume.

The only AP^3M-SPH code with parallel versions previously reported in the literature is Hydra (Couchman et al., 1995). Pearce & Couchman (1997) have discussed the parallelization of this code using a programming methodology specific of the Cray T3D. A portable parallel version of hydra using OpenMP has been also described (Thacker & Couchman, 2006), as well as the first steps towards another version using MPI (Pringle et al., 2001; Thacker, 2003). A much wider literature exists on data-parallel versions of SPH codes with other gravity solvers. This is the case of Tree-SPH (e.g. Antonioletti

et al., 1994; Dave et al., 1997; Lia & Carraro, 2001; Borgani et al., 2002), TreePM-SPH and GRAPE-SPH (e.g. Nakasato et al., 1997) codes.

Due to their limited expansion capacity, the present multi-processor servers with shared memory cannot compete for the largest simulations with massively parallel machines of distributed memory. However, there is a trade-off between science accomplishment and development time that must be also considered. The effort in developing a code for distributed-memory machines can be enormous for complex codes. Indeed, in multi-part solvers like an AP^{3}M-SPH code, an optimal load balance requires different data topologies and parallelization strategies at different stages of each integration step. Subtle communication patterns between processors must be also taken into account to reach a good efficiency in massively parallel environments. Such an effort is probably not justified in simulations with a modest number of particles, as well as in the modeling of isolated galaxies, where the practical limit of scalability appears to be of a few ten processors (Thacker & Couchman, 2006). In these cases, shared-memory multiprocessor servers arise as highly productive computing environments. Their ease to use and programming renders them an excellent tool for conducting simulations requiring significantly more computational power than that available from a single workstation.

The chapter is organized as follows: After a brief overview of P-DEVA in §2.2, we discuss in §2.3 the memory hierarchy in NUMA systems and how particle reordering can be used to improve data locality and cache reuse on these machines. Our time-symmetric PEC (Predict-Evaluate-Correct) integrator with individual time steps is then presented in §2.4, while the parallel implementation of the AP^{3}M and SPH methods are described in §2.5 and §2.6, respectively. Section 2.7 presents the results of some tests to check the performance and correctness of our code, while conclusions and the main features of our code are finally summarized in §2.8

2.2 Implemented Physics

The fundamental approach of cosmological simulations is to study the formation of cosmic structures by just using simple physical principles. To that end, initial conditions are set at high z as a Montecarlo realization of the field of primordial fluctuations in a periodic homogeneously sampled box. Then, the evolution of these fluctuations is numerically followed up to $z = 0$ by solving a set of basic equations that describe the dynamics of a collisionless component (dark matter and stars) and of a dissipative baryonic gas. All these components, represented by discrete numbers of particles, are

coupled by gravity and subject to an expanding background space.

We will now briefly summarize the basic set of equations, as well as the methods used in P-DEVA to solve such equations.

2.2.1 Gravity

Gravity is the key driving force for all the particle types involved in cosmological simulations. Indeed, the motion equation of any dark matter and star particle, i, is:

$$\frac{d\mathbf{v}_i}{dt} = -\nabla\Phi_i \tag{2.1}$$

where the gravitational potential, Φ_i, is given by the Poisson equation

$$\nabla^2\Phi = 4\pi G\rho_{tot} \tag{2.2}$$

A popular scheme to solve equations (2.1) and (2.2) consists of separating the gravitational force into its short and long range components, i.e.,

$$\mathbf{F}_{grav} = \mathbf{F}_{short} + \mathbf{F}_{long}. \tag{2.3}$$

The long range gravitational force, $\mathbf{F}_{long}$, can be efficiently computed through the Particle-Mesh (PM) algorithm (see, e.g. Hockney & Eastwood, 1981). Such a method is based on the fact that, in the Fourier space, the Poisson equation writes:

$$\tilde{\phi}(\mathbf{k}) = \tilde{G}(\mathbf{k})\tilde{\rho}(\mathbf{k}) \tag{2.4}$$

where the tilde denotes the (fast) Fourier transform (FFT) of a quantity and $\tilde{G}(\mathbf{k})$ is an appropriate Green function. We use $\mathbf{k}$ to denote points in Fourier space and $\mathbf{n}$ points in real space, both spaces are discretized with L cells per side.

The PM method then consists in 1) obtaining the density field $\rho(\mathbf{n})$ on the mesh points, 2) computing its Fourier transform $\tilde{\rho}(\mathbf{k})$, 3) obtaining the transformed potential $\phi(\mathbf{k})$ from Eq. (2.4), and 4) computing the inverse FFT to obtain $\phi(\mathbf{n})$. Once found the mesh potential, its differentiation gives the force field on the mesh points, that can be interpolated to the particle positions to obtain the gravitational forces.

The short range gravitational force, $\mathbf{F}_{short}$, provides resolution at scales smaller than the cell size of the potential mesh. This short range component can be evaluated from different procedures such as *e.g.*, a direct particle-particle (PP) sum, or the Barnes & Hut (1986) tree code (this is the case of the TreePM codes developed by Bagla, 2002; Springel, 2005; Yoshikawa & Fukushige, 2005). The alternative provided by the AP^{3}M

method for the evaluation of the short range forces consists in a recursive application of the above PM scheme in dense regions, where the application of the PP method would be too expensive. In these regions a new mesh is created and the force field computed by means of the PM method. If there are still dense regions within the new mesh where a new application of the PM is advantageous, a finer mesh inside the new mesh is created and the PM method applied again. This is done recursively until a pre-defined maximum number of levels is reached. The PP forces are evaluated only at the finer level available for a given particle, thus greatly reducing the number of particle pairs that need to be evaluated.

2.2.2 Hydrodynamic equations

The motion of particle i is determined by the momentum and energy equations:

$$\frac{d\mathbf{v}_i}{dt} = \mathbf{a}_i^P + \mathbf{a}_i^{visc} - \nabla\Phi_i \tag{2.5}$$

$$\frac{du_i}{dt} = \frac{P_i}{\rho_i^2}\frac{d\rho_i}{dt} + \mathcal{H}_i \ , \tag{2.6}$$

where Φ_i is the local gravitational potential, $\mathbf{a}_i^P$ is the acceleration due to pressure forces, $\mathbf{a}_i^{visc}$ is the acceleration due to viscosity forces, u is the specific internal energy, $P = (\gamma - 1)\rho u$ is the pressure (with γ being the constant heat ratio), and $\mathcal{H}_i$ is the power due to non-adiabatic heating or cooling processes.

In the SPH method (Lucy, 1977; Gingold & Monaghan, 1977), the gas density at the position of particle i is computed by convolving with a kernel function W that smooths out local statistical fluctuations

$$\rho(\mathbf{r}_i) = \sum_{j=1}^{N_g} m_j W(r_{ij}, h_i, h_j) \ , \tag{2.7}$$

where $r_{ij} = \mid \mathbf{r}_i - \mathbf{r}_j \mid$, m_j is the mass of particle j, and h_k is the smoothing length for particle k, which specifies the size of the averaging volume.

Ideally, the individual particle smoothing lengths h_k must be updated so that each particle has a constant number of neighbours N_S. By neighbours we mean those particles j with distances $r_{kj} \leq 2h_k$. Such a condition can be exactly implemented by constructing, for each particle k, a list of its N_S nearest neighbours. The most distant particle k_f in this list will define the smoothing length of k: $h_k = r_{kk_f}/2$. Such a procedure introduces however a numerical noise that can be reduced (Nelson & Papaloizou, 1994)

by computing h_k as the average distance of N_f most distant neighbours of k:

$$h_k = \frac{1}{2N_f} \sum_{k_f}^{N_f} \mid \mathbf{r}_k - \mathbf{r}_{k_f} \mid , \tag{2.8}$$

Since each particle has its own h value, it is possible to find couples of particles (j, k) such that j is a neighbour of k, but k is not a neighbour of j. In these cases, it is obvious that the reciprocity principle is not satisfied and, therefore, simulations will not conserve momentum. In order to solve this problem, it is necessary to symmetrize the SPH equations by using, for example, averaged kernels (Hernquist & Katz, 1989):

$$W_{ij} \equiv W(r_{ij}, h_i, h_j) = \frac{1}{2} \left[W(r_{ij}, h_i) + W(r_{ij}, h_j) \right] . \tag{2.9}$$

A first consequence of the adopted symmetrization procedure is the specific form for the kernel derivatives. As a matter of fact, Eq. (2.9) implies that W_{ij} is a function of three variables: r_{ij}, h_i and h_j. Consequently, its gradient $\nabla_i W_{jk}$ is given by:

$$\begin{aligned} \nabla_i W_{jk} = & \frac{1}{2} \left[\left(\frac{\partial W(r_{jk}, h_j)}{\partial r_{jk}} + \frac{\partial W(r_{jk}, h_k)}{\partial r_{jk}} \right) \nabla_i r_{jk} \right] \\ & + \frac{1}{2} \left[\frac{\partial W(r_{jk}, h_j)}{\partial h_j} \nabla_i h_j + \frac{\partial W(r_{jk}, h_k)}{\partial h_k} \nabla_i h_k \right] \end{aligned} \tag{2.10}$$

The first part of Eq. (2.10), which does not involve derivatives of the smoothing lengths, is the usual symmetrized form of $\nabla_i W_{jk}$. The second part, which involves derivatives of the smoothing lengths, arises because of the spatial and temporal variability of h. We shall refer to terms of this type as "∇h terms". Most implementations of the SPH algorithm consider only the first one and neglect the ∇h terms.

A fully consistent SPH expression for pressure forces, satisfying all conservations laws (including entropy conservation in reversible adiabatic problems), was obtained by Nelson & Papaloizou (1993, 1994):

$$\mathbf{F}_i^P = - \sum_j m_j \frac{P_j}{\rho_i^2} \nabla_i \rho_j . \tag{2.11}$$

Using Eqs. (2.7) and (2.10) to compute $\nabla_i \rho_j$, one obtains

$$\begin{aligned} \mathbf{a}_i^P = & - \sum_j m_j \left(\frac{P_i}{\rho_i^2} + \frac{P_j}{\rho_j^2} \right) \left[\frac{\partial W(r_{ij}, h_i, h_f)}{\partial r_{ij}} \right] \frac{\mathbf{r}_{ij}}{r_{ij}} \\ & - \Re_i \Psi_i - \sum_j \delta_{ij_f} \frac{\mathbf{r}_{ij}}{r_{ij}} \frac{m_j}{m_i} \Psi_j \end{aligned} \tag{2.12}$$

where

$$\Re_k \equiv \sum_{k_f}^{N_f} \frac{\mathbf{r}_{kk_f}}{r_{kk_f}} \tag{2.13}$$

$$\Psi_k = \frac{1}{4N_f} \sum_k m_f \left(\frac{P_k}{\rho_k^2} + \frac{P_j}{\rho_j^2} \right) \frac{\partial W(r_{jk}, h_j)}{\partial h_j} \tag{2.14}$$

and $\delta_{ij_f} = 1$ (if i is one of the N_f most distant neighbours of j) or 0 (otherwise).

On the other hand, using Eqs. (2.7) and (2.10) to compute the $d\rho_i/dt$ derivative appearing in Eq. (2.6), the energy equation becomes:

$$\begin{aligned} \frac{du_i}{dt} &= \frac{P_i}{\rho_i^2} \sum_j m_k \left[\frac{\partial W(r_{ij}, h_i, h_j)}{\partial r_{ij}} \right] \frac{\mathbf{r}_{ij} \cdot \mathbf{v}_{ij}}{r_{ij}} \\ &+ \frac{P_i}{\rho_i^2} \sum_j m_j \left[\frac{\partial W(r_{ij}, h_i)}{\partial h_i} \breve{r}_i + \frac{\partial W(r_{ij}, h_j)}{\partial h_j} \breve{r}_j \right] \\ &+ \mathcal{H}_i \, , \end{aligned} \tag{2.15}$$

where

$$\breve{r}_k \equiv \frac{1}{4N_f} \sum_{k_f}^{N_f} \frac{\mathbf{r}_{kk_f} \cdot \mathbf{v}_{kk_f}}{r_{kk_f}} \, . \tag{2.16}$$

As usual in SPH, to account for dissipation at shocks, the above equations must be completed by adding an artificial viscous pressure term, Π_{ij}. When the ∇h terms are considered, Π_{ij} is added only to the leading term of equations (2.12) and (2.15), that is, those not involving ∇h terms (Nelson & Papaloizou, 1994):

$$\frac{P_i}{\rho_i^2} \rightarrow \frac{P_i}{\rho_i^2} + \frac{\Pi_{ij}}{2}, \qquad \frac{P_i}{\rho_i^2} + \frac{P_j}{\rho_j^2} \rightarrow \frac{P_i}{\rho_i^2} + \frac{P_j}{\rho_j^2} + \Pi_{ij} \, , \tag{2.17}$$

where we have adopted the standard viscous pressure proposed by Monaghan & Gingold (1983):

$$\Pi_{ij} = \frac{-\alpha \mu_{ij} \overline{c}_{ij} + \beta \mu_{ij}^2}{\overline{\rho}_{ij}} \, , \tag{2.18}$$

where α and β are constant parameters of order unity, c_i is the local sound speed,

$$\mu_{ij} = \begin{cases} \frac{\mathbf{v}_{ij} \mathbf{r}_{ij}}{h_{ij} \left(r_{ij}^2 / h_{ij}^2 + \eta^2 \right)} & \mathbf{v}_{ij} \mathbf{r}_{ij} < 0 \\ 0 & \mathbf{v}_{ij} \mathbf{r}_{ij} \geq 0 \end{cases} \, . \tag{2.19}$$

and η^2 is a softening parameter to prevent numerical divergences,

2.3 Improving performance by data reordering

2.3.1 Memory Hierarchy in NUMA systems

The memory in modern multiprocessor computers is usually partitioned into interconnected modules, each comprised of one or more CPUs and memory. A CPU has high speed access to the memory located in its node, its local memory. More distant modules can be transparently accessed by any processor, meaning that no special communication instructions must be issued. The memory in all nodes then constitutes a logical global memory, but access is significantly slower for non-local memory (measured both by latency and bandwidth). These systems are termed Non-Uniform Memory Architectures, or NUMA.

NUMA systems can deliver high performance for multi-threaded applications provided that the computations carried out by each processor use data which are placed in its local memory. Otherwise, the resulting codes have a suboptimal performance, since they spend most of the time cycling idle waiting from remote data to be fetched, or the caches synchronised and their scaling becomes clearly unsatisfactory. Data locality and minimization of the rate of remote memory accesses are then critical for sustaining high performance on NUMA systems. Unfortunately, the standard OpenMP application programming interface (API) for multi-threaded applications provides no explicit means to the programmer for controlling the distribution of data among processing nodes. Since OpenMP is becoming the *de facto* standard for high-performance parallel programming on shared memory multiprocessors, some vendors have seriously considered the incorporation of data distribution facilities in their compilers. However, such facilities are not still standard and a certain controversy exists on either implementing them as high-performance Fortran-like extensions of OpenMP (Bircsak et al., 2000), as an independent user-level page migration environment (Nikolopoulos et al., 2000), or as additional system calls which are non standard (Löf & Holmgren, 2005). As a consequence, the inclusion of such facilities presently limits the portability of codes.

A widely used alternative strategy (see, e.g. Hu et al., 2000; Nikolopoulos et al., 2003; Thacker & Couchman, 2006) is the combined use of a first-touch placement policy with either data or computation reordering. In modern NUMA-aware operating systems, the default algorithm for allocating memory follows a 'first-touch' policy: a given page of memory will be allocated in the local memory of the first processor to access it. This policy is based on the assumption that the most frequent user of a memory page is the thread that first touches its data. The first-touch placement policy provides an elegant

way of mapping data to processors. If each processor touches first the data that we wish to map to it, the desired data distribution is performed implicitly and transparently to the programmer. In principle, this is possible by rewriting the loop so that it iterates over the processor number and the innermost iterations touch the data that we want to assign to each processor. The important limitation of this scheme is that the data assigned to each processor should be page aligned. If not, it is likely that processors will map locally pages with significant amounts of data that "belong", to other processors. As a consequence, false sharing will occur, the number of remote memory accesses will be increased and the program might suffer from high waiting times in the memory system. In many practical cases, this problem can be circumvented by padding certain array dimensions, or by adding one dimension (the processor number dimension) to the array, a transformation known as array reshaping.

2.3.2 Particle reordering and space-filling curves

In irregular applications, like N-body simulation codes, the optimal distribution of data among processors changes in different parts of the code and/or in different simulation steps. Since the first-touch distribution of data is carried out at the beginning of a simulation only, it becomes suboptimal as the code execution advances. Particle reordering then arises as an easy way of remapping the data to processors. The procedure (see Mellor-Crummey et al., 2001, for a brief review) consists in changing the order of elements within the particle information vector. In other words, if the first-touch placement policy assigned a block $i \in [i_1, i_2]$ of elements to a given processor, we can modify the particle identities to ensure that such a block corresponds to closely interacting particles. The idea is that if two particles are referenced near each other in time in the interaction list, they should be placed near each other in the particle information vector.

Data reordering requires a previous knowledge of the computation order, or interaction list. In N-body codes, this requirement is partially fulfilled by the fact most of the computing time is spent in the evaluation of short-range interaction. These interactions are produced by the neighbours of each particle and can be computed by considering a mesh with appropriate cell size: the short-range force on a given particle will be then produced by particles located in its 27 neighbouring cells only. Local interactions are then usually computed by performing a loop over cells, as well as an inner loop over the particles contained within each cell.

The loop over cells can be basically considered as a transformation that creates a linear ordering of the three-dimensional distribution of mesh cells. Figure 2.1 shows the

2D representation of three different ways of carrying out such a loop: the column major ordering, as well as the Morton and Peano-Hilbert space-filling curves (see, e.g. Hu et al., 2000). The former is the easiest to be implemented, while the Morton and Peano-Hilbert space-filling curves potentially result in better data locality (see, e.g., Butz, 1969; Bially, 1969; Hu & Johnsson, 1999, for different algorithms to achieve these curves). For any of these ordering methods, each particle position $\mathbf{r}_i$ must be converted into a position iboxp(i) on the space-filling curve. The particles are then sorted into ascending order by their position on the curve. Sorting particles into space-filling curves tends to increase spatial locality. Namely, if two particles are close together in physical space, then they tend to be nearby on the curve.

The Morton and Peano-Hilbert curves have the downside of being limited to mesh sizes that are a power of two. In order to ease the search of particles in the PP part of the code a searching mesh of size L_s is used. Since L_s is given by an error-limiting criterion for the forces, it need not be a power of two. To solve this problem, two alternatives have been explored:

1. to compute the smallest Morton or Peano-Hilbert curve (Moore, 2000) that entirely covers the searching mesh and then map the cells that are inside the searching mesh to a compact curve by means of a partition, following Shirokov (2005). This procedure results in regions that are not compact anymore near the borders of the searching mesh, and therefore memory access is slowed down for that regions. Furthermore, the compactification procedure adds a non-negligible overhead to the computation of the Peano-Hilbert curve.

2. to decrease L_s until it is a power of two, thus obtaining a coarser searching mesh, which increases the number of pairs of particles that are considered for evaluation and eventually discarded. Aside from the obvious downside of having a coarser searching mesh, this procedure has the advantage of requiring less evaluations of the Peano-Hilbert indexes and it also can be readily combined with the SPH neighbour search to obtain improved memory locality.

The above ordering strategies require a fast algorithm for sorting the particles in ascending order of their iboxp(i) values, and also a fast method to identify all the particles with the same position in the space-filling curve (i.e., the particles within a given mesh cell). To that end, two different approaches have been proposed in the literature:

1. Using a linked list, i.e., a vector ihc(ibox) giving the first particle within the cell

ibox, and another vector ll(i) so that all the particles in ibox are found through the sequence: i_1 =ihc(ibox), i_2 =ll(i_1), i_3 =ll(i_2),..., ll(i_{last})= 0. The sequential construction of a linked list requires a single loop over particles: the particle i is added to ll(ibox) by assigning ll(i) = ihc(ibox) followed by ihc(ibox)=i. Such an algorithm is difficult to be efficiently computed in parallel, because a race condition appears when different threads try to modify ihc(ibox). We have implemented the parallel strategy proposed by Merz et al. (2005): each thread constructs a private linked list for a subset of particles. The tail and head of each individual list are stored, so that all them can be later merged into a single list by linking the tail of an individual chain to the head of another one. Such a strategy has however a scaling limited to a few threads, because it requires much more operations than a sequential algorithm (e.g., some vectors like ihc(ibox) have to be individually initialized to zero on each thread).

2. Using an ordering list, i.e., a parallel sorting routine to obtain the particles identities ll(i) in increasing order of iboxp(i). In this way, the particles within a given mesh cell (i.e., with the same value of iboxp) will appear in consecutive locations of ll(i). The first particle ihc(ibox) within each cell can be also identified and stored through a single loop: ihc(ibox) will corresponds to the first particle in ll(i) with iboxp(i)=ibox. We have used a parallel sorting routine based on the radix-sort method and kindly provided by D.A. Bader (see Bader & JáJá, 1999, for a detailed description). The efficiency of such a routine is modest, but has a better scaling than the parallel construction of a linked list (we tested the scalability of both approach with up to 16 cores, see Table 2.1). Therefore, most parts of P-DEVA requiring the ordering of particles are carried out by using such a radix-sort method. Nevertheless, since such a method requires a longer computing time when performed on a single sequential thread, some parts of P-DEVA (such as the refinement farm, where each processor deals with a full refinement) use instead a linked-list ordering.

2.3.3 Domain decomposition

Once chosen a given space-filling curve and carried out the corresponding particle reordering, the total amount of work must be divided into various pieces of work that are suitable for distribution to the $N_{\rm proc}$ individual processors. Ideally, such pieces of work should require similar amounts of computing time to ensure a good load balancing of

Table 2.1: Ratio of the wall-clock time spent by a linked list to that expended by a radix-sort ordering. This test has been run on our local server with 16 cores (see Section 2.7 for a description of the hardware used in the developement of the code).

Task	z	N	$r_{cpu=1}$	$r_{cpu=8}$	$r_{cpu=16}$
AP^3M	0	2×256^3	4.70/8.54	2.95/1.58	3.76/1.89
SPH	0	2×256^3	-/4.90	-	-
AP^3M	2	2×128^3	0.48/0.74	0.29/0.20	0.40/0.30
SPH	2	2×128^3	4.70/6.57	1.48/2.16	1.42/2.47

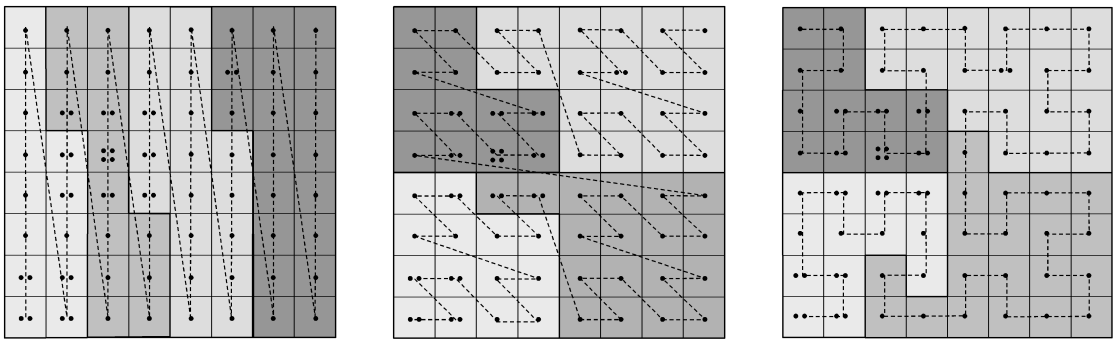

Figure 2.1: From left to right: Two-dimensional domain decomposition in regions with similar particle numbers using the column major, Morton and Peano-Hilbert space-filling curves. Dots represent particles in each cell.

processors. However, in very clustered cosmological simulations, it is hard to achieve a very good load balance because a small number of mesh cells usually require a heavy workload.

The most frequent approach in cosmological simulations consists of dividing the computational volume into various domains, or compact subvolumes, each assigned to one processor. Since the workload increases with the number of particles, a straightforward method of domain decomposition consists of dividing the space-filling curve into N_{proc} parts containing similar particle numbers. Obviously, the region occupied in the physical space by each domain depends on the space-filling curve (see Figure 2.1). For example, Springel (2005) used a domain decomposition based on the Peano-Hilbert space-filling curve to preserve locality and, therefore, for efficiently using cache allocations and reducing communication costs with neighbouring domains.

In AP^{3}M based codes, the above method of domain decomposition does not necessarily provide the best performance. Here, load balancing under conditions of heavy particle clustering is mainly achieved by the adaptive scheme: the largest amounts of PP work are delayed to the next refinement level. As a consequence, a domain with a large number of clustered particles could imply a computing time much shorter than in other domains since most of work is delayed to further refinement levels. In other words, in this kind of codes, a single domain decomposition based on particle counts could lead to a poor load balancing between processors. A different strategy is here needed. For example, in their MPI version of Hydra, Pringle et al. (2001) have reported a good load balance by using a large number of small blocks of chaining cells. Using cyclic patterns that select spatially separated blocks the simulation volume is then distributed to the processors. In P-DEVA, we have taken into account the above difficulty of obtaining an optimal domain decomposition in AP^{3}M-based codes, that is dramatically increased when using a time integrator with individual time steps, while trying to recover the data locality and cache efficiency achieved through the particle reordering in a space-filling curve. To that end, the AP^{3}M part of the code distributes small refinements among processors, as described in section 2.5.1, thus ensuring that no CPU sits idle while there are still refinements left to be evaluated.

During the development of P-DEVA we have tested the performance effects of using a Peano-Hilbert space-filling curve and a slab decomposition. Table 2.2 summarizes the results of some of these tests. We see that a space-filling method based on the Peano-Hilbert curve provides the best global performance in our code. Consequently, such a space-filling curve will be assumed hereafter.

2.4 Time Integration

2.4.1 Time-symmetric Integration cycle

The simulation of a system constituted by N particles usually requires a computational effort which considerably varies from some regions (or particles) to other. For example, regions of high density and submitted to strong shocks need to be simulated with timesteps much shorter than the rest of the system. In the AP^{3}M+SPH codes described in the literature, all the particles in the system are simultaneously advanced at each timestep. The particle needing the highest time resolution determines the timestep length of all the others. Consequently, some few particles can slow down the simulation of a system. To make a code more efficient in handling with problems with multiple time scales, the computational effort must be centered on those particles that require it, avoiding useless computations for the remaining particles. In other words, it is necessary to allow for different timesteps for each particle.

In N-body simulations, high-accuracy integration procedures are needed to ensure that the drift in the value of conserved quantities is kept to a minimum. Two main approaches have been proposed to improve the long-term stability of the theoretically conserved quantities: 1) symplectic integrators, where the simulated system is guaranteed to follow a slightly perturbed Hamiltonian system, and 2) time-symmetric integration schemes, where reversible processes are preserved so that no secular errors are present in conservation laws (Quinlan & Tremaine, 1990; Cano & Sanz-Serna, 1997). Both methods have been used in cosmological codes. As an example, the time-integration in GADGET-2 (Springel, 2005) and GASOLINE (Wadsley et al., 2004) is based on a symplectic integrator, while codes using the GRAPE special purpose hardware (Makino et al., 1997) use a time-symmetric Hermite integrator. The introduction of variable and/or individual time-steps leads to a loss of the symplectic or time-symmetric character of integration methods.

P-DEVA uses a time-symmetric integrator based on a n-order PEC (Predict-Evaluate-Correct) Hermite scheme (see e.g., Kokubo et al., 1998). In a second order accuracy scheme (the extension to a higher accuracy level n is straightforward, but requires $n-2$ additional arrays to store high-order derivatives), such an integration method proceeds according to the following steps.

1. We enter the step n (which corresponds to the time t^n) with known variables and derivatives for all the N particles. Furthermore, the time at which the last update

of $\mathbf{a}_i$ was performed is stored in t_i^{last} while $t_i^{next} = t_i^{last} + \Delta t_i$ contains the time at which a recomputation of $\mathbf{a}_i$ will be necessary in the future.

2. The global time is advanced by $t^{n+1} = t^n + \Delta t$, where Δt is the shortest prediction time

$$\Delta t = \min_j (t_j^{next} - t^n) \ . \tag{2.20}$$

3. For all particles, we use the values stored at t^n to predict their corresponding values at $t^{n+1} \equiv t^n + \Delta t$

$$\begin{aligned} \tilde{\mathbf{r}}_1 &= \mathbf{r}_0 + \mathbf{v}_0 \Delta t + \mathbf{a}_0 \Delta t^2/2 \\ \tilde{\mathbf{v}}_1 &= \mathbf{v}_0 + \mathbf{a}_0 \Delta t \\ \tilde{u}_1 &= u_0 + \dot{u}_0 \Delta t \ . \end{aligned} \tag{2.21}$$

where $x_0 \equiv x_i^n$ and $x_1 \equiv x_i^{n+1}$.

4. A list is constructed with those particles j, labelled as *active*, which will be advanced at the current step.

5. Only for active particles, we compute their accelerations and correct $\tilde{\mathbf{r}}_1$ and $\tilde{\mathbf{v}}_1$ using :

$$\begin{aligned} \mathbf{r}_1 &= \tilde{\mathbf{r}}_1 + \frac{3}{20}(\mathbf{a}_1 - \mathbf{a}_0)\delta t^2 \\ \mathbf{v}_1 &= \tilde{\mathbf{v}}_1 + \frac{1}{2}(\mathbf{a}_1 - \mathbf{a}_0)\delta t \\ u_1 &= \tilde{u}_1 + \frac{1}{2}(\dot{u}_1 - \dot{u}_0)\delta t \ , \end{aligned} \tag{2.22}$$

where $\delta t \equiv \delta t_i = t^{n+1} - t_i^{last}$ represents the time elapsed from the last evaluation of $\mathbf{a}_i$ to that performed in the current timestep. Unlike Δt, the δt_j value is then different for each active particle.

From equations (2.21)-(2.22), the Hermite integrator is described in an implicit form as

$$\mathbf{r}_1 = \mathbf{r}_0 + \frac{1}{2}(\mathbf{v}_1 + \mathbf{v}_0)\delta t - \frac{1}{10}(\mathbf{a}_1 - \mathbf{a}_0)\delta t^2 \tag{2.23}$$

$$\mathbf{v}_1 = \mathbf{v}_0 + \frac{1}{2}(\mathbf{a}_1 + \mathbf{a}_0)\delta t \tag{2.24}$$

which is time-symmetric (i.e., subscripts 0 and 1 are used symmetrically so that equations remain unchanged in a backward-in-time integration).

6. We update the global time $t^{n+1} = t^n + \Delta t$, as well as the t_j^{last} and t_j^{next} values of each active particle.

2.4.2 Particle activation and individual time steps

Time step controls and time symmetry

In order to maintain the numerical stability, the individual timestep Δt_i of each particle must be updated according to a number of controls. In P-DEVA, Δt_i is chosen as a power-of-two subdivision of the largest allowed timestep $\Delta t_{\max}$:

$$\Delta t_i = \frac{\Delta t_{\max}}{2^{n_i}} \tag{2.25}$$

with

$$n_i = \lfloor \log(\Delta t_{\max}/\Delta t'_i)/\log 2 + 0.5 \rfloor \tag{2.26}$$

and

$$\Delta t'_i = \min(\Delta t_i^{\epsilon}, \Delta t_i^{h}, \Delta t_i^{cv}, \Delta t_{\max}) \tag{2.27}$$

Here, Δt_i^{ϵ} and Δt_i^{h} are timestep controls to avoid significant displacements per step, while Δt_i^{cv} is a timestep control which combines the Courant and viscous conditions:

$$\Delta t_i^{\epsilon} = (\epsilon^2/a_i^2)^{1/4}\,, \tag{2.28}$$

$$\Delta t_i^{h} = (h_i^2/a_i^2)^{1/4} \tag{2.29}$$

$$\Delta t_i^{cv} = \frac{h_i}{c_i + 1.2(\alpha c_i + \beta \max_j |\mu_{ij}|)}\,. \tag{2.30}$$

In the case of collisionless particles (stars and dark matter), only the Δt_i^{ϵ} and $\Delta t_{\max}$ controls are used.

The introduction of variable time steps leads to a loss in the time-symmetric character of equations (2.23) and (2.24). Indeed, when $\Delta t_1 \neq \Delta t_0$, the initial conditions (at step 0) are not found in a backward-in-time integration from step 1 (see Figure 2.2). Hut et al. (1995) have proposed an integration scheme where the time reversibility is restored by using an implicit definition of the timestep: $\Delta t = (\Delta t_0 + \Delta t_1)/2$. Since such a procedure requires the knowledge of Δt_1 at the end of the step, an iterative scheme is then needed with pre-evaluations of $\mathbf{a}_1$, backing up the timestep, and re-evaluation of $\mathbf{a}_1$ until that convergence is reached. In large N-body simulations, such an iterative scheme is however unpractical. Quinn et al. (1997) proposed a faster time-symmetrization procedure for leapfrog schemes and, in general, for symplectic integrators. However they noted that, although their scheme implies a considerable improvement, it is not strictly time-symmetric. Due to the temporary unsynchronization of particles in the leapfrog scheme, many different situations arise where a forward step followed by a backward step will not come back to the initial conditions (see Figure 3 of Quinn et al., 1997).

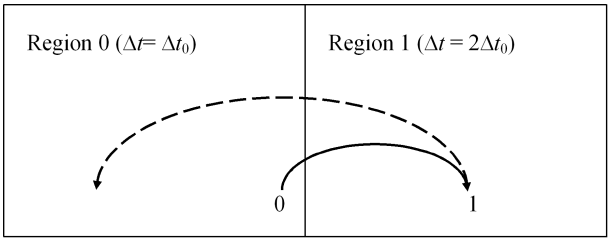

Figure 2.2: Loss of the time-symmetry in variable timestep integrations.

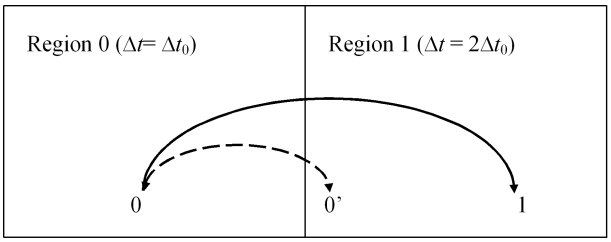

Figure 2.3: Time-symmetric stepping.

We will now propose a simple and fast procedure to preserve the time-symmetry of a PEC integration scheme with variable timesteps. Such a procedure has been implemented in P-DEVA. Consider an active particle in the same situation of Figure 2.2: i.e., after predicting $\mathbf{r}_1$, $\mathbf{v}_1$ and u_1 and updating its derivatives $\mathbf{a}_1$ and $\dot{u}_1$, one finds that Δt_1 is longer than the initial value Δt_0. In this case, if $\mathbf{r}_1$, $\mathbf{v}_1$ and u_1 are corrected using the updated derivatives, we will find the loss of time-symmetry represented in Figure 2.2. On the contrary, the time reversibility is preserved if particle is re-labeled as non-active (i.e., $\mathbf{r}_1$, $\mathbf{v}_1$ and u_1 are not corrected and we maintain its non-updated derivatives $\mathbf{a}_0$ and $\dot{u}_0$) while its individual timestep is replaced by the longer value Δt_1. Such a re-labeling must not be applied in the opposite situation (when $\Delta t_1 < \Delta t_0$), where the particle variables are instead corrected and updated as usual. Figure 2.3 shows how this procedure works. The dashed line $0 - 0'$ represents a first failed forward step from a region with $\Delta t = \Delta t_0$ to another region with $\Delta t = 2\Delta t_0$. Since an increase in its individual Δt value is found, the particle is re-labeled as non-active so that it maintains its non-updated derivatives of step 0, but now with $\Delta t = 2\Delta t_0$. With this new timestep, the particle will be later advanced and updated from 0 to 1 (solid line) since its individual Δt remains now unchanged. In a backward step starting from 1 (coincident with the solid line), the particle will come to the initial step 0 because no re-labeling is considered when a decrease in Δt is found.

Particle activation

Different criteria can be envisaged to decide which particles will be selected, at each integration step, for a full update of their variables (i.e., the list of *active* particles). A straightforward criterion consists of considering as active any particle with $t_i^{next} = t^{n+1}$ or, in other words, any particle with a prediction time equal to the shortest value given by equation (2.20). However, since cosmological simulations involve multiple time scales, the above procedure would imply activation lists containing a very small fraction of the total number of particles. This procedure is then unpractical because the evaluation of forces for those particles would imply having to compute PM forces for all the refinements including those particles. Thus a good part of the gravitational force for those particles in those refinements would be computed and later discarded. A fast and much more efficient strategy of particle activation consists of using the fact that P-DEVA is an AP^{3}M-like code. Instead of activating individual particles according to their t_i^{next} values, we activate to full zero-level or first-level refinements containing particles that need activation according to the t_i^{next} criterion. Using this strategy, the t_i^{next} of all particles in active refinements is advanced at a very low computational cost.

2.4.3 Parallel strategy

The prediction and correction steps (equations 2.21-2.22) of the integration cycle consist of single loops over particles. In these loops, each particle only needs its own data to modify its position, velocity and thermal energy. Their parallelization is then straightforward through the OMP DO directive. However, this is only true on SMP systems with UMA characteristics, where every processor can access all available memory with the same bandwidth and latency. On a ccNUMA architecture like SGI Altix or Opteron nodes, memory is logically shared but physically distributed, leading to the non-uniform access characteristics already mentioned in Section 2.3. In that case, the mapping between physical memory pages and logical addresses is essential in terms of performance: if data are allocated in one local memory, most threads are forced to a remote access to the data and performance does not scale at all. Since our code makes use of the first-touch page allocation policy, we obtain an acceptable scaling of parallel single loops over particles.

2.5 Gravitational forces: The AP^{3}M Algorithm

2.5.1 Placing refinements

A key condition for an efficient standard P3M method is that each grid cell must contain just a small number of particles. However, cosmological simulations usually must deal with heavily clustered regions, where some cells have a very large number of particles. In these regions, the number of particle-particle calculations over near neighbours could become prohibitively large, resulting in a dramatic slow-down of simulations. In order to circumvent this problem, Couchman (1991) proposed an Adaptive-P3M scheme based on the long-range/short-range force split of conventional P3M. Since the short-range force is spatially localized, there is no need to retain knowledge of the background field. Therefore, short-range forces in high-density regions can be computed by isolating such regions and locally dividing the grid into one or more finer grids (which may themselves be further subdivided) until there are just a few particles per grid cell.

The refinements (i.e., regions where PP forces are evaluated using finer grids) must be placed so that they maximize the saving in computing time.

1. The number of particles within each chaining cell is calculated and the peaks in this array above some threshold are labeled.

2. The saving, estimated by putting refinements of increasing size over each peak, is maximized. The optimal number of mesh points, L, is returned.

3. To seek a greater saving, the array in (1) is smoothed over a larger scale and the two previous steps are repeated

Changes on the sequential structure

In the public distribution of the AP^{3}M algorithm, the refinements and sub-refinements are found and placed by the routine refine, which drives several auxiliary subroutines (plref, mxfnd, nmaxw,...). The decision of which regions need a further refinement is embedded between the PM and PP calculation of either the full simulation box or a refined box, resulting in a recursive search for refinements. The information of the new refinements is stored in two arrays: Nlins and psf. The former contains, for each refinement *ip*, the number of particles, the optimal number of mesh cells per side, and the identity of the parent refinement. The latter contains the position and size of *ip*.

In P-DEVA, the full list of refinements and subrefinements is constructed before any computation of gravitational forces. This allows us to construct a structured chaining list. Once found the first-level refinements (i.e., those of the full simulation box), with

the same method refine uses, the refinements are loaded in turn and subrefinements found in a recursive way. This strategy imposes some restrictions on on the parallelization.

Parallel strategy

As remarked by Pearce & Couchman (1997), placing refinements in parallel is difficult because they may in general have any size and distribution, subject to the constraints that they are cubic and disjoint. These constraints force the problem to have a non-local character which makes the problem hard to distribute. Any blocking strategy employed to divide up the computational volume between the processors leads to boundary problems: placement of a new refinement is influenced by the distribution of those already placed.

Since the procedure of placing refinements is fast and takes no more than a few percent of the total computing time per integration step, we have not tried to deeply modify the corresponding Fortran routines. Instead of distributing the computational volume of each refinement between the processors, we use the constraint that refinements with equal levels do not overlap. Therefore, once completed the full list of refinements of a given level, the refinement list is distributed over the different processors. Each thread deals with a subset of complete refinements and performs all the tasks needed to find highly clustered regions within them. At the end of the parallel region, we have obtained the full list of the next level of refinements. If the list is not empty, their refinements are again distributed over processors and the procedure continues up to a maximum level of subdivision is reached. To prevent a race condition occurring, each thread has its private counter of new refinements as well as of the arrays containing the information that needs to be saved. The shared arrays and the global counter of refinements are updated within an OpenMP critical section.

Obviously, the above parallel strategy cannot be applied to obtain the first-level of refinement, because it results from a unique 0-level region: the full simulation box. It is then computed on a single processor. Since the top-level refinement distribution does not change rapidly, P-DEVA uses the same strategy as that proposed by Pearce & Couchman (1997): it is calculated only every 10 steps, while subsequent levels of refinement are placed every step. With this restriction the time taken to place refinements is less than 2 percent of the total even in difficult highly clustered positions when the refinement placing algorithm is most expensive.

Task farm of refinements

The smallest refinements ($N_r \leq N_{r,m}$, $N_{r,m}$ being a simulation parameter, here fixed to 64^3) are distributed as a task farm amongst the CPUs. As soon as one processor becomes free it is immediately given work from a pool via the dynamic scheduling option in OpenMP, with a particularity, the CPU to which the centre of the refinement belongs according to the domain decomposition used is determined, and each CPU computes first the refinements that belong to his domain and are yet unsolved before attempting to draw refinements form other CPU's pool. Load imbalance may still occur in the task farm if one refinement takes significantly longer than the rest and there are not enough refinements to balance the workload over the remaining CPUs. Note also that in order to avoid race conditions, the task farm is divided into levels, the refinements placed within the top level, termed 'level one refinements' must be completed before calculating the 'level two refinements',that have been generated by the level one refinements. However, we minimise the impact of the barrier wait by sorting refinements by the number of particles contained within them and then begin calculating the largest refinements first. This issue emphasises one of the drawbacks of a shared memory code: it is limited by the parallelism available and one has to choose between distributing the workload over the whole machine or single CPUs. It is not possible in the OpenMP programming environment to partition the machine into processor groups[1]. This is a major drawback that has been addressed by the development of an MPI version of the code (Thacker & Couchman, 2006).

2.5.2 Particle-Mesh Forces

The Mesh Density Field

The first step in evaluating long-range (PM) forces is to interpolate the mass density of the particle distribution on to a grid which can be viewed as a map from a Lagrangian representation to an Eulerian one. The interpolation function we use is the Triangular Shaped Cloud (TSC) assignment function

$$\rho(\mathbf{n}) = \frac{1}{V} \sum_i m_i U(\mathbf{r}_i - \mathbf{n}) \tag{2.31}$$

[1] Although a similar effect can be achieved by the usage of nested paralelism and the specification of the number of threads for each parallel region, this approach is cumbersome and there is no control on which CPU is assigned to each thread, thus losing all control over memory placement

where $U(\mathbf{r}_i) = u(x)u(y)u(z)$ and

$$u(x) = \begin{cases} \frac{3}{4} - x^2 & |x| \leq \frac{1}{2} \\ \frac{1}{2}(\frac{3}{2} - |x|)^2 & \frac{1}{2} \leq |x| \leq \frac{3}{2} \\ 0 & \text{otherwise} \end{cases} \tag{2.32}$$

Two benefits of using TSC are good suppression of aliasing from power above the Nyquist frequency of the grid and a comparatively low directional force error around the grid spacing. The mass assignment operation count is $\mathbf{O}(N)$, where N is the number of particles.

Smoothing onto a grid is a well studied but difficult problem to parallelize efficiently. In the TSC assignment scheme, the mass of each particle is distributed over the 27 potential cells around it. Therefore, if all the particles are processed in parallel, many processors may write to the same grid location simultaneously. Pearce & Couchman (1997) used an atomic update facility of CRAFT that prevents a race condition occurring when two or more processors try to write to the same memory location. However, with modern cache coherency protocols, the equivalent OpenMP atomic directive is very inefficient.

When the slab decomposition is used, the parallel strategy used in P-DEVA is based on the fact that the chaining cells have a minimal width of 2.2 potential mesh cells. Therefore, for this particular task, the computation volume is divided over the z-axis into different domains containing similar particle numbers. Each domain is constrained to have a minimal width on the z-axis of three chaining cells. In this way, any domain can be divided into three subdomains (referred as L, C, and R) of at least one chaining cell on the z-axis. The smoothing onto the potential mesh is then carried out in three steps. At each of such steps, only one type of subdomains (L, C or R) is distributed over the different processors, so that two adjacent subdomains are not processed (see Figure 2.4). Such a procedure ensures that each processor deals with a subset of particles in a region separated enough from those assigned to other processors, so that they do not write to coincident grid locations. In addition, this parallelization algorithm only needs three barriers or synchronization points, in contrast with the four or nine barriers needed by other algorithms also based on the same idea (see, e.g., Thacker & Couchman, 2006).

For the Peano-Hilbert curve decomposition a similar strategy is used, again based on the fact that four chaining cells cover at least eight potential mesh cells, and that each $4 \times 4 \times 4 = 64$ subvolume in the searching mesh is contiguous in the Peano-Hilbert domain. The computation loops 64 times over the whole volume, smoothing one of the 64 cells at a time, therefore avoiding concurrent writes to the same location of the

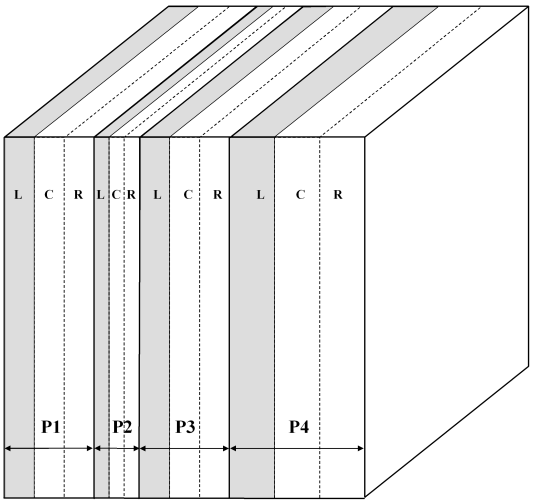

Figure 2.4: Computation of the mesh density field using a domain decomposition into regions with similar particle numbers. The domain assigned to each processor is divided into three subdomains (L, C, R), each with a minimal width of one chaining cell (2.2 potential cells), that are treated in three consecutive steps.

PM mesh. While this scheme keeps memory access local, it might have an impact on cache misses, since cells are not accessed in sequential Peano-Hilbert order, but rather in increments of 64. However, our measurements (see Table 2.2) indicate no significant slowdown when compared to the slab decomposition strategy.

The Mesh Potential Field

Once the mass density grid has been constructed it is Fourier transformed using a FFT routine. For the Fourier transforms themselves we use the FFTW library developed at MIT (Frigo & Johnson, 2005). Instead of following the standard procedure (Springel, 2005) of using a parallel 3-dimensional FFT, multiply the resulting k-space density field with an appropriate Green's function, and performing a 3-dimensional inverse FFT to obtain the potential field, we have preferred to combine the FFT and multiplication steps into a parallel 3D convolution procedure, by invoking 1D FFTs subroutines, and combining them with the multiplication with a Green's function that is calculated to minimise errors associated with the mass assignment procedure (see Hockney & Eastwood, 1981, for a review of the 'Q-minimisation' procedure). The procedure is done in the standard way (see, e.g., Pearce & Couchman, 1997), by first performing 1D FFTs

of lines parallel to the z axis, and then performing 1D FFTs in the two directions of xy planes. In the latter case, real data are packed into complex data, so that two planes are computed at once. In P-DEVA, the tasks on both the various z-lines and xy-planes are distributed over the different processors. Our procedure has the advantage of an explicit control over the parallelisation of the algorithm and the memory locality, which is previously allocated to the nodes in the mesh density part of the code. Another big advantage over the first procedure is that the PM mesh need be duplicated only over one direction when isolated conditions are assumed (like, for instance, in refinements), instead of the three directions, resulting in four times less memory usage.

Once the potential field is obtained, it must be differentiated to recover the mesh force field. Although many differencing operators are possible, we use the same 10-point operator as in Couchman (1986, Chapter 11), the x component of which is:

$$D_x(i,j,k) = \frac{1}{6}(\phi_{i-1,j,k} - \phi_{i+1,j,k}) + \frac{1}{12}(\phi_{i-1,j+1,k} - \phi_{i+1,j+1,k} + \phi_{i-1,j-1,k} - \phi_{i+1,j-1,k} + \phi_{i-1,j,k+1} - \phi_{i+1,j,k+1} + \phi_{i-1,j,k-1} - \phi_{i+1,j,k-1}) \tag{2.33}$$

which incorporates off-axis components and reduces directional force errors, but many others are possible.

Finally, the PM accelerations are found from the force grid using the mass assignment function to interpolate the acceleration field. The PM algorithm has an operation cost that is approximately $\mathbf{O}(\alpha N + \beta L^3 \log L)$ where α and β are constants (the $\mathbf{O}(L^3)$ cost of the differencing is adequately approximated by the logarithmic term describing the FFT).

2.5.3 Particle-Particle Forces

As mentioned above, the short-range gravity forces in P3M-based codes are computed by considering a mesh with L_s cells per side (searching mesh) and, then, by a direct sum over the 27 neighbouring cells of each particle. The dramatic slow-down of simulations with very clustered regions can be circumvented by the adaptive algorithm of Couchman (1991), where clustered regions (and subregions within them) are labeled as *refinements*. When computing the PP forces, interactions between cells belonging to the same refined region are temporally excluded (see Figure 2.5). Such interactions will be later computed by considering the refinement as an isolated box with finer PM and PP meshes.

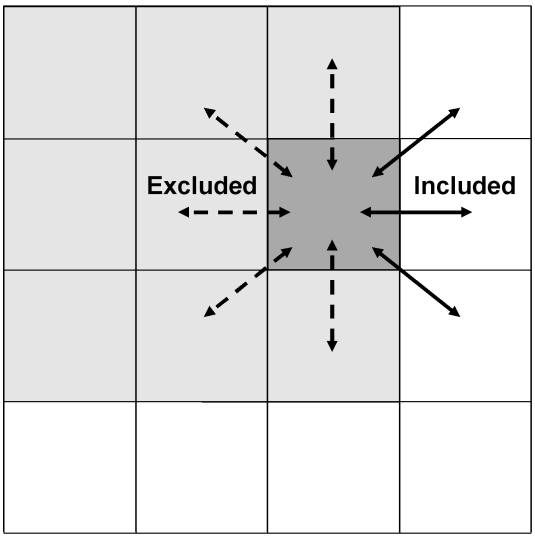

Figure 2.5: Short-range gravity forces on a cell belonging to a refinement (grey region). When computing gravity in its base mesh (white region), the PP-forces between non-refined cells and between cells belonging to different refinements (solid arrows) are included. Interactions between two cells of the same refinement (dashed arrows) are however excluded and computed, later, using an isolated refined mesh.

Since the largest amounts of PP work are delayed to the next refinement level, the above algorithm avoids a heavy workload for any processor and, therefore, prevents for a strong load unbalancing. However, an optimal domain decomposition is more difficult to be achieved than in other kinds of codes. Indeed, the exclusion of the next refined regions implies that computations are only required in a subset of mesh cells. Such an irregular spatial distribution of computational cells is even accentuated when using a multistep time integrator with individual time steps, i.e., when the update of forces is only required for a subset of particles. A cell-based distribution of work among processors and a domain decomposition into various compact subvolumes (see § 2.3.3), although still possible, becomes unnatural for this kind of codes.

In P-DEVA, we have dropped the usual cell-based strategy to compute short-range forces. Although a searching mesh is still employed to find the neighbours of each particle, we use instead a particle-based distribution of work among processors. After identifying the particles actually required for computations at a given refinement level, a parallel loop over such particles distributes the work among processors and, then, a good load balancing is easily achieved. To also ensure a good cache efficiency and data locality, the arrays containing the particle data ($\mathbf{r}_i$,...) are copied into local allocatable arrays ($\mathbf{r}'_j$, ...) where the required particles are ordered in the same way that they will be later needed for computations. The first-touch placement policy assigns similar blocks of particles to the local memory of each processor. Note that such auxiliary arrays $\mathbf{r}'_j$,... do not imply a memory requirement higher than in a cell-based strategy. Such arrays are needed in any case to store the particle data in units scaled to the refinement size.

More in detail, at a given refinement level, short-range gravity forces are computed through the following scheme (see Figure 2.6):

1. The particles belonging to the n'th refinement are sorted within a searching mesh of $L_s(n)$ cells per side. Using the resulting linked (or ordering) list, their masses and positions are copied to local allocatable arrays, m'_j and $\mathbf{r}'_j$, in units scaled to the refinement size. This task is performed within a parallel loop, so that the first-touch placement policy distributes among processors the memory location of particle data.

2. The mesh density field and the resulting Particle-Mesh forces on active particles are computed as explained in § 2.5.2.

3. If the smoothing length for the force law is bigger than the smoothing length implied by the PM forces, there is no need to compute short-range forces and the

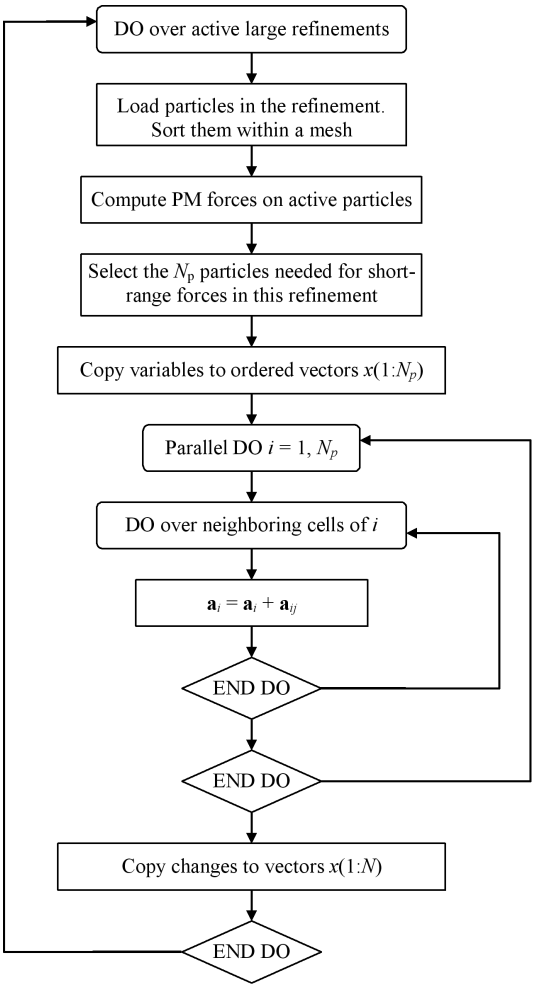

Figure 2.6: Flux diagram of short-range gravity computations.

refinement is marked as done.

4. Otherwise, the N_p particles needed for short-range (PP) gravity forces are selected by neglecting (e.g., by imposing ihc_{ibox}=0) any cell in a subrefined region and with the 27 neighbouring cells belonging to its own subrefinement. In the zero-level refinement, when their particles do not need to be updated at the current time step, only the cells neighbouring an active refinement are selected.

5. A new copy to local allocatable arrays is carried out using the above ordering list and the first-touch placement policy. Such a copy is now restricted to the N_p previously selected particles.

6. The main loop over the N_p selected particles is then carried out in parallel. Therefore, each processor deals with its local block of N_p/N_{proc} ordered particle data. For each particle i of this loop, the contribution to $\mathbf{a}_i$ from particles located in the 27 neighbouring cells is added by direct summation. Note that, in this scheme, the acceleration of particle i is only updated by its corresponding processor. Therefore, no race condition appears.

7. After finishing the above main loop over the N_p selected particles, the short-range gravity accelerations contained in the ordered array $\mathbf{a}'_j$ is rescaled and added to the global acceleration array $\mathbf{a}_i$.

8. The above computation cycle is repeated for the next refinement.

2.6 The SPH Method

2.6.1 Implementation of SPH

Note that Eqs. (2.12) and (2.15) have been deduced by using both spatial and time derivatives of the SPH density as defined by Eq. (2.7) *with the symmetrization specified in* Eq. 2.9. Conservation laws require in fact the evaluation of SPH force and energy equations in consistency with the density definition. In the case of P-DEVA, this requirement increases the CPU time per integration step. In fact, since the density ρ_i associated to a particle i depends on both h_i and h_j, for $j = 1, ..., N_S$, (i.e., for its N_S nearest neighbours, see Eq. 2.7), the computation of ρ_i at a given integration step requires the knowledge of h_j for these N_S nearest neighbours at its beginning [2]. This

[2] As a matter of fact, each h_j value must be kept fixed all along the integration step in order to avoid violating the reciprocity principle

can be achieved either by using the h_j values predicted in the previous integration step or by performing, at each step, a first loop over the particles to compute their h_j values and, once it is over, a second loop to compute their hydrodynamical properties. Since we look for a high accuracy rather than a high computational speed, we have adopted the second possibility.

Neighbour search

Hydrodynamics involves short-range forces and effects and, therefore, a search of neighbours must be carried out for each gas particle i. As for the PP-gravity forces, such a task can be addressed by considering a mesh with cell sizes slightly larger than the extend $2h_i$ of hydrodynamic effects on i. In this way, we only need to look for possible contributions of particles located in the 27 neighbouring cells of i. However, SPH contributions have a crucial difference with respect to PP-gravity forces: the smoothing length h_i depends on the particle location $\mathbf{r}_i$ and, therefore, each particle requires its own searching mesh different from that of other particles. An algorithm based on a large number of searching meshes is however unpractical because each mesh involves non-negligible additional tasks as, for example, the ordering of particles. In the same way, an algorithm using a unique searching mesh is also unpractical. Indeed, to ensure correct computations in regions with the lowest density (i.e., with the largest h value, h_{max}), the latter algorithm would require a cell size of $2h_{max}$. As a consequence, the neighbour search in high density regions would be very expensive in computing time because each particle i must look for a large number of (vanishing) contributions.

In order to circumvent this problem some alternatives have been previously used, such as combining the SPH neighbour search with the PP gravity neighbour search and using the different scales provided by the multiple meshes used for refinements to search for neighbours (Couchman et al., 1995). While this approach has the supposed advantage of less computational overhead (that might not be true, see Couchman et al., 2002), it will not give the correct list of neighbours for voids or very low density regions. We use a fiducial strategy, proposed by Couchman et al. (2002), based on a small number of different searching meshes. More specifically, this strategy first considers a mesh with cell size $2h_{max}$. Such a mesh is used to update the SPH effects only on active gas particles with $h_i \in [h_{max}, h_{max}/2)$ (i.e., particles in the lowest density regions). Then, we consider another mesh where the cell size has been divided by 2 and update the SPH effects on particles with $h_i \in [h_{max}/2, h_{max}/2^2)$. Such a procedure continues up to reaching cells small enough to include particles with $h_i = h_{min}$, i.e., the highest density

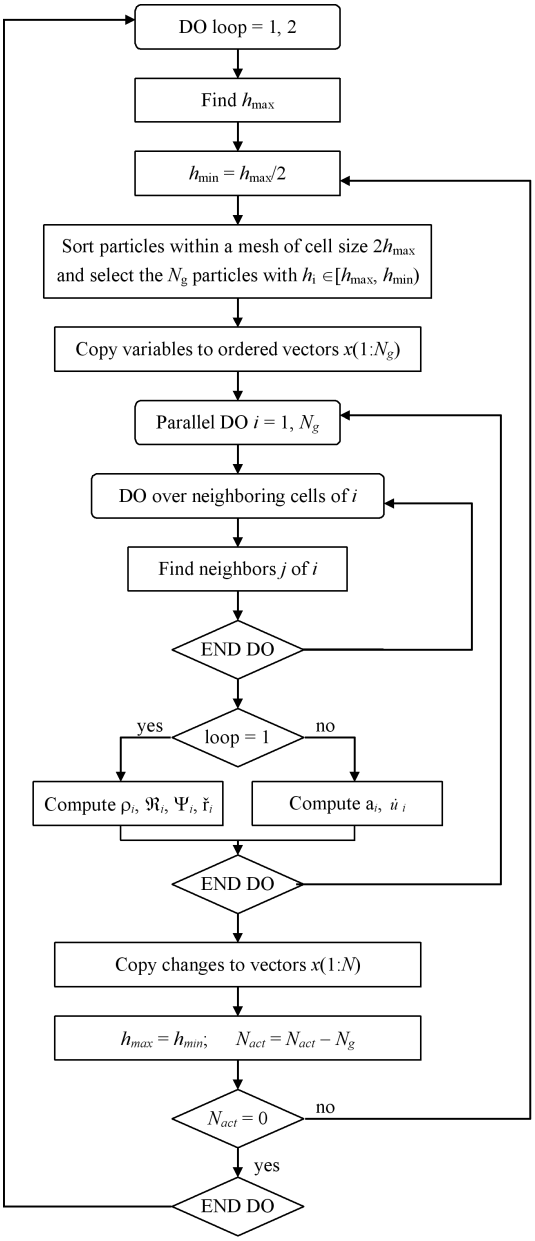

Figure 2.7: Flux diagram of SPH computations.

regions. Note that the number N_m of meshes required by such a procedure is given by $h_{max}/h_{min} = 2^{N_m}$. For example, in a simulation with $\rho_{max}/\rho_{min} \simeq (h_{max}/h_{min})^3 = 10^6$, the number of required meshes is $N_m = 2/\log_{10} 2 \simeq 7$.

Parallel strategy

Within the nth mesh of the above procedure for neighbour search, we only deal with a subset of particles constituted by active gas particles with $h_i \in [h_{max}, h_{max}/2)/2^{n-1}$ and their possible neighbours. As a consequence, computations are only required in a subset of the mesh cells, usually in spatially separated regions. A cell-based distribution of work among processors could then result in a strong load unbalancing and/or non-locality of data. A particle-based distribution of work among processors, similar to that employed for PP-gravity forces, clearly arises as a procedure to easily ensure load balancing and data locality.

1. Gas particles are sorted within a searching mesh of size L_g, corresponging to a cell size of $\sim h_{max}/2^{n-1}$. After constructing the linked (or ordering) list, we select the N_g needed particles and neglect (e.g., by imposing ihc(ibox)=0) any cell ibox without any active gas particle with $h_i \in [h_{max}, h_{max}/2)/2^{n-1}$ in its 27 neighbouring cells.

2. Using the above ordering list, all needed variables $\mathbf{r}_i$, h_i, ... for the N_g selected particles are copied to local allocatable arrays $\mathbf{r}'_j$, h'_j,... This task is performed within a parallel loop over the N_g selected particles. In this way, the first-touch placement policy distributes among processors the memory location of data in blocks of $\sim N_g/N_{proc}$.

3. The outer loop over the N_g selected particles is then carried out in parallel. Therefore, each processor deals with its local block of N_g/N_{proc} ordered particle data. For each particle i of this loop, its 27 neighbouring mesh cells are explored to construct the list nearlist() of particles with SPH effects on i.

4. The neighbour list nearlist() is then used to update the SPH variables of particle i.

5. After finishing the above main loop over the N_g selected particles, the ordered arrays containing modified variables (h'_j,...) are copied in parallel to their corresponding global arrays (h_i,...)

6. The computation cycle is repeated for the next ($n' = n + 1$) searching mesh until no more meshes are left.

When updating the SPH properties of particle i, in the step 4 of the above computation cycle, we must use some SPH variables of its neighbouring gas particles. More specifically, we must know the density ρ_k (equation 2.7), as well as the the $\Re_k$, Ψ_k and $\breve{r}_k$ vectors defined by equations (2.13), (2.14) and (2.16).

In the first SPH loop, we update the gas density and the arrays needed for the ∇h corrections. In particular, the $\Re_k$, Ψ_k and $\breve{r}_k$ vectors defined by Equations (2.13), (2.14) and (2.16), respectively.

In the second SPH loop, we update $\mathbf{a}_k$ and $\dot{u}_k$ including their viscosity and ∇h correction terms (equations 2.12, 2.15 and 2.17).

In order to efficiently implement the described scheme, the ordering of the particles has to be taken into account. The particles are ordered according to a Peano-Hilbert curve defined in the searching mesh of the main PP loop, of size L_s. In order to minimise the communication load, it is desirable to follow the same curve in the SPH part of the code. For the first iterations of the neighbour search scheme, $L_g \leq L_s$, and the procedure is straightforward. The Peano-Hilbert curve has the desirable property of being a fractal. This property ensures that a partition within a coarser mesh that is also a power of 2 can be made to follow the original partition. The Peano-Hilbert cell index iboxp(i) of each particle is easily reduced to the corresponding index in the coarse mesh by taking the $\log(L_g)/\log(2)$ most significant bits of the index.

For the finer meshes, when $L_g > L_s$, a more elaborate procedure is required. The already computed Peano-Hilbert index is only defined up to a size L_s. With a finer mesh, an ordering inside those cells is required. The most straightforward procedure would be to also follow a Peano-Hilbert curve inside the coarse cells, effectively defining a finer Peano-Hilbert curve. This simple approach has the disadvantage of requiring a prohibitive number of evaluations of the Peano-Hilbert indices of neighbouring cells when L_g becomes high. We have addressed this problem by defining a column-major ordered mesh inside each cell of the searching mesh. We define a new cell index for each particle by taking into account the Peano-Hilbert index and the inner index defined by the column major ordering. Both indices are bit-combined into a single index for each particle, with the Peano-Hilbert index stored into the most significant bits of the new index, and the column-major inner index into the least significant bits. When the particle list is walked it is done in an orderly way, with active particles having the same the Peano-Hilbert index being evaluated sequentially. The Peano-Hilbert indices

of neighbouring cells need thus be evaluated only once for each coarse cell. The index of neighbouring sub-cells can be easily evaluated by bit-combining two indices in the described way.

2.7 Tests and Performance

In order to test the results and performance of P-DEVA we have run two different tests: the adiabatic Santa Barbara cluster test of Frenk et al. (1999) and a non-adiabatic ΛCDM simulation. The former models the cosmological formation of a galaxy cluster and has become a widely used test to compare the results obtained from different codes. The latter considers a ΛCDM model already used in our previous works with DEVA to study the formation of galaxies with different morphologies (Sáiz et al., 2004, e.g.,). Such a ΛCDM model will be used here to compare the results of DEVA and P-DEVA.

Two different machines have been used when developing and testing the P-DEVA code. For most development purposes an 8-way Iwill H8051 NUMA server equipped with dual-core AMD Opteron 870 processors (total of 16 cores) and 32GB of RAM locally installed and self-administered was used. Larger scale tests and simulations with up to 128 cores were run on the HLRB-II SGI Altix 4700 system at the Leibniz-Rechenzentrum of Munich.

2.7.1 The Santa Barbara cluster test

The Santa Barbara cluster problem was proposed by Frenk et al. (1999) to compare the results obtained from different codes. The formation of a X-ray cluster in a Cold Dark Matter (CDM) universe has been simulated using most of the hydrodynamic codes available at that time, setting a standard of reference to test newly proposed hydrodynamic codes. This test has been run on our local Iwill server.

The initial conditions of this test correspond to a 3σ peak of the density field smoothed with a Gaussian filter of radius $r_0 = 10$ Mpc according to the algorithm of Hoffman & Ribak (1991). The perturbation was centered on a periodic cubic region of side $L = 64$ Mpc. The cosmological scenario is a flat CDM universe with $H_0 = 50$ km s^{-1} Mpc^{-1} for the Hubble constant; $\sigma_8 = 0.9$ for the present-day linear rms mass fluctuation in spherical top hat spheres of radius 16 Mpc; and $\Omega_b = 0.1$ for the baryon density (in units of the critical density). 64^3 dark matter and 64^3 baryon particles have been used with a softening length of 20 kpc.

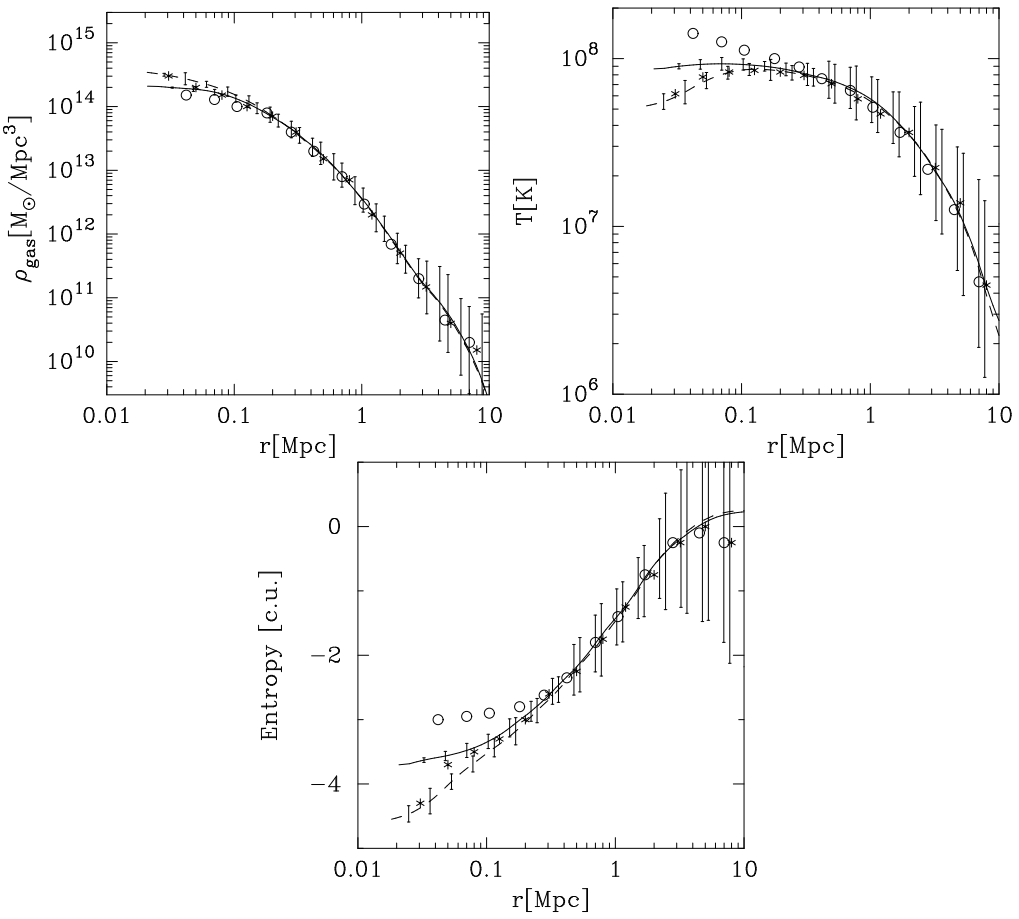

Figure 2.8: Density, temperature and entropy profiles in the Santa Barbara cluster test. The stars represent the SPH results obtained by Jenkins, while circles represent the results obtained by Bryan & Norman from an adaptive mesh refinement code. The lines correspond to the results obtained from DEVA or P-DEVA when the ∇h terms are taken into account (solid line) and when these terms are neglected (dashed line).

Similarly to Serna et al. (2003), two different simulations were run with P-DEVA. In one of these simulations, the ∇h terms have been considered while in the other they have been neglected. In Figure 2.8, the density, temperature and entropy profiles of the cluster are plotted. The stars represent the results obtained (Frenk et al., 1999) by Jenkins from a high-resolution SPH simulation using a parallel version of the Hydra code (Pearce & Couchman, 1997), while the circles represent the results obtained by Bryan & Norman from a high-resolution adaptive mesh refinement shock-capturing code, SAMR, (Bryan et al., 1995; Bryan & Norman, 1995). Both results from DEVA and P-DEVA are virtually indistinguishable, and we plot here only the results from P-DEVA. As previously remarked by Frenk et al. (1999), we see that the SPH and mesh results differ at the central region. This figure also shows the results obtained from our code both when the ∇h terms are included (solid line) and neglected (dashed line). Error bars correspond to the standard deviation of the individual SPH data.

As was discussed in Serna et al. (2003), our results differ slightly depending on whether the ∇h terms have been included or not. Moreover, when the ∇h terms are neglected, we obtain results that are similar to those of previous SPH simulations, and very close to Jenkins' results, obtained with a much higher resolution. When these terms are taken into account, the results are intermediate between previous SPH and grid results. This suggests that, at least in part, the difference between the SPH and grid results could be due to the non-physical entropy introduced by SPH codes. This non-physical entropy is negative (Alimi et al., 2003) and, therefore, it produces objects with a smaller central temperature and a higher central density. Indeed, we have shown in Serna et al. (2003) that the entropy conserving formulation of GADGET (Springel & Hernquist, 2002) leads to an entropy profile for the Santa Barbara cluster in close agreement with that obtained from our code.

To sum up, the inclusion of the ∇h terms is relevant, and the new parallel version of DEVA succeeds at obtaining totally compatible results with the previous serial version in a standard cosmological test such as the Santa Barbara cluster test.

2.7.2 Galaxy formation in a ΛCDM Cosmology

In order to further check the results of P-DEVA, as compared to those obtained from our previous sequential code, we have simulated the structure formation at galactic scales. Several results concerning the fundamental plane have already been obtained with the sequential version of the code (Sáiz et al., 2004; Domínguez-Tenreiro et al., 2004; Oñorbe et al., 2005; Domínguez-Tenreiro et al., 2006; Oñorbe et al., 2006, 2007),

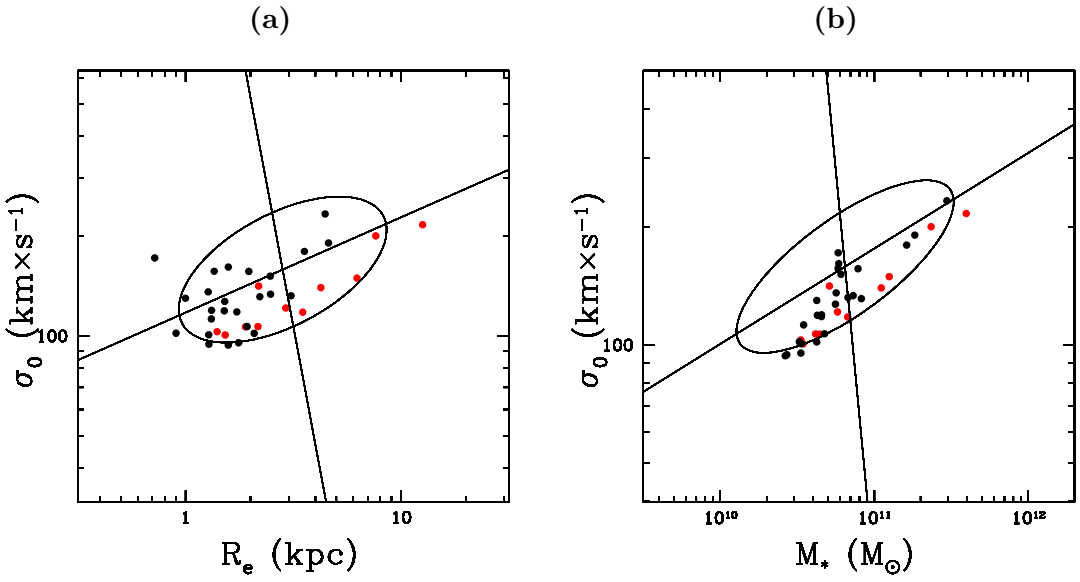

Figure 2.9: The central l.o.s. velocity dispersions of ELOs in the sample versus **(a)** their stellar half-mass radii or **(b)** their stellar mass. For both figures, red dots correspond with objects extracted from old simulations performed with the DEVA code, while black dots correspond with objects extracted from the simulation described in this section. We also draw the concentration ellipse (with their major and minor axes) for the SDSS early-type galaxy sample from Bernardi et al. (2003) in the z-band.

and the purpose of this test is to find out whether the validity of previous results still holds with the new P-DEVA version of the code. To this end we have run a full-box cosmological simulation in the framework of a flat ΛCDM cosmological model, with $h = 0.69$, $\Omega_{\rm m} = 0.29$, $\Omega_{\rm b} = 0.048$, and $\sigma_8 = 0.85$. The gravitational softening was $\epsilon_{\rm g}$= 1.5 kpc and SF parameters were chosen ($c_* = 0.1$ and $\rho_{\rm g,thres} = 1.8 \times 10^{-24}$ gr cm^{-3}) to include feedback effects from stellar processes in just an implicit way. No chemical feedback was included.

In Figure 2.9 we represent the relation between line-of-sight velocity dispersion and half-mass radius or stellar mass for the elliptic-like objects (ELOs) obtained in this simulation. In the same plots we represent the results of previous DEVA simulations already presented in some of the above mentioned works, together with observational ellipses. As it can be seen, the objects simulated with either code are compatible with the observational results, that is we still recover a fundamental plane for ELOs in simulations

compatible with the observed one. While there are slight differences between the distributions originating from either code, this is possibly due to the fact that different cosmological parameters have been used for both simulations.

2.7.3 Performance tests

Table 2.2 summarizes the different blocks of tasks carried out at each integration step, as well as the clock time for a series of tests carried on the HLRB-II supercomputer at the Leibniz-Rechenzentrum in Garching. Here we try to check how the code performance scales when simulating a large box (56 Mpc/h) with a high number of particles (2×512^3) in a rather highly clustered state ($z\simeq5$).

Two versions of the code that differ in the memory arrangement of particles have been put to test, these have been previously described in Section 2.3.2 as a column-major (or slab) and a Peano-Hilbert curve. While the first is simpler to implement, the results indicate that the second one scales slightly better to higher number of processors.

As it can be appreciated, even for such a high number of CPUs, the gravity part scales fairly well for both code versions. This is a remarkable fact, since the non-local character of the gravitational force makes its parallelization a especially difficult task. The SPH part of the code scales more poorly and becomes dominant for such a high number of processors. Although it is not practical to run such a big simulation with a single cpu in order to test the scaling, suffice to say that for a 2×128^3 simulation on 8 CPUs, the SPH and gravitational parts of the code take about the same wall clock time, so the SPH is clearly scaling poorly. We believe this is due to the fact that the parallelization strategy and memory distribution has been planned from the ground up with the AP^{3}M algorithm in mind, and we SPH part has been fitted *a posteriori* into the pre-existing scheme. In principle one would expect that the local character of the hydrodynamical interactions would ease the task of parallelization of the SPH part. We will try to solve this issue in successive versions of the code.

2.8 Summary and Conclusions

We have described P-DEVA, a parallel multistep AP^{3}M-like-SPH code designed to study galaxy formation and evolution in connection with the global cosmological model, that uses a formulation of SPH equations ensuring both energy and entropy conservation. The code has been parallelized using the OpenMP framework for shared-memory machines and successfully deployed in several supercomputers. Although the code scaling is not

Table 2.2: Wall-clock time in second per step t for 2×512^3 active particles in the clustered regime of a ΛCDM simulation.

Task	P-H 64	P-H 128	Slab 64	Slab 128
Predict variables	1.315	0.519	1.440	0.862
Correct variables	2.066	0.739	2.501	1.846
Hubble drag	0.796	0.271	1.062	0.694
Activation of particles	0.137	0.009	0.320	0.299
Updating timesteps	1.721	0.755	1.949	0.736
Cooling	2.946	1.423	2.583	1.432
Star formation	0.706	0.592	0.779	0.485
Sequential (Misc)	2.254	2.402	1.518	1.493
Subtotal (Misc.)	11.940	6.710	12.152	7.845
Placing refinements	5.027	3.909	2.082	0.468
Ordering/Linked list	27.740	5.525	36.604	5.622
Green function	0.586	0.114	0.323	0.236
Base mesh density field	10.207	4.730	3.089	1.862
Base mesh convolution	61.599	29.658	53.684	24.789
Base Mesh force	4.931	2.222	3.620	2.705
Label and select pp cells	0.138	0.057	0.132	0.048
Load/Unload PP	1.961	1.489	2.594	2.233
PP forces (base mesh)	132.329	65.119	42.390	17.486
AP^3M in large refinements	17.148	3.577	78.228	45.862
AP^3M in refinement farm	34.795	4.748	134.984	52.563
Sequential (Gravity)	79.781	70.585	72.263	64.299
Subtotal (Gravity)	376.242	191.733	429.992	218.172
Init SPH	1.562	0.107	3.358	0.254
SPH Load first loop	289.573	76.363	212.028	100.692
SPH Load Second loop	276.723	78.216	214.016	96.315
First SPH Loop	307.300	259.309	352.365	287.105
Second SPH Loop	509.137	428.043	568.450	478.256
Sequential (SPH)	7.697	9.222	6.332	6.228
Subtotal (SPH)	1391.993	851.261	1356.550	968.850
Total	1780.175	1049.704	1798.694	1194.867

perfect, we believe the conservation and accuracy of the code make it a good tool to perform simulations of galaxy formation.

In the next chapter we will describe the sub-resolution model for star formation, chemical evolution and cooling that we have added to the code. These model also tries to be as self-consistent and accurate as possible, in line with the main code.

Chapter 3

A composition-dependent SPH model for chemical evolution and cooling[1]

> Science may be described as the art of systematic over-simplification – the art of discerning what we may with advantage omit
>
> Francis Bacon

3.1 Introduction

Chemical abundances are a rich reservoir of information which can help uncover how the formation of galaxies took place. Indeed, even after epochs where much information is lost through phase mixing or violent relaxation, stars still retain important clues about the evolutionary histories of the objects from which they come (e.g., Freeman & Bland-Hawthorn, 2002). The earliest studies of the chemical evolution of galaxies were based on the well-known Closed Box model (Lynden-Bell, 1975; Tinsley, 1980), that played an important role in obtaining a first insight into this problem. This model considers galaxies as one-zone systems with a constant total mass and instantaneous recycling and mixing of matter. Because of such simplifying assumptions, the Closed Box model provides no idea about the internal structure of galaxies and leads to some predictions that are inconsistent with the distribution of G-dwarfs in the solar vicinity, as well as with other observations (Pagel & Patchett, 1975; Valle et al., 2002).

After the seminal work of Lacey & Fall (1983, 1985), other approaches (e.g., Díaz & Tosi, 1986; Matteucci & Tornambe, 1987; Clayton, 1987; Sommer-Larsen & Yoshii, 1989;

[1] This chapter is published as Martínez-Serrano, F. J., Serna, A., Domínguez-Tenreiro, R., & Mollá, M. 2008, MNRAS, 388, 39, arXiv:0804.3766.

Matteucci & Francois, 1989; Ferrini et al., 1994; Chiappini et al., 1997) have considered multi-zone chemical evolution models with external gas infall. Numerical computations based on these kinds of models have been successful to describe the radial distribution of abundances in our Galaxy (Ferrini et al., 1994; Boissier & Prantzos, 1999) and in other spiral disks (Molla et al., 1996; Boissier & Prantzos, 2000; Mollá & Díaz, 2005). The success of most of these models is based on appropriate spatial variations of the ratio between the star formation rate and gas infall rate, which are achieved by using different code input parameters for different galaxy types. It is then important to compute more realistic models where such rates naturally appear, within a cosmological context, as a result of the physical processes involved in the formation and dynamical evolution of galaxies. Due to the complexity of this problem, it must be addressed from approaches like, e.g., hydrodynamic N-body simulations.

Among the different methods developed for the modelling of complex hydrodynamic phenomena, the Smooth Particle Hydrodynamics (SPH) technique (Monaghan, 1992) is one of the most widely used in astrophysics. Due to its Lagrangian nature, the evolving distribution of the gas, dark matter and stellar components can be easily followed in a self-consistent way. The first approach to include chemical evolution in an SPH code was proposed by Steinmetz & Muller (1994, 1995), followed by Raiteri et al. (1996), Carraro et al. (1998), Berczik (1999), Kawata & Gibson (2003) and Kobayashi (2004), among others. All these works focussed on the chemical enrichment of isolated objects, or groups of objects, formed from pre-prepared initial conditions. Recent works (see, e.g., Mosconi et al., 2001; Scannapieco et al., 2005; Kobayashi et al., 2007) have extended SPH simulations to study the detailed chemical enrichment of galaxies within a full cosmological context, where mergers and interactions have important effects.

A new degree of sophistication in the SPH-modelling of chemical enrichment was introduced by Lia et al. (2002, hereafter LPC02), who proposed a stochastic algorithm to completely remove the assumption of instantaneous recycling of stellar ejecta. Such a delayed gas restitution from stars has non-negligible dynamical effects on N-body disks, as discussed by Jungwiert et al. (2001, 2004), and a direct impact on the resulting abundance gradients. The algorithm of LPC02 takes into account the non-instantaneous gas restitution from stars through a method where the total number of baryonic particles remains constant and no dynamically hybrid particles are present: they are either fully collisional or fully collisionless. The presence of such hybrid particles would introduce spurious dynamical effects like, e.g., stars that follow for a while the evolution of the gas. The LPC02 approach, already used in some studies (Sommer-Larsen et al., 2005;

Romeo et al., 2005, 2006), has the advantage that it leads to objects with reliable *average* values for their chemical properties. Nevertheless, due to its statistical nature, its main disadvantage is that large numbers of particles per object are needed to avoid an excessively high scatter around the average values.

Together with the inclusion of delayed gas restitution from stars, a necessary further improvement on the SPH modelling of chemical enrichment is the full dependence of both metal production and radiative cooling on the detailed chemical composition of star and gas particles, respectively. Indeed, the metal production of stars is usually included in SPH codes on the base of up-to-date libraries with stellar models and their corresponding ejecta for stars with different masses and metallicities. Such libraries (e.g., Portinari et al., 1998; Gavilán et al., 2005) generally assume solar relative abundances of the various species for any total metallicity Z. Nevertheless, it is well known that within a given Z different chemical compositions are possible. Chemical evolution models show in fact that abundance ratios are not constant in the course of galactic evolution (see, e.g., Portinari et al., 1998). Deviations from solar proportions, particularly the ratios of α-peak to Fe-peak elements, are also observed in different stellar systems. Supra-solar values for these ratios are observed in metal-poor stars of our Galaxy as well as in globular clusters (Kuntschner et al., 2002; Larsen et al., 2002), where [α/Fe] seems to increase with decreasing metallicity (Puzia et al., 2005), reaching values that vary from some α elements to others: Mg seems to converge towards [Mg/Fe] ~ 0.4 for very metal-poor stars (see Fuhrmann, 1999) whereas oxygen trends towards [O/Fe] ~ 0.6 (see Reetz, 1999). Such an α-enhancement is also observed in spiral galaxy bulges (Sansom et al., 1994) as well as in most of the central regions of elliptical galaxies (Burstein et al., 1984, 1988; Worthey et al., 1992; Guzman et al., 1993; Carollo et al., 1993; Davidge & Clark, 1994; Worthey, 1994), where the [α/Fe] ratio increases with velocity dispersion and hence with mass. Since the α-enhancement is commonly interpreted as the result of large and short star formation events at early times, it could provide us with a very strong constraint for models of galaxy formation. To accurately follow the evolution of this or any other abundance ratio, the assumption of solar proportions must be relaxed in cosmological simulations when computing the production of the different chemical elements.

On the other hand, the chemical content of the gas in the interstellar medium (ISM) is enriched by metal ejecta of different stars and then mixed through complex processes involving both local diffusion and motions at larger scales. Consequently, the gas of cosmological simulations (as well as in real objects) has a non-trivial mixture of metals

with trends that are not necessarily the same as in the solar vicinity. Since the radiative cooling rate of gas closely depends on its metal composition, a realistic modelling of galaxy formation must consider a metal-dependent cooling function. As pointed out by some authors (e.g., Romeo et al., 2006), ideally one would need cooling functions for different relative proportions of different elements. Nevertheless, the lack of a fast algorithm to implement such a composition-dependent cooling rate has forced the use in cosmological simulations of the Sutherland & Dopita (1993) functions, given for chemical compositions mimicking those in the solar vicinity (scaled, according to the total metallicity, from primordial to solar abundances).

In this paper we present a new SPH-model for chemical evolution and cooling. Our model includes: i) the delayed gas restitution from stars by means of a probabilistic approach based on the LPC02 scheme. Such a scheme has been modified to reduce the statistical noise and, hence, to allow for the study of the inner chemical structure of objects with moderately high numbers of particles; ii) the full dependence of metal production on the detailed chemical composition of stellar particles. To this end, the chemical production of a stellar particle is computed by using the Q_{ij} matrix formalism (Talbot & Arnett, 1973), that relates each nucleosynthetic product to its sources; and iii) the full dependence of radiative cooling on the detailed chemical composition of gas particles. This latter issue is achieved through a fast algorithm where the cooling rate is not computed by using the total metallicity as the scaling parameter. We use instead a parameter $\zeta(T)$ defined as a linear combination of the abundance of different chemical species. The coefficients of such a linear combination depend on temperature and give the weight of each element on the total cooling function.

The work presented in this paper will focus on the description and testing of our chemical model. In order to analyse whether this model is able to produce galactic objects with chemical properties consistent with observations, we also report some first results on the cosmological formation of elliptical galaxies. Such simulations have been carried out by using the DEVA code (Serna et al., 2003). Nevertheless, the model presented in this paper is not limited to any particular code. In forthcoming papers we will analyse for larger galaxy samples some important chemical properties like, e.g., the metallicity distribution functions (MDF) and abundance gradients within individual objects, as well as the mass (or luminosity) relation with age, metallicity and $[\alpha/\mathrm{Fe}]$.

This paper is organised as follows. In Section 2 we describe our model for chemical evolution, whereas Section 3 presents our algorithm to compute composition-dependent cooling functions. Some synthetic tests as well as first results on cosmological simulations

are shown in Section 4. Finally, in Section 5 we summarise our main results.

3.2 The Chemical Evolution Model

As in any particle-based scheme, both the dark matter and baryonic content of the simulation box are sampled in our model by using a discrete number N of particles. Each baryonic particle can be either in the form of gas or in the form of a stellar particle representing a single stellar population (SSP) of mass m and age t. We do not consider hybrid particles simultaneously hosting both a stellar and gas content. Star formation (SF) and gas restitution from stars are then modelled by turning gas into stars, or stars into gas, respectively.

Within the above scheme the chemical evolution model must provide us with procedures to compute: i) when and how gas particles are turned into stars (star formation); ii) when and how stellar particles are turned into gas (gas restitution); iii) the metal production of each stellar particle over a timestep Δt (metal production); and iv) how the chemical production of stars is released and mixed through the gas component (metal ejection and diffusion). We will now address each of these issues separately.

3.2.1 Star Formation

Star formation is commonly included in most SPH codes for galaxy formation. Different criteria have been proposed in the literature to decide when and how gas particles are turned into stars (e.g., Katz, 1992; Steinmetz & Muller, 1994; Yepes et al., 1997; Berczik & Petrov, 2001; Springel & Hernquist, 2003; Merlin & Chiosi, 2007). In our current implementation of SF we consider that gas particles are eligible to form stars if they are located in a region with a convergent flow and a gas density higher than a given threshold, ρ_{th}. In that case they are turned into stellar particles according to a Kennicutt–Schmidt law-like transformation rule (see Kennicutt, 1998; Silk, 2001),

$$\frac{d\rho_g}{dt} = -\frac{d\rho_*}{dt} = -\frac{c_*\rho_g}{t_g} \ , \tag{3.1}$$

where ρ_g and ρ_* are gas and stellar density, respectively, c_* is a dimensionless star-formation efficiency parameter, and t_g is a characteristic time-scale chosen to be equal to the maximum of the local gas-dynamical time $t_{dyn} = (4\pi G\rho_g)^{-1/2}$, and the local cooling time, $t_{cool} = u_i/\dot{u}_i$, where u_i is the internal energy. Eq. (3.1) implies that the probability p that a gas particle forms stars in a time Δt is

$$p = 1 - e^{-c_*\Delta t/t_g} \ . \tag{3.2}$$

As usual, we compute p at each time step for all eligible gas particles and draw random numbers to decide which of them form stars in the time interval $[t, t + \Delta t]$. Then, each of these randomly selected gas particles is transformed into one stellar particle.

3.2.2 Gas restitution

Once stars are present they return to the ISM part of their mass in form of chemically processed gas. As already mentioned, each stellar particle is treated as an SSP of total mass m and age t. Within each SSP, stellar masses are distributed according to a given Initial Mass Function (IMF), $\Phi(M)$. Throughout this paper we use the Chabrier (2003a) IMF with a mass range of $[M_l,\, M_u] = [0.1,\, 100]$ $\mathrm{M}_\odot$. Such an IMF is similar to other possible choices (e.g., Salpeter, 1955; Kroupa, 1998), but provides a better fit to counts of low-mass stars (Chabrier, 2003b; Bell et al., 2003).

Individual stars of mass M are characterised by a mean-lifetime $\tau(M)$. Therefore, within an SSP of age t, any star with $\tau(M) < t$ has already died so that part of its mass remains as a stellar remnant, M_r, while the rest should be in the form of gas ejected back to the ISM. The gas mass fraction, $E(t)$, of an SSP of age t is then given by:

$$E(t) = \int_{M(t)}^{M_u} \frac{M - M_r(M)}{M} \Phi(M)\, dM \ , \tag{3.3}$$

where M_u is the upper mass limit for stars in the IMF, and $M(t)$ is the mass of stars with lifetime t so that any individual star with $M > M(t)$ has already ejected a mass $M - M_r(M)$ of gas. We compute (3.3) by using the stellar mean-lifetimes $\tau(M)$ from the Geneva evolutionary tracks (Schaller et al., 1992) and the remnant masses $M_r(M)$ of Gavilán et al. (2005) for $M \leq 8M_\odot$, or Woosley & Weaver (1995) for $M \geq 8M_\odot$.

In a stochastic approach the above mass fraction of gas can be used to compute, at each timestep Δt, the probability that an entire stellar particle turns back into gas through a Monte Carlo method similar to that used for SF. Such a probability is given by (LPC02):

$$p_g = \frac{E(t + \Delta t) - E(t)}{1 - E(t)} = \frac{\int_t^{t+\Delta t} e(t')\, dt'}{1 - E(t)} \ , \tag{3.4}$$

where

$$e(t) = \frac{dE(t)}{dt} \tag{3.5}$$

is the instantaneous rate of total ejecta, while $[1 - E(t)]^{-1}$ is a correction factor that accounts for the stellar particles that have already turned to gas, so that the probability p_g is not computed for them anymore.

3.2.3 Metal production

We assume that initially all gas particles have a primordial composition. As part of stellar evolution, newly produced elements are released to the surrounding ISM, either as stellar winds or byproducts of supernovae (SNæ) explosions. We consider the evolution of the following elements: H, ^{4}He, ^{12}C, ^{13}C, ^{14}N, ^{16}O, ^{20}Ne, ^{24}Mg, ^{28}Si, ^{32}S, ^{40}Ca and ^{56}Fe.

For an SSP of age t, the instantaneous ejection rate of a given element i can be expressed as:

$$e_i(t) = p_i(t) + e(t)X_i \ , \tag{3.6}$$

where $p_i(t)$ is the ejection rate of the newly synthesised element i (i.e., the yield of i), while $e(t)X_i$ is the ejection rate of the element i already present when the SSP was formed from a gas particle with abundance X_i. All these rates are expressed as quantities per total mass unit.

As already quoted in § 3.1, the yield of any element i depends on the detailed abundances of all other species j. In order to take into account such a dependence we use the Q_{ij} formalism proposed by Talbot & Arnett (1973). Such a formalism links any ejected species to all its different nucleosynthetic sources, allowing the model to scale the ejecta with respect to the detailed initial composition of a star.

For an individual star of mass M, the mass fraction initially in the form of chemical species j, transformed and ejected as chemical species i, is written in the Q_{ij} formalism as:

$$Q_{ij}(M) = \frac{M_{ij,exp}}{M_j} = \frac{M_{ij,exp}}{X_j M} \ ,$$

where X_j is the initial abundance of j, whereas $M_{ij,exp}$ is the mass of i that was synthesised from j and finally expelled.

For a whole SSP, the contribution to $e_i(t)$ due to j is then given by

$$q_{ij}(t) = -Q_{ij}(M(t))\Phi(M(t))\frac{\mathrm{d}M}{\mathrm{d}t} \ ,$$

and, therefore, the total ejection rate of the chemical species i can be written as:

$$e_i(t) = \sum_j q_{ij}(t)X_j \tag{3.7}$$

and the yield of i can be obtained from Eqs. 3.6 and 3.7 as

$$p_i(t) = e_i(t) - e(t)X_i \ . \tag{3.8}$$

To compute $q_{ij}(t)$ we consider the element production from:

1. Enrichment from low and intermediate mass (LIM) stars. We assume that all stars with masses in the range 0.8 - 8 $M_\odot$ end their life, after an AGB or TP-AGB phase, by the loss of their envelope that is ejected to the ISM as enriched gas in the form of planetary nebulae. We use the set of stellar yields by Gavilán et al. (2005), which include the effects of the third dredge-up for the TP-AGB stage and of the hot-bottom burning processes. In this set the primary nitrogen contribution of the LIM stars is higher for low metallicities (Gavilán et al., 2006) and, simultaneously, the total nitrogen yield is lower than in other stellar yield sets (van den Hoek & Groenewegen, 1997; Marigo, 2001). Models using these stellar yields produce results in excellent agreement with observation of nitrogen from our Galaxy (halo and disk stars), from extragalactic HII regions, and from Damped-Lyman-Alpha galaxies (Gavilán et al., 2006; Mollá et al., 2006).

2. Type II supernovae (SNII). We assume that stars more massive than 8 $M_\odot$ produce SNII. For the chemical production we adopt the yields of Woosley & Weaver (1995)[2]. These yields include the elements produced in pre-supernova evolution and SNII explosions for metallicities between $Z = 0$ and $Z_\odot$ and masses between 11 and 40 $M_\odot$[3]. Unlike other sets (e.g., Portinari et al., 1998), these yields do not consider the contribution of stellar winds. As shown by Gavilán et al. (2005, 2006), when stars suffer mass loss from winds they eject large quantities of helium and carbon from their envelopes. This hinders the creation of oxygen and other heavier elements, and results in a low yield of oxygen and a high yield of carbon.

3. Type Ia supernovae (SNIa). We use the chemical yields from the W7 model by Iwamoto et al. (1999), tabulated for two different metallicities (solar and subsolar). The SNIa rates are computed according to Ruiz-Lapuente et al. (2000) who provided us with a numerical table (private communication) with the time evolution of the supernova rates for a single stellar population. These rates were derived for several combinations of possible candidates of binary system or SNIa (double degenerate, single degenerate, etc.), considering all parameters (secondary lifetimes, orbital velocities, distances between both stellar components, etc.) that determine the conversion of a binary system into an SNIa explosion.

[2]The Fe ejecta has been divided by 2, following Timmes et al. (1995)

[3]We extrapolate linearly for ejecta up to the upper mass limit considered (100 M⊙).

All the above sets of stellar yields are used as input data to construct the $q_{ij}(t)$ matrix according to the Ferrini et al. (1992) algorithm as updated in Gavilán et al. (2005). Such an updated algorithm is based on Galli et al. (1995) and Portinari et al. (1998).

3.2.4 Metal ejection and diffusion

Metal ejection

How the chemical elements are distributed and mixed in the ISM is a complex problem that takes place at scales much smaller than the resolution reached in cosmological simulations. Most SPH implementations of chemical enrichment do not consider gas restitution from stars. Therefore, at each timestep Δt, the metals produced by a stellar particle are distributed through the neighbouring gas by means of, e.g., SPH-spreading. This simple procedure fails however when the gas restitution from stars is considered. Indeed, the most straightforward way of restoring gas is to perform the opposite process of star formation, and turn whole stellar particles into gas. However, when a stellar particle of age t turns back into a gas particle, its metal production from stars with lifetimes longer than t has not been considered yet. If, at that timestep, such a remaining metal production is computed and distributed over the neighbouring gas, particles with an extremely high metallicity could result. Otherwise (i.e., if the remaining metal production is ignored), simulations including gas restitution would systematically underestimate the chemical enrichment. A straightforward procedure to circumvent this problem consists in introducing new gas particles and/or modifying the individual masses of particles to progressively account for the gas restitution from stars.

Within a scheme where both the individual mass and the total number of particles remain constant, as we consider here, the metal release from stars can be also addressed through a statistical approach like that proposed by LPC02. That is to say, we must evaluate the overall metal production of a large enough number N of stellar particles with similar ages and initial metallicities, so that they themselves constitute an SSP. The way in which individual particles release their metals must then ensure the right overall chemical evolution for the whole set of N particles. For example, a possible procedure suggested by LPC02 is based on the fact that, within a timestep Δt, a stellar particle of age t theoretically ejects an amount $\int_t^{t+\Delta t} e(t')\,dt'$ of gas with chemical abundances given by

$$X_i'(t) = \frac{\int_t^{t+\Delta t} e_i(t')\,d't}{\int_t^{t+\Delta t} e(t')\,dt'}\ . \tag{3.9}$$

This procedure then considers that, as long as a particle remains as a stellar one, there is no gas restitution and metals are not released to the surrounding gas. On the contrary, if such a particle turns back into gas at some timestep Δt, the chemical content of the resulting gas-again particle is updated so that it corresponds to the composition of the gas released at such timestep, given by Eq. (3.9). Over a sufficiently large number N of particles, constituting a whole SSP, this approach gives a fair representation of the overall metal production. The main limit of this method is that newly produced metals for a whole set of stellar particles are sampled by the few particles of different ages that turn back into gas within a given timestep, i.e., within a given cosmic age interval, $[t, t + \Delta t]$. Since the chemical composition of the gas released from an SSP is a function that strongly varies with time (see Figure 3.1), a large number of particles is then needed to obtain a meaningful sampling, but also to avoid strong statistical noise which could lead to excessively high scatter in the resulting distribution of abundances.

In order to reduce the above statistical noise we have implemented a different procedure, in such a way that the metals produced by any stellar particle at a given timestep $[t, t + \Delta t]$ are distributed through the neighbouring gas at this timestep (this procedure is similar to that used in previous SPH implementations of chemical enrichment without restitution). Actually, since we incorporate the diffusion of metals through the gas (see below), just the nearest gas neighbour receives the yields of a stellar particle during each timestep. Note that, since stars do not follow the motion of gas particles, the identity of such nearest gas neighbour can change from one step to another. The composition X_i' of the nearest gas neighbour[4] of a stellar particle of age t is updated according to:

$$\Delta X_i'(t) = \frac{\int_t^{t+\Delta t} p_i(t')\, dt'}{1 - E(t)} \ . \tag{3.10}$$

Here the yield $p_i(t)$ is given by (3.8) and the factor $[1 - E(t)]^{-1}$ converts yields per total mass unit to yields per stellar mass unit and then corrects for the missing metal production of stellar particles that were already transformed into gas. To see that is indeed the case, consider N_0 particles of mass m that become stellar particles at $t_0 = 0$. Such N_0 particles can be regarded as an SSP. For each chemical species i, the mass production by this SSP during the time interval $[t, t + \Delta t]$ is:

$$\Delta M_i(t) = mN(t)\Delta X_i'(t) \ , \tag{3.11}$$

[4]When a stellar particle is turned into gas, the resulting gas-again particle is considered as the nearest gas neighbour in that timestep.

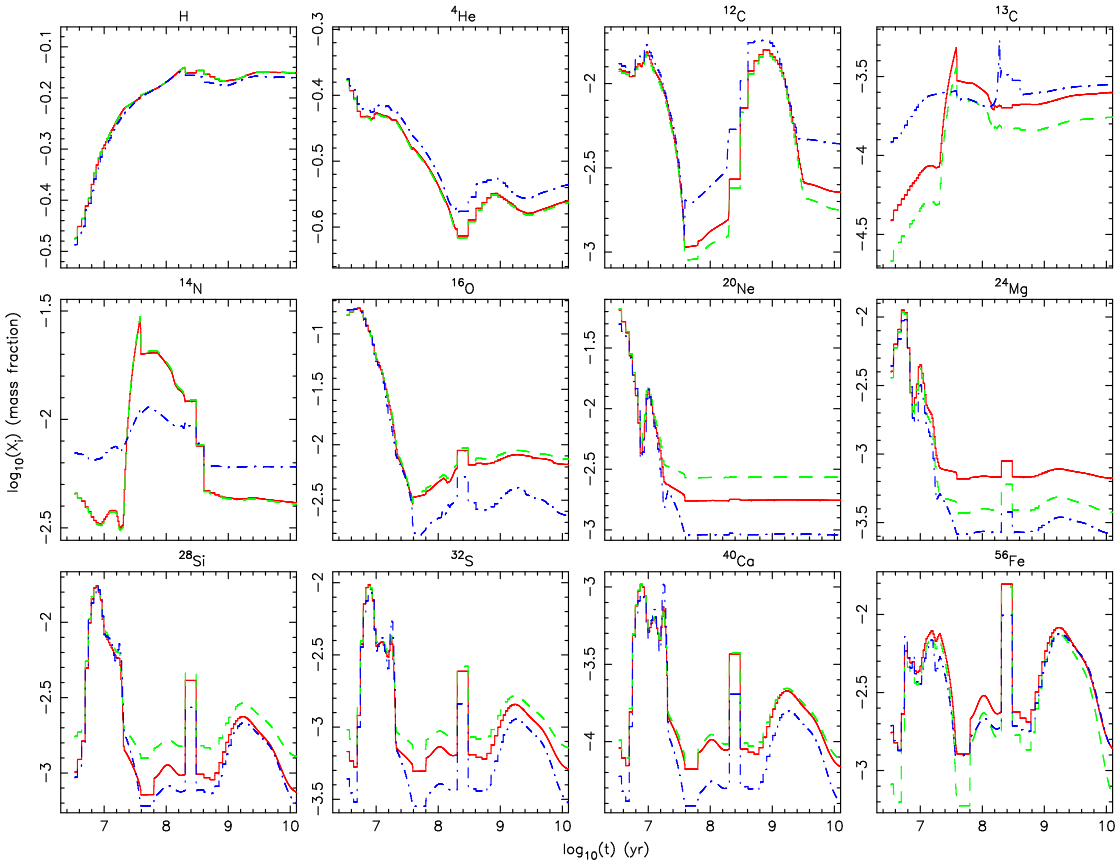

Figure 3.1: Composition of the ejecta as a function of time for three SSPs with solar total metallicity but different abundance ratios. The solid line corresponds to solar proportions, the dashed line to [O/Fe]=0.5, and the dashed-dotted line to [O/Fe]=-0.5. It can be seen how, even at identical total metallicity, in many cases the production of a particular isotope varies significantly. This effect is due solely to the use of the Q_{ij} matrix formalism, since the stellar evolution models used in this work only take into account the initial total metallicity, which is the same for the three compositions.

where $mN(t) = mN_0[1 - E(t)]$ is the actual stellar mass available at time t, after a fraction $E(t)$ of the stellar mass initially available at $t = 0$ has been transformed again into gas. Taking into account (3.10), we can write:

$$\Delta M_i(t) = mN_0 \int_t^{t+\Delta t} p_i(t')dt' \, , \tag{3.12}$$

and this is just the expression for the theoretical mass production during the time interval $[t, t + \Delta t]$ of the i-th element by the whole stellar mass in the SSP, mN_0.

Note also that, since the yield definition implies $\sum_i p_i(t) = 0$, Eq. (3.12) gives:

$$\sum_i \Delta M_i(t) = 0 \tag{3.13}$$

Therefore, when the composition of a gas particle is updated using (3.10), there is no mass exchange between such a gas particle and the neighbouring stellar particle that releases its metals. The mass of each particle remains then unaltered and the only mechanism transforming stellar mass into gaseous mass is still that described in § 3.2.2 for gas restitution.

Metal diffusion in the gas

Once the stellar production of metals has been released to the ISM, their redistribution through the gas component is governed by the turbulent motions of the gas. The turbulent mixing that takes place at subresolution scales can be properly modelled by a diffusion law at resolved scales (Taylor, 1921; Klessen & Lin, 2003).

$$\frac{\partial X_i}{\partial t} = D\vec{\nabla}^2 X_i \, . \tag{3.14}$$

The SPH formulation of the diffusion equation for a compressible fluid has been given by Monaghan (2005):

$$\frac{dX_i^a}{dt} = \sum_b K^{ab}(X_i^b - X_i^a) \, , \tag{3.15}$$

with

$$K^{ab} = \frac{m_b}{\rho_a \rho_b} \frac{4D_a D_b}{D_a + D_b} \frac{|\nabla_a W_{ab}|}{|\mathbf{r}_{ab}|} \tag{3.16}$$

where the subindexes a and b are used to denote different SPH particles. As a first approximation, in this paper we have considered a constant diffusion parameter $D_a = D_b = D$ for all the gas particles. Except in the first three synthetic tests of § 3.4.1, where

the instantaneous mixing of metals through the gas component is assumed, and in the diffusion test of § 3.4.1, we have adopted the value $D = 9.25 \times 10^{26}$ cm^2/s as suggested by LPC02.

In our code, the diffusion equation (3.15) is computed at each timestep by considering all the active gas particles a, and their active neighbours b[5]. By active particles at timestep $[t, t + \Delta t]$, we mean those needing the update of their physical properties at that timestep. In order to solve Eq. (3.15) it must be noted that metal diffusion would introduce a new time-scale $(X/\dot{X})_{\rm diff}$ and therefore, an additional criterion limiting the time stepping. Just like for the radiative cooling (see Serna et al., 2003), such an additional Δt-control criterion can be circunvented by solving Eq. (3.15) in integrated form. We have then used the fact that, because of the Courant condition, the density field (and hence K^{ab}) is nearly constant over a timestep. Therefore, Eq. (3.15) can be anallytically integrated to find:

$$\Delta X_i^a = X_i^a(t + \Delta t) - X_i^a(t) = \sum_b \Delta X_i^{ab} \tag{3.17}$$

with

$$\Delta X_i^{ab} = -\Delta X_i^{ba} = \frac{1}{2}\left(1 - e^{-2K^{ab}\Delta t}\right)\left(X_i^b(t) - X_i^a(t)\right) . \tag{3.18}$$

Such analytical expressions are those actually used in our implementation of the diffusion process.

3.2.5 Energy feedback from stellar processes

Energy feedback from supernova explosions has been implicitly included in our implementation, at least partially, through the choice of the SF efficiency parameters. Our model relies on the *turbulent sequential star formation scenario*. This model assumes that the interstellar medium is structured into different regions characterized by specific values of their physical variables.These structures are thought to form a multiscale hierarchy with different levels. Physical processes operate at different levels of this hierarchy to produce the ISM gas structure (e.g. Elmegreen, 2003, 2002). In particular, giant molecular clouds and molecular clouds are supported against gravity by turbulence and magnetic fields. Turbulence has a second role at this level: it produces gas compressions at lower scales. Compressed volumes can then fragment into clumps and dense cores, even if the cloud is globally stable because the average RMS speed is large enough to

[5]Only active gas particles are considered in order to maintain the symmetry and ensure the abundance conservation in the diffusion process

give global stability. The final step of the sequence is star formation from dense core collapse, locally triggered at this scale by supernova explosions and expanding shells, among other possibilities.

Not any dense core collapses into stars. A given core collapses when gravity overcomes its kinetical energy support. A density threshold for core collapse appears at this scale[6], ρ_c, as well as a SF efficiency, ϵ_c. The ISM gas structure can be described by means of the probability distribution function (PDF). Wada & Norman (2001, 2007) in their simulations of whole galaxy models have found a log-normal PDF. Stellar processes (stellar winds, SNæexplosions and similar processes) inject energy, momentum and metals into the ISM. This very likely results into molecular cloud destruction. However, as the bulk ISM may be stable and cloud-forming instabilities still operate in the cool phase, caused by turbulent compressions, this stellar self-regulation of SF may not be very effective.

Despite its complexity, SF (at least in disk galaxies) follows two simple empirical laws, that any deeper understanding of SF processes must explain: 1) the Kennicutt-Schmidt law for the SF rate (Kennicutt, 1998). It represents an average over $\sim$ disk scales, and, as an average, takes into consideration the whole complex physical processes involved into SF at disk scales. 2) Moreover, a density threshold at this scale empirically appears (Martin & Kennicutt, 2001). Concerning the explanation of these empirical laws, Elmegreen (2003, 2002) suggests that the Kennicutt-Schmidt law can be linked to the SF processes at the scale of dense cores through the PDF: the SF efficiency at a given scale is proportional to the fraction of gas at this scale verifying $\rho_{\rm g} > \rho_{th}$. Li et al. (2005a,b), on their turn, have reproduced the observed global and local Kennicutt-Schmidt laws, and, also, have obtained star formation thresholds in disk galaxies in their three dimensional SPH simulations of SF in disk galaxies where no stellar explicit feedback has been implemented. These works indicate that an agreement of astronomers about the precise role of stellar feedback in the setting up of the two laws above, among other SF characteristics, is far from being reached.

3.3 The composition-dependent cooling function

3.3.1 The cooling model

The publicly available MAPPINGS III code (see Sutherland & Dopita, 1993, hereafter SD93, for a much wider description) consists of a detailed cooling model for low and

[6]Note that these parameters are defined for core-scale processes and thus are not the same (although they are related) as the macroscopic ones previously defined.

high temperatures, which includes calculations for up to 16 atoms (H, He, C, N, O, Ne, Na, Mg, Al, Si, S, Cl, Ar, Ca, Fe and Ni) and all stages of ionization. In this code, the net cooling function of an optically-thin astrophysical plasma is obtained by adding the contribution of different processes: collisional line radiation (including fine-structure, inter-system, and forbidden emission), $\Lambda_{\rm lines}$, free-free and two-photon continuum radiation, $\Lambda_{\rm cont}$, recombination processes with both cooling and heating effects, $\Lambda_{\rm rec}$, photoionization heating, $\Lambda_{\rm photo}$, and collisional ionization, $\Lambda_{\rm coll}$.

$$\Lambda_{\rm net} = \Lambda_{\rm lines} + \Lambda_{\rm cont} \pm \Lambda_{\rm rec} - \Lambda_{\rm photo} + \Lambda_{\rm coll} \tag{3.19}$$

All the detailed cooling computations in this paper have been carried out by using MAPPINGS III. To obtain results easily comparable to those reported by SD93, widely used in cosmological simulations, we selected the algorithms and assumptions of its previous version. In addition, all these computations considered Collisional Ionization Equilibrium (CIE) conditions. Therefore, the photoionization heating is insignificant, leaving only collisional line radiation, continuum radiation, and recombination heating as significant terms.

3.3.2 Metallicity dependent cooling in cosmological simulations

In principle, the accurate value of the normalised cooling function[7] depends on both the local temperature and the detailed chemical composition:

$$\Lambda_N = \Lambda_N(T, \mathbf{Z}) \tag{3.20}$$

where

$$\mathbf{Z} = (Z_1, Z_2, ..., Z_N) \tag{3.21}$$

is a vector containing the abundance Z_i of the $N = 16$ chemical species taken into account by MAPPINGS for the cooling rate. In a cosmological simulation, one must deal with a huge number of gas particles with different metal mixtures. A full computation (e.g., by directly using MAPPINGS) of the cooling function of each particle according to its detailed chemical composition would be very expensive in terms of computing time.

To deal with the above difficulty, the most common approach consists of reducing the $\mathbf{Z}$ dependence of the cooling function into a much smaller number of parameters or,

[7] Please note that we define the normalised cooling rate as $\Lambda_N = \Lambda_{\rm net}/\rho^2$, instead of $\Lambda_N = \Lambda_{\rm net}/n_e n_t$, where n_e is the electron number density and n_t the total ion number density. The resulting units for Λ_N are erg cm^3 s^{-1} g^{-2}. This approach eases the computation of $\Lambda_{\rm net}$ in SPH codes.

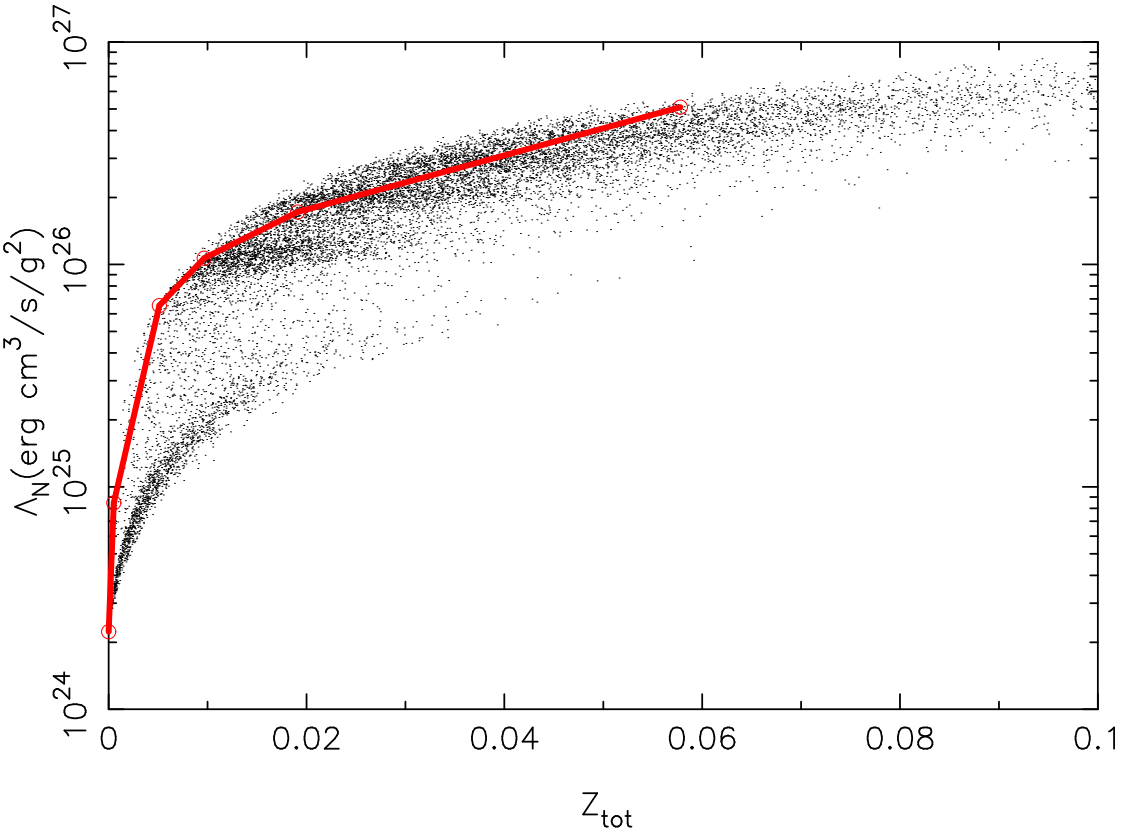

Figure 3.2: Cooling function dependence on the total metallicity Z for a given ($T = 10^{5.5}$ K) temperature for distribution of abundances present on a cosmological self-consistent simulation with metal enrichment. The solid line represents the cooling according to SD93.

ideally, into just one parameter ζ.

$$\Lambda_N = \Lambda_N(T, \zeta) \tag{3.22}$$

For example, SD93 have considered the total metallicity, $Z_{\rm tot}$, as their choice of ζ. More specifically, the cooling function is computed and tabulated by using chemical proportions interpolated, according to the total metallicity $Z_{\rm tot}$, between primordial and solar abundances. Such an approach allows for a fast implementation of a metallicity dependent cooling function in cosmological simulations.

In order to test the above approach, we have considered a sample of gas particles with different metal mixtures. Instead of assigning a random composition to each particle, we

have randomly selected $\sim 10^5$ particles extracted from cosmological ΛCDM simulations with the chemical evolution model described in § 3.2.

A full computation of the cooling function has been carried out for each particle by using MAPPINGS and its individual chemical composition. The dots in Figure 3.2 represent the individual values of the cooling function when the same temperature ($T = 10^{5.5}$) is assigned to all the gas particles in the sample. The solid line represents instead the cooling rate obtained from the SD93 method. It can be seen from this figure that the latter approach gives a reasonable approximation of the cooling rate at different $Z_{\rm tot}$ values. However, the figure also shows an important dispersion on the cooling rate of gas particles with the same total metallicity but different metal mixtures. Such a dispersion could lead to errors in the estimate of $\Lambda_T(\mathbf{Z})$ of almost one order of magnitude for sub-solar metallicities.

Different approaches can be envisaged to improve the modelling of the cooling function in cosmological simulations. For example by characterising the composition dependence of the cooling function with more than one parameter. This could be achieved by considering, in addition to the total metallicity, the alpha-element enhancement or any other parameter providing a more detailed description of the metal content. Another approach that needs to be explored consists of maintaining the Eq. (3.22), with just one metallicity parameter, but using a different choice of ζ to describe the effect on the cooling function of different chemical compositions.

In order to analyse this latter possibility, we have employed a Dimension Reduction Regression (DDR) technique (Weisberg, 2002). In such a procedure, one tries to reduce the multidimensional dependence of a function $\Lambda(\mathbf{Z})$ (e.g., the cooling function at a given temperature) to a small number d of parameters expressed as linear combinations $\zeta_1 = \mathbf{c}_1 \cdot \mathbf{Z}$, ..., $\zeta_d = \mathbf{c}_d \cdot \mathbf{Z}$, where $\mathbf{c}_i$ are vectors, of the same dimension as $\mathbf{Z}$, containing the coefficients of each linear combination ζ_i. If d is very small, one or two, then the regression problem can be summarised using simple graphics (a single $\Lambda(\zeta_1)$ plot for $d = 1$, or a 3D plot for $d = 2$) containing all the regression information.

Several methods for estimating d and the relevant coefficients $\mathbf{c}_1, ..., \mathbf{c}_d$ have been suggested in the literature. In this paper we have used a sliced inverse regression method (Li, 1991), where the range of Λ_T values is divided into several intervals, or slices, and then a weighted principal component analysis is performed. This gives higher importance to the slices with higher covariance. The eigenvectors of the covariance matrix, ordered by their corresponding eigenvalues, are the preferred directions (i.e. the d $\mathbf{c}_i$ vectors).

When the above algorithm is applied to the cooling function, one finds that just one

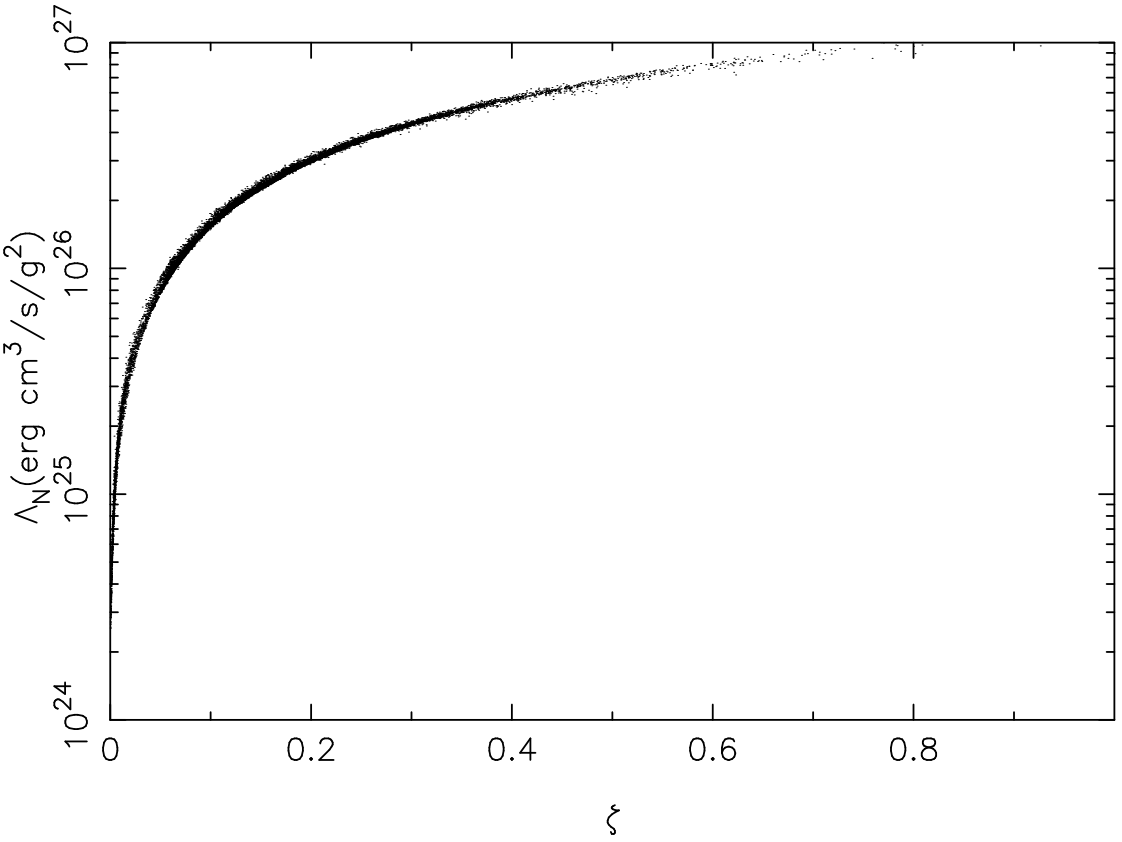

Figure 3.3: Cooling function dependence on the ζ_T parameter for a given ($T = 10^{5.5}$ K) temperature.

parameter

$$\zeta(T) = \mathbf{c}(T) \cdot \mathbf{Z} \tag{3.23}$$

is enough to accurately fit Λ_N at a given temperature T. For the sake of clarity, Table 3.1 gives the resulting $\mathbf{c}(T)$ coefficients for some temperature values and for the same metals as those considered in the yields of Gavilán et al. (2005). The metallicity parameter in Table 3.1 has been normalised according to $\zeta_N(T) = [\zeta(T) - \zeta_0(T)]\zeta_1(T)$ so that $\zeta_N(T)$ lies in the interval $[0, 1]$. The corresponding $\zeta_0(T)$ and $\zeta_1(T)$ normalisation parameters are also given in Table 3.1.

To check the above result, we have repeated the same test as in Figure 3.2. For each gas particle in the sample we have considered its detailed chemical content to determine its corresponding ζ parameter (Eq. 3.23), as well as to carry out a full MAPPINGS III computation of its individual cooling rate at $T = 10^{5.5}$ K. The dots in Figure 3.3

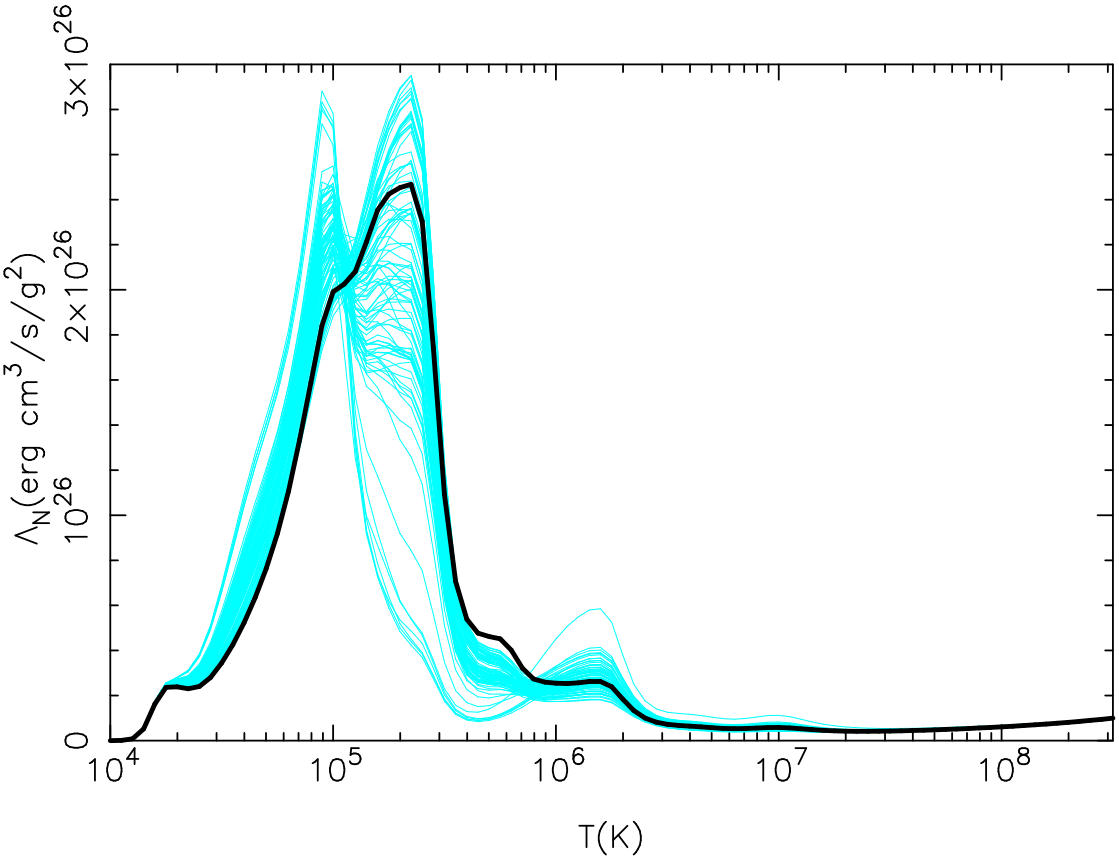

Figure 3.4: Cooling function for a sample of particles with solar metallicity ($Z = 0.02 \pm 0.0002$) but different metal mixtures as found in a cosmological simulation (thin lines). The thick black line represents the cooling function for solar abundances (Anders & Grevesse, 1989).

show the (Λ_j, ζ_j) values obtained for each particle j. It can be seen that such a plot now presents almost no dispersion and, therefore, the $\Lambda_N(T, \zeta)$ values can be easily and accurately tabulated (see Table 2).

Summarising, given a gas particle with known temperature T and chemical content $\mathbf{Z}$, its appropriate metallicity parameter $\zeta(T, \mathbf{Z})$ can be computed by using Eq. (3.23) and the coefficients of Table 3.1. An accurate estimate of the cooling rate can be then obtained through interpolation from Table 3.2. The resulting algorithm needs an almost negligible amount of computing time but implies a remarkable improvement on the cooling modelling, as compared to other approaches based on $Z_{\rm tot}$. Indeed, we have

applied this algorithm to a sample of simulated gas particles with $Z_{\rm tot} = Z_\odot$ but different chemical contents. Figure 3.4 shows their corresponding cooling functions (thin lines), as well as the cooling function (thick line) obtained for solar abundances (i.e., in the case considered by SD93).

The physical meaning of the $\mathbf{c}(T)$ values obtained in the above DDR procedure can be understood as coefficients giving, at a given temperature T, the weight of each element on the total cooling function. For example, Figure 3.5-a shows the logarithmic partial derivative of Λ_N with respect to the abundance of each element, i.e., a quantity roughly giving the weight of each element on the total cooling function. Figure 3.5-b shows instead the contribution $\zeta_i = c_i Z_i$ of each element i to the metallicity parameter $\zeta(T)$. In both panels, solar proportions have been assumed. It can be seen from this figure that both quantities are correlated, with the most important coolants contributing more to the metallicity parameter $\zeta(T)$.

It is important to note that, in SPH simulations, specific internal energy u is tracked instead of temperature T. Both are related by

$$u_T(\mathbf{Z}) = \frac{3}{2\bar{\mu}m_p} k_B T \ , \tag{3.24}$$

where k_B is Boltzmann's constant, m_p is the proton mass and $\bar{\mu}$ is the mean molecular mass. For simplicity, some SPH codes fix $\bar{\mu}$ to a constant value regardless of metallicity. In some cases (e.g., Kawata & Gibson, 2003) such a constant value is chosen to represent a fully ionised gas ($\bar{\mu} = 0.6$), while in other cases (e.g., Berczik, 1999) the adopted value represents a cool gas with primordial ($\bar{\mu} = 1.2$) or solar ($\bar{\mu} = 1.3$) abundances. To be consistent with our aim of developing a model that takes into account the full dependence on the chemical composition, we have preferred to consider the mean molecular mass as a function of T and $\mathbf{Z}$. Consequently, we have applied a DDR procedure similar to that of Eq. (3.22) to write $u(T, \mathbf{Z})$ as a linear combination of $\mathbf{Z}$. The corresponding DDR coefficients are also available online.

3.4 Tests and results

3.4.1 Synthetic tests

In order to test the results of our model, as well as the resolution effects, we have carried out a series of tests based on classical evolution models for chemical evolution. In all these tests, particles are just discrete mass elements submitted to certain constraints.

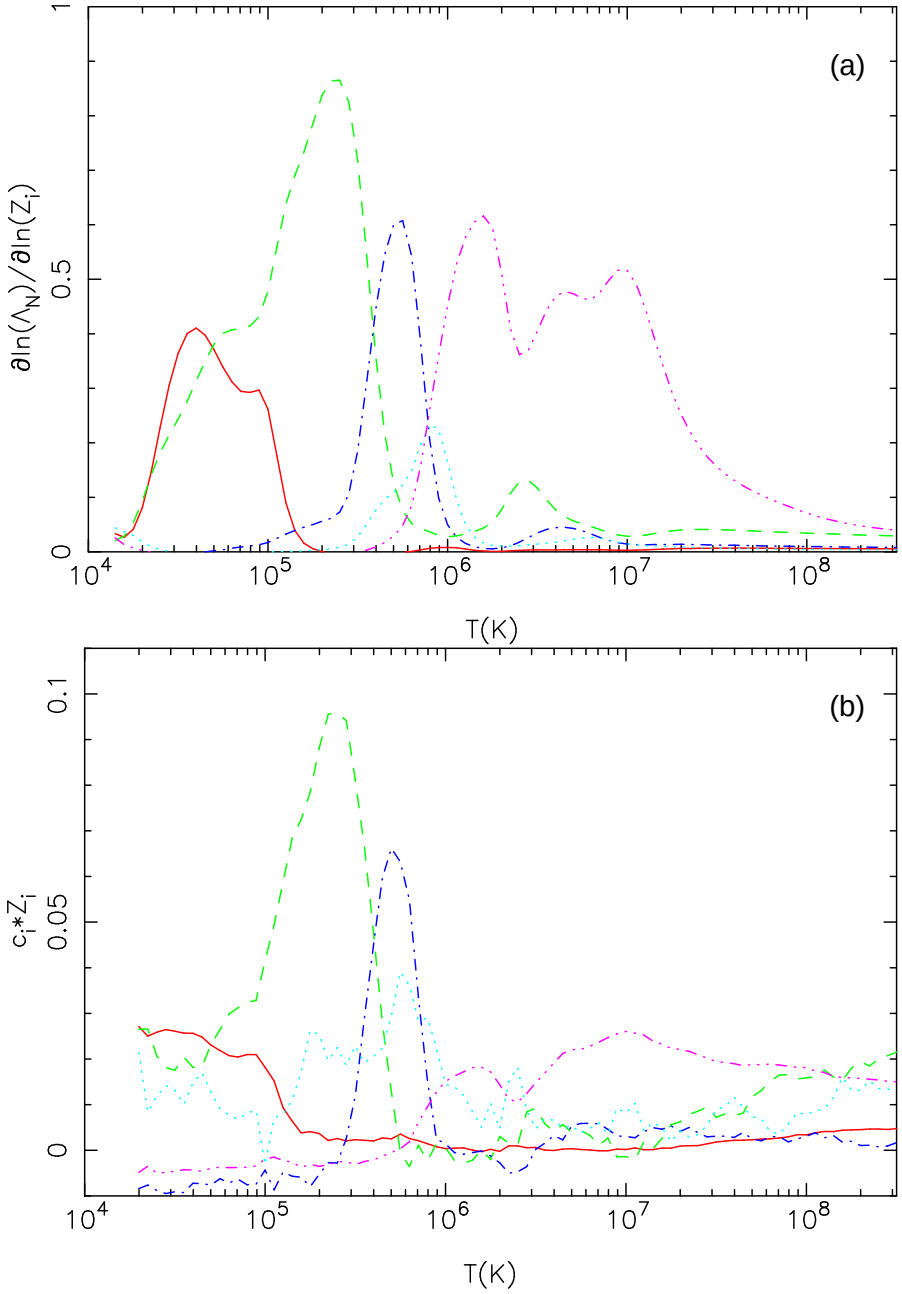

Figure 3.5: **(a)**: portion of the total cooling function contributed by C (solid line), O (dashed line), Ne (dashed-dotted line), Mg (dotted line) and Fe (dashed-triple dotted line) for a solar mixture of elements ($\mathbf{Z} = \mathbf{Z}_{\odot}$). **(b)**: corresponding values of the $c_i Z_i$ terms of ζ_T.

Therefore the models presented in this section are useful to test the different aspects of our implementation of the metal enrichment, uncoupled from any dynamical effect.

A single stellar population

Following LPC02, a first basic test consists of analysing the chemical evolution in the simple case of a single burst of star formation. Such a test is designed to check the validity of our statistical approach by comparing its results to the expected chemical production of an SSP.

The single-burst model begins with $N = 5000$ newly born star particles of total mass 10^{11} $M_{\odot}$. All particles have primordial composition at $t = 0$ and are left to evolve afterwards according to the statistical prescriptions for gas restitution and metal enrichment described in § 3.2. Consequently, as time progresses, some stellar particles will turn into gas. At each time step, the metal content of the gas component is enriched through the yields of the remaining stellar particles according to either Eq. (3.9) or (3.10). In this test, metals are instantaneously mixed through the gas component and no further SF episodes take place.

Figure 3.6 displays, as a function of time, the gas mass fraction and the chemical composition of the gas. The solid lines correspond to the exact analytical predictions for an SSP (i.e., those obtained in the continuous limit by directly integrating Eqs. 3.3 and 3.10 for a unique SSP). The dashed and dotted-dashed lines give instead the results obtained from a statistical model of chemical evolution based on Eq. (3.10) and Eq. (3.9), respectively. It can be seen from this figure that both statistical methods closely reproduce the expected trends for an SSP. Therefore, our scheme of progressive metal ejection (Eq. 3.10) gives, within a stochastic model, a fair representation of the overall production of an SSP.

Closed box model of an elliptical galaxy

Another useful test for chemical evolution models is the closed box model (Pagel, 1997) with one zone. We have implemented such a test by initially considering N gas particles that, during the simulation, randomly turn into stars according to a pre-defined probability. More specifically, in order to mimic an elliptical galaxy, we have considered an exponentially decaying star formation rate:

$$\psi(t) = \kappa e^{-\tau t}\,, \tag{3.25}$$

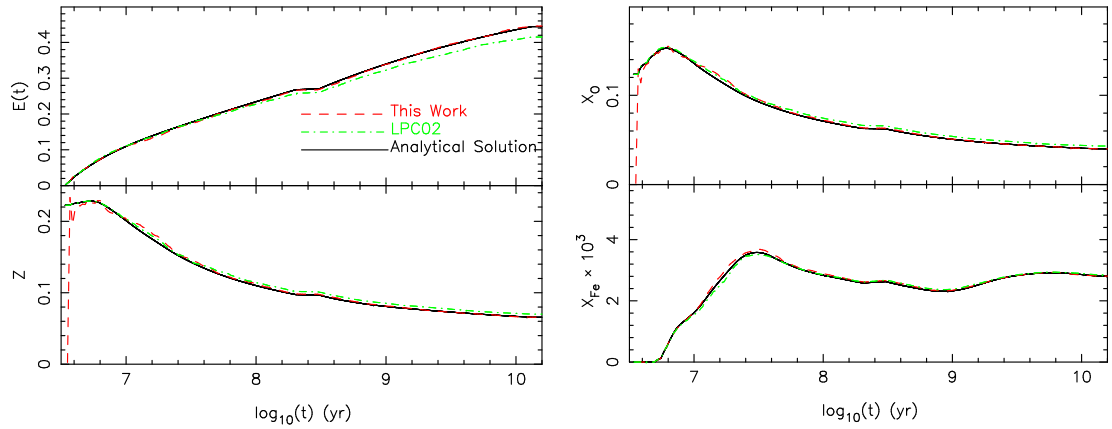

Figure 3.6: Results of the SSP test: time evolution of the total gas ejection $E(t)$, total metallicity of the ejected gas, Z, oxygen and iron fraction in the ejected gas

so that, assuming no gas feedback, the rate of change of the gas mass fraction, $g(t)$, is given by

$$dg(t)/dt = -\psi(t)\,. \tag{3.26}$$

The above equation implies that the probability p that a gas particle forms stars in a time Δt is

$$p = \frac{\left(e^{-\tau\Delta t} - 1\right)\kappa}{\kappa + e^{\tau t}(\tau - \kappa)}\,, \tag{3.27}$$

where κ can be written in terms of the final fraction of gas, g_1:

$$\kappa = \frac{\tau e^{\tau}(g_1 - 1)}{1 - e^{\tau}}\,. \tag{3.28}$$

As in the previous test, all particles are left to evolve according to the statistical model for gas restitution and metal enrichment described in § 3.2, except that here we use Eq. (3.27) to compute p at each time step for all gas particles and draw random numbers to decide which particles actually form stars. We again consider that metals are instantaneously mixed through the gas component.

The above closed box model then gives a simple representation of objects with a more complex sequence of star formation bursts and, therefore, containing a mixture of different SSPs. The main advantage of this model is that it has a known theoretical prediction for the resulting metal distribution function (MDF) of the gas component (see Appendix A of this chapter). The comparison with such a theoretical MDF then constitutes a strong test, uncoupled from hydrodynamic and gravitational effects, of the stability of particle-based numerical methods against a degraded resolution.

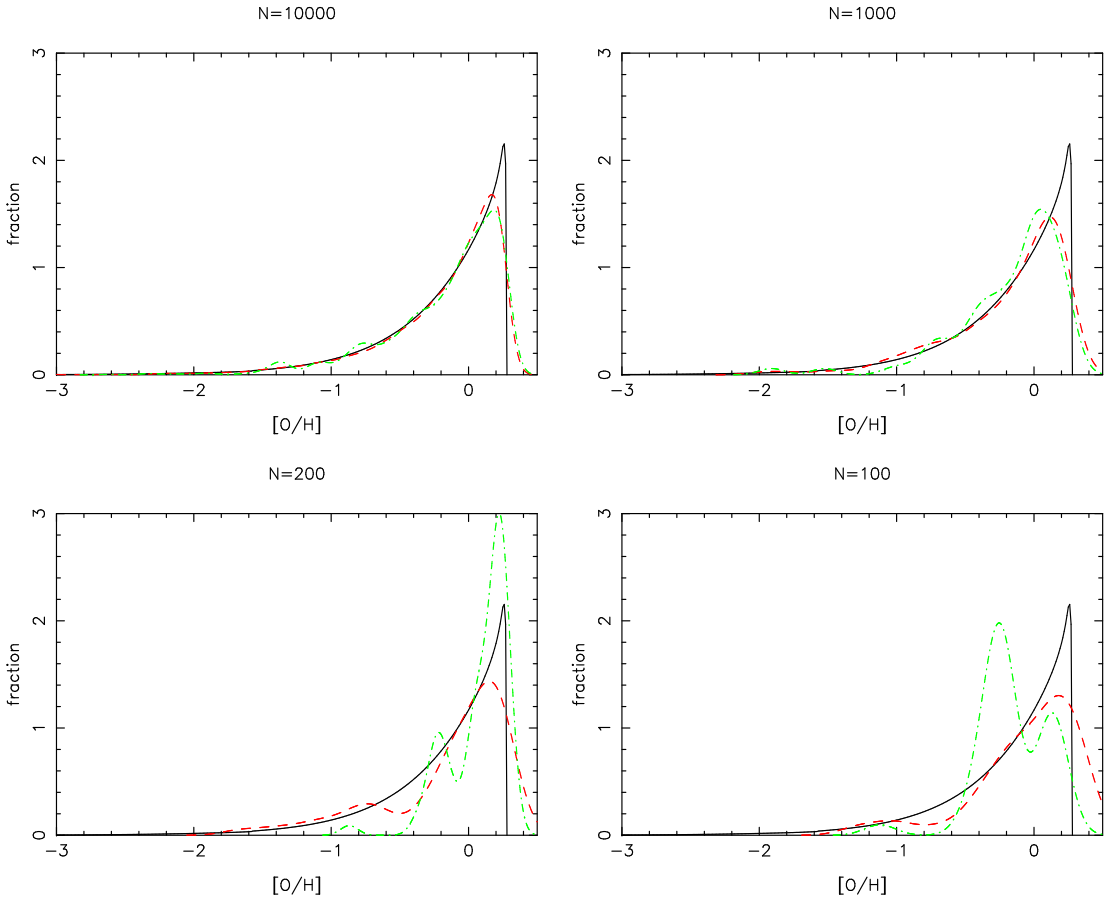

Figure 3.7: Metallicity Distribution Function (MDF) for the stellar particles in the closed box test. The different panels correspond to a decreasing number of particles (N =10000, 1000, 200 and 100) and, therefore, to a decreasing mass resolution. In order to make easier the comparison of the different curves, the particle-based MDFs are displayed as kernel-smoothed distributions with the bandwidth, $h = 1.06\sigma N^{-1/5}$, where σ is the standard deviation of the sample, as suggested by Scott (1992). The solid line corresponds to the analytical solution, the dashed-line to the numerical results obtained from Eq. (3.10), and the dotted-dashed line to those found from Eq. (3.9).

We have run this test for four different particle numbers (N = 10000, 1000, 200 and 100). In all runs we considered $\tau = 1/5$ Gyr^{-1}, a typical value for massive elliptical galaxies, and a constant timestep of $\Delta t = 1.38\ 10^6$ yr (i.e., 10000 integration steps over a Hubble time). In order to have enough resolution for the gas component, we have used a high value ($g_1 = 0.4$) for the final gas fraction. In a series of runs we have used Eq. (3.9) to incorporate the stellar production of metals into the gas component, whereas in another series of runs we have used the new procedure proposed in this paper (Eq. 3.10) to account for the metal feedback. Figure 3.7 shows the results of this test, where the solid line corresponds to the theoretical MDF, whereas the particle-based predictions are shown as dashed (for Eq. 3.10) and dotted-dashed (for Eq.3.9) lines. As can be seen from Figure 3.7, for a high number of particles (N = 10000) both procedures for metal feedback lead to MDFs in good agreement with the theoretical solution. Obviously, the kernel procedure used to draw the particle-based results leads to MDFs where the sharp peak and cutoff of the theoretical solution at [O/H] ~ 0.23 are smoothed. In tests with N = 1000 particles, both metal feedback procedures still give results in reasonable agreement with the theoretical solution, although the statistical noise is slightly less visible in the predictions obtained from Eq. (3.10) than in those found from Eq. (3.9). At low particle numbers (N = 200 and 100), the results from Eq. (3.10) degrade sensibly better and keep the shape of the MDF almost unaltered, while those from Eq. (3.9) become noise-dominated due to the lack of enough sampling data.

Multi-zone model of a Spiral Galaxy

In order to test our implementation of the Q_{ij} formalism, we have also performed a test based on the Mollá & Díaz (2005) multi-zone evolution model for a disk galaxy. Such a model also considered the Q_{ij} formalism and used the same stellar libraries as in our code. To ensure that our results are directly comparable to those of Mollá & Díaz (2005) and Gavilán et al. (2005), we have adopted the same IMF (Ferrini et al., 1990, 1992) for this test as that used in such studies.

The Mollá & Díaz (2005) model considers a galaxy with a spherical halo of radius R_H and a concentric cylinder constituting the disk. The spherical halo is divided into concentric cylindrical regions 1 kpc wide with a height determined by the corresponding galactocentric distance on the disk and the total radius of the sphere. The corresponding regions on the disk are also concentric cylindrical shells 1 kpc wide, but with a constant height $h_D = 0.2$ kpc.

In the initial conditions, the halo contains the total mass of the galaxy in gas phase.

The halo mass has a radial distribution consistent with the rotation curve of Persic et al. (1996). In units of 10^9 $M_\odot$, such a distribution is given by $M(R) = 2.32 \times 10^5 R V(R)^2$, with

$$V(R) = V_{opt}\left[0.72\frac{1.97x^{1.22}}{(x^2+0.61)^{1.43}} + 1.07\frac{x^2}{x^2+2.25}\right]^{1/2}. \quad (3.29)$$

Here, $x = R/R_{opt}$ and $R_{opt} = R_H/2.5$. We have considered $V_{opt} = 200$ km/s, $R_{opt} = 13$ kpc and $L = 10^{10.4} L_\odot$, which correspond to galaxies similar to the Milky Way.

For each region i the matter in the halo can be either in the form of stars of diffuse gas, with total mass M_{sh} and M_{gh}, respectively. In the corresponding disk region, the model allows for the following phases: diffuse gas (M_{gd}), clouds (M_{cd}), and stars (M_{sd}). In this latter phase, the adopted IMF implies a certain mass M_{s2} of stars with $M > 8$ $M_\odot$[8]. The mass of the different phases can change through the following conversion processes: i) Diffuse gas infall from the halo to the disk, with a rate $\dot{m}_{INF}$, ii) In the halo, star formation from diffuse gas ($\dot{m}_{SFH}$), iii) In the disk, star formation from clouds ($\dot{m}_{SFD}$), either from cloud-cloud collisions and from massive star-cloud interactions, and iv) Cloud formation from diffuse gas in the disk ($\dot{m}_{CFD}$). The complete set of equations for each zone is therefore (see Molla et al., 1996, for details):

$$\begin{aligned} dM_{gh}/dt &= \dot{W}_H - \dot{m}_{INF} - \dot{m}_{SFH} \\ dM_{sh}/dt &= \dot{m}_{SFH} - \dot{W}_H \\ dM_{sd}/dt &= \dot{m}_{SFD} - \dot{W}_D \\ dM_{cd}/dt &= \dot{m}_{CFD} - \dot{m}_{SFD} \\ dM_{gd}/dt &= \dot{m}_{INF} - \dot{m}_{CFD} + \dot{W}_D \end{aligned} \quad (3.30)$$

where W_H and W_D represent the gas return rate for the halo and disk, respectively, and

$$\begin{aligned} \dot{m}_{INF} &= M_{gh}/\tau \\ \dot{m}_{SFH} &= K M_{gh}^{1.5} \\ \dot{m}_{CFD} &= \mu M_{gd}^{1.5} \\ \dot{m}_{SFD} &= H M_{cd}^2 + \epsilon_a M_{cd} M_{s2} \end{aligned} \quad (3.31)$$

with $\tau = \tau_c \exp[(R - R_c)/\lambda_D]$, $K = \epsilon_K (G/V_H)^{1/2}$, $\mu = \epsilon_\mu (G/V_D)^{1/2}$, and $H = \epsilon_H/V_D$. Here, $R_c = R_{opt}/2$, $\lambda_D = 0.15 R_{opt}$, G is the universal gravitational constant, V_H is the volume of the halo region and V_D is the volume of the disk region. We have considered

[8]Note that the mass of massive stars in an SSP, M_{s2}, declines with the SSP age and eventually drops to zero.

parameter values that correspond to a galaxy mimicking the Milky Way: $\tau_c = 4$ Gyr, $\epsilon_K = 5.3\,10^{-3}$, $\epsilon_\mu = 0.80$, $\epsilon_H = 0.28$ and $\epsilon_a = 0.83$.

The above model has been implemented by considering 16 regions in the disk, from $R = 2$ kpc to $R = 18$ kpc. We explicitely avoid the bulge since our model is not applicable there. Each region is sampled with

$$N = 1000 \max\left[1,\ \frac{1}{1-\exp(-1/\tau)}\right] \tag{3.32}$$

particles of individual mass $M(R)/N$. All particles are initially labelled as diffuse gas in the halo so that, except for M_{gh}, all phases have a vanishing total mass. At each timestep Δt, the rate of change for the mass of the different phases is computed using Eqs. (3.30)-(3.31). The corresponding change on the mass M_i of each phase i is then computed at the first level of approximation, $\Delta M_i = (dM_i/dt)\Delta t$, and then expressed as discrete changes in the numbers of particles. After re-labelling the particles, our routines for chemical evolution are called to compute the metal production and return of gas (terms W_H and W_D in Eqs. 3.30) in both the halo and the disk, except for the star formation, which is computed in this text from Eq. (3.31).

Figure 3.8 compares our results and those found by Mollá & Díaz (2005) at $t = 13.72$ Gyr. We see from this figure that the radial distribution of the different elements and model components obtained from our code are in close agreement with those of Mollá & Díaz (2005). The small deviation of the oxygen and carbon abundance at the outer galactic regions is probably due to the fact that our approach is based on masses that are sampled by a discrete number of particles. Both methods give also very similar results for the time evolution of the oxygen and carbon abundance in the gas for the solar cylinder.

Figure 3.9 shows the time evolution of the stellar [O/Fe] ratio obtained from the Q_{ij} formalism (dashed line) as compared to that found when the Q_{ij} formalism is not used (dashed-dotted line). This latter result has been computed, for each stellar particle with composition X_j, by using in Eq. (3.7) effective abundances X'_j scaled, assuming solar proportions, according to its total metallicity. We see from this figure that the latter procedure underestimates the [O/Fe] ratio. This is due to the fact that forcing solar proportions for a stellar particle with [O/Fe]> 0 implies the use in Eq. (3.7) of a larger effective abundance of iron ($X'_{\rm Fe} > X_{\rm Fe}$). Consequently, when computing the ejection of iron $e_{\rm Fe}(t)$, the dominant affected term in Eq. (3.7) is $q_{\rm Fe,Fe}X'_{\rm Fe} > q_{\rm Fe,Fe}X_{\rm Fe}$, and $e_{\rm Fe}(t)$ is overestimated. Although less significantly, similar arguments imply that the ejection of oxygen is underestimated. These two effects can also be noticed in Figure 3.1 and

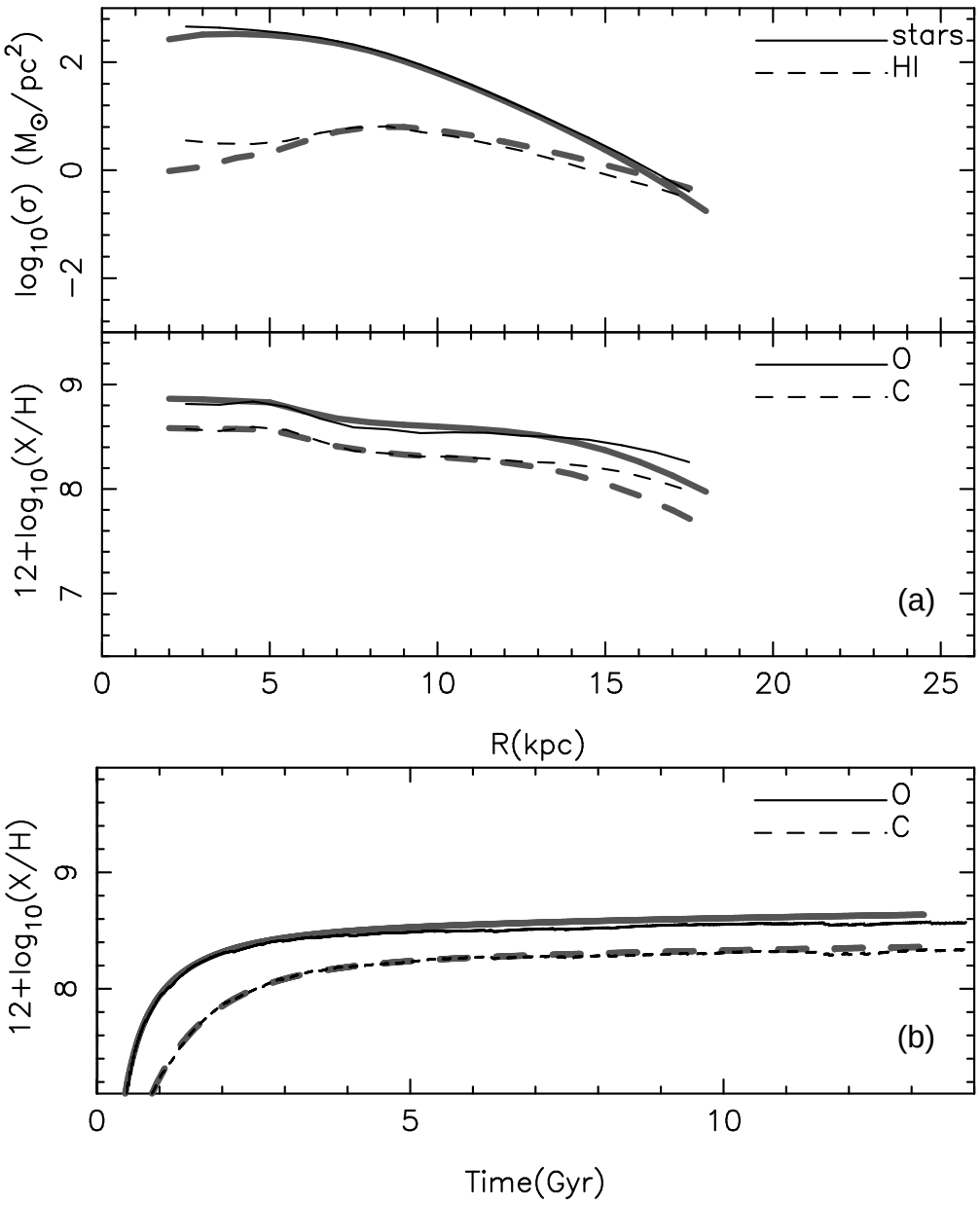

Figure 3.8: Comparison of our results (thin lines) and those found by Mollá & Díaz (2005) (thick lines) in their multi-zone model of a spiral galaxy. **(a)** Top panel: radial distributions of atomic gas, molecular clouds and stellar density at the end of the run. Bottom panel: radial distributions of oxygen and carbon. **(b)**: Time evolution of oxygen and carbon abundances in the gas for the solar cylinder.

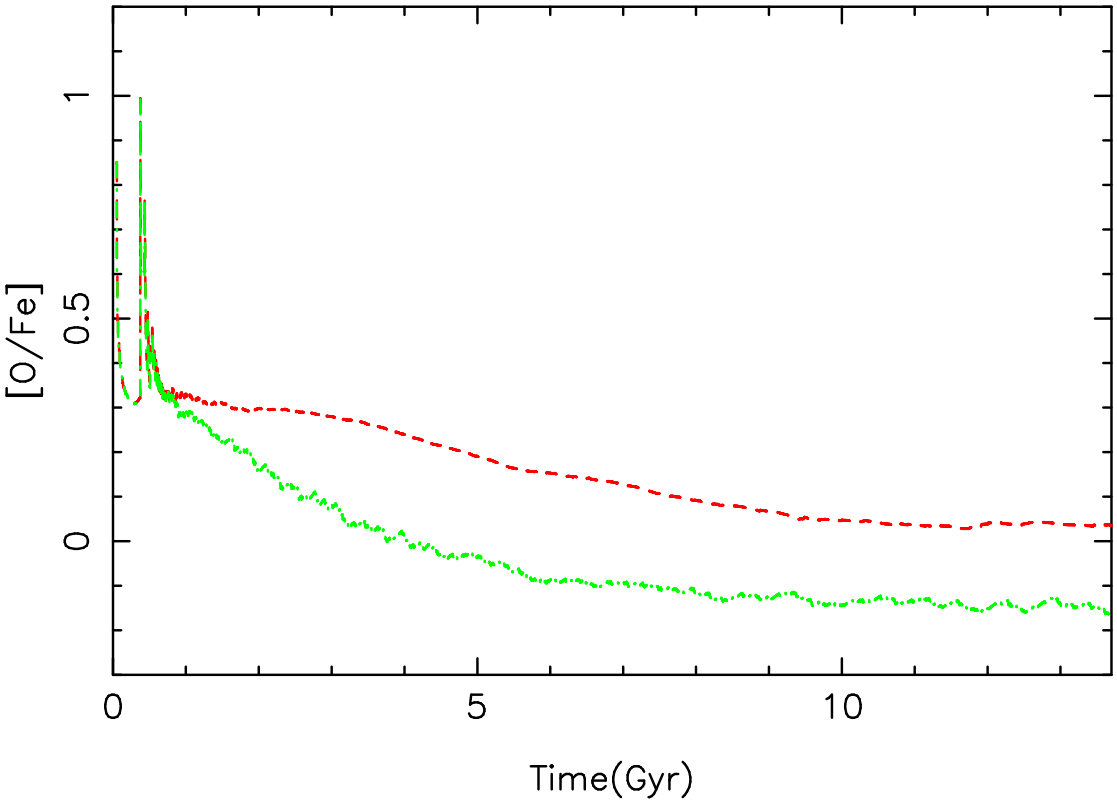

Figure 3.9: Time evolution of the [O/Fe] ratio of stellar particles in the solar cylinder. The dashed line corresponds to the result obtained from the Q_{ij} formalism. The result displayed as a dashed-dotted line has been obtained by computing the metal production of each stellar particle using its total metallicity and assuming solar proportions.

result in the underestimation of the [O/Fe] ratio observed in Figure 3.9.

Diffusion in a homogeneus box

The diffusion of metals in our model remains to be tested. In order to test our implementation of Eq. (3.14), described in § 3.2.4, we have devised a simple test. Starting with an isolated cubic box of $L = 1.43$ Mpc filled with 32^3 particles, distributed on a regular grid and representing a cloud of homogeneous gas with density $\rho = 1.058 \times 10^{-35}$ g/cm^3, we pollute the central particle with a metallicity of $Z = 0.1$, and let diffusion algorithm act for 13.72 Gyr. A diffusion constant of $D = 4.63 \times 10^{29}$ cm^2/s has been used, and no other processes have been considered, so that the particles are kept fixed

to the grid.

This simple setup allows for an analytical solution of the diffusion equation with initial conditions

$$X(\mathbf{r}, t = 0) = 0.1\delta(\mathbf{r}) \ , \tag{3.33}$$

namely

$$X(\mathbf{r}, t) = \int X(\mathbf{r}', 0) \frac{1}{(4\pi D t)^{3/2}} e^{-(\mathbf{r}-\mathbf{r}')^2/4Dt} \mathrm{d}\mathbf{r}'^3 \ . \tag{3.34}$$

While initial conditions of Eq. (3.33) cannot be imposed in a discrete model, both should converge if r or t are big enough.

In fact, the upper panel of Figure 3.10 shows the comparison between the final metallicity profile of the numerical test and its corresponding analytical solution. We find a good agreement for such a high t. Lower panel shows the metallicity time evolution in a bin centered around $r = 200$ kpc. We find the numerical solution to have a shallower growth than the analytical one, due to the fact that the numerical initial conditions are not an exact delta function. At later times, however, both solutions converge.

3.4.2 Cosmological simulations

We have finally performed different simulations of galaxy formation and chemical enrichment within a cosmological context. All simulations started at redshift $z = 20$ from initial conditions that are a Montecarlo realisation of the field of primordial fluctuations to a concordance cosmological model (a flat ΛCDM model, with $h = 0.7$, $\Omega_\Lambda = 0.7$, $\Omega_\mathrm{m} = 0.3$ and $\Omega_\mathrm{b} = 0.04$). The σ_8 value has been taken slightly high ($\sigma_8 = 1$) in order to mimick an active region of the universe (Evrard et al., 1990). The evolution of these fluctuations was numerically followed up to $z = 0$ by means of the parallel version of the DEVA code (see Serna et al., 2003, for a detailed description of DEVA) where we have coupled our model for chemical evolution and cooling. In the test performed in this section we have used a star-formation threshold of $\rho_{th} = 3 \times 10^{-25}$ g/cm^3, an efficiency of $c_* = 0.3$, a gravitational softening of $\epsilon = 1.5$ kpc$/h$ and $N = 2 \times 64^3$ particles in a box of $L = 7$ Mpc$/h$, implying a mass resolution of $m_b = 2.06 \times 10^7$ M$_\odot$ for baryonic particles and $m_{dm} = 1.34 \times 10^8$ M$_\odot$ for dark matter particles.

Individual galaxy-like objects of different morphologies naturally appear in these simulations as a consequence of the cosmic mass assembly and the physical processes taken into account. Differently from the semi-analytical models of § 3.4.1, no assumptions are made about the spatial variations of the infall rate of gas and its relative importance as compared to the star formation rate.

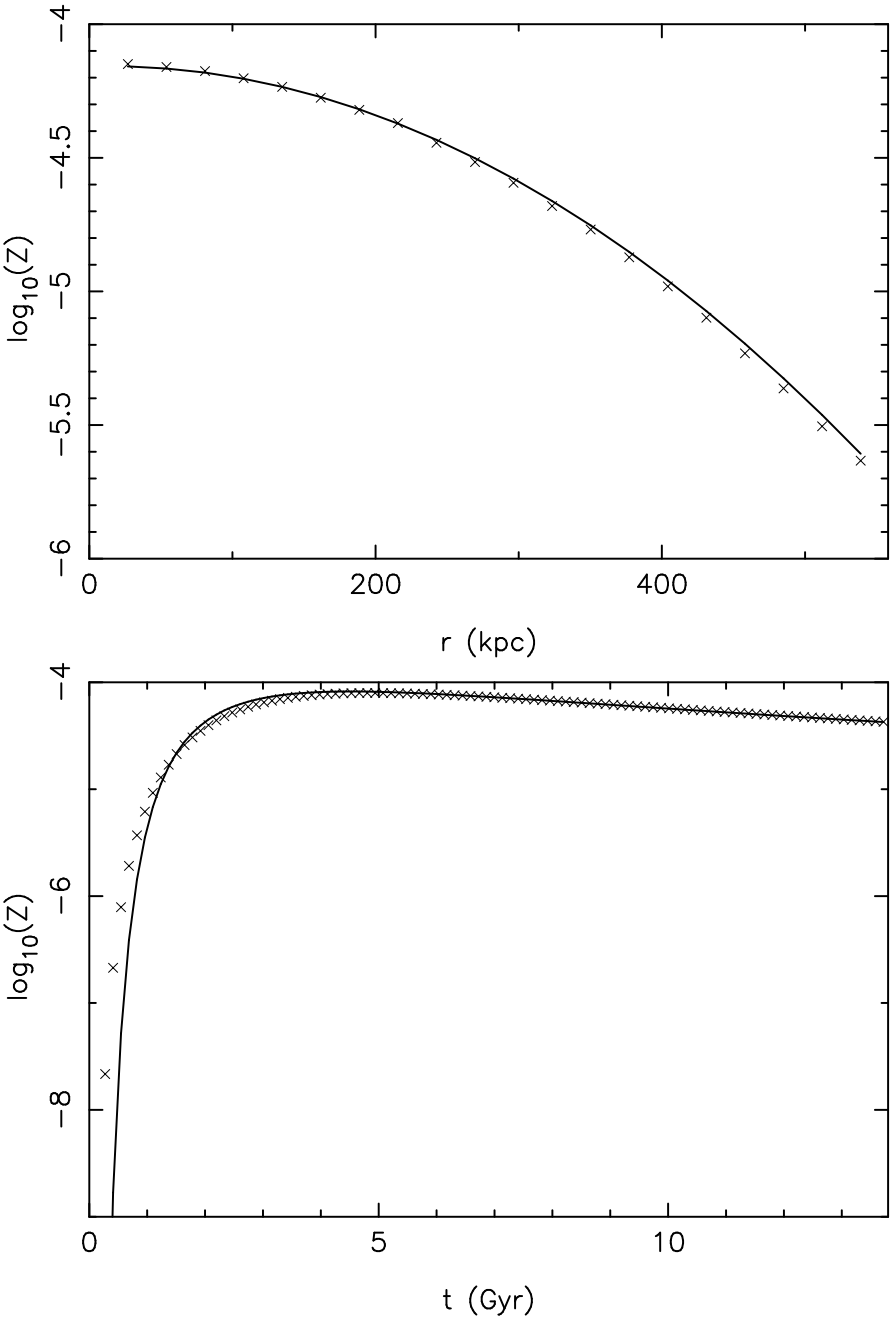

Figure 3.10: Upper panel: final spherical distribution of metallicity for the diffusion test (crosses) and analytical solution (solid line) for $t = 13.72$ Gyr. Lower panel: time evolution of the metallicity at $r = 200$ kpc.

These simulations then constitute an appropriate test to analyse: i) whether the resulting galaxy-like objects have realistic chemical properties; ii) the possible effects of including the cooling function presented in § 3.3, that takes into account the full dependence on the detailed chemical composition of gas particles; and iii) the importance of using the Q_{ij} formalism in cosmological simulations. In order to address these issues we have carried out different runs. In a first run (referred as the ζ-cooling run) we used the composition-dependent cooling of § 3.3, whereas in a second run (referred as the $Z_{\rm tot}$-cooling run) we used the total metallicity-dependent cooling of SD93. In both cases, we used the Q_{ij} formalism of § 3.2. In a third run (referred as the no-Q_{ij} run), the metal production of each stellar particle was instead computed by using its total metallicity and assuming solar proportions.

Elliptical-like objects (ELOs) constitute a family of objects with simple scaling relations (see Oñorbe et al., 2005, for a study of the origin of the Fundamental Plane of ELOs obtained in DEVA simulations). In this work, we focus on the study of ELOs because given their simplicity, less resolution is needed to properly simulate them. ELOs were identified as those objects having a prominent stellar spheroidal component with hardly disks at all. Here we will focus on the analysis of the chemical properties of the most massive ELOs at $z = 0$, sampled with at least 1000 baryonic particles. This selection criterion produces eight massive ELOs, with a stellar mass range of $\sim 3\times10^{10}-1.5\times10^{11}$ $M_{\odot}$.

In both the ζ-cooling and $Z_{\rm tot}$-cooling runs, we found that ELOs have metallicities with individual mean values that are consistent with those observed for elliptical galaxies with similar masses (Thomas et al., 2005). For example, Figure 3.11 shows the age-metallicity relation and metallicity distribution function (MDF) for the most massive ELO ($M = 1.5 \times 10^{11}$ $M_{\odot}$) identified in such simulations. We have found that the age-metallicity relation obtained for this object in the ζ-cooling (shown in the upper panel of Figure 3.11) is almost indistinguishable from that found in the $Z_{\rm tot}$-cooling run. Such a relation shows a very fast enrichment on the first 3 Gyr, when most of the star formation happens, followed by a very slow enrichment at recent times. The large scatter at $t < 3$ Gyr is probably due to the fact that stars were formed on separate smaller objects that merged later on to form the final object. The MDFs found for this object in both simulations (lower panel of Figure 3.11) are also very similar and with a shape that closely resembles that observed for some giant ellipticals (e.g., Harris et al., 2007). In addition, the central oxygen abundance (not shown in Figure 3.11) of this ELO has a value ([O/H]$\sim +0.2$) that agrees with that expected from the mass-metallicity relation

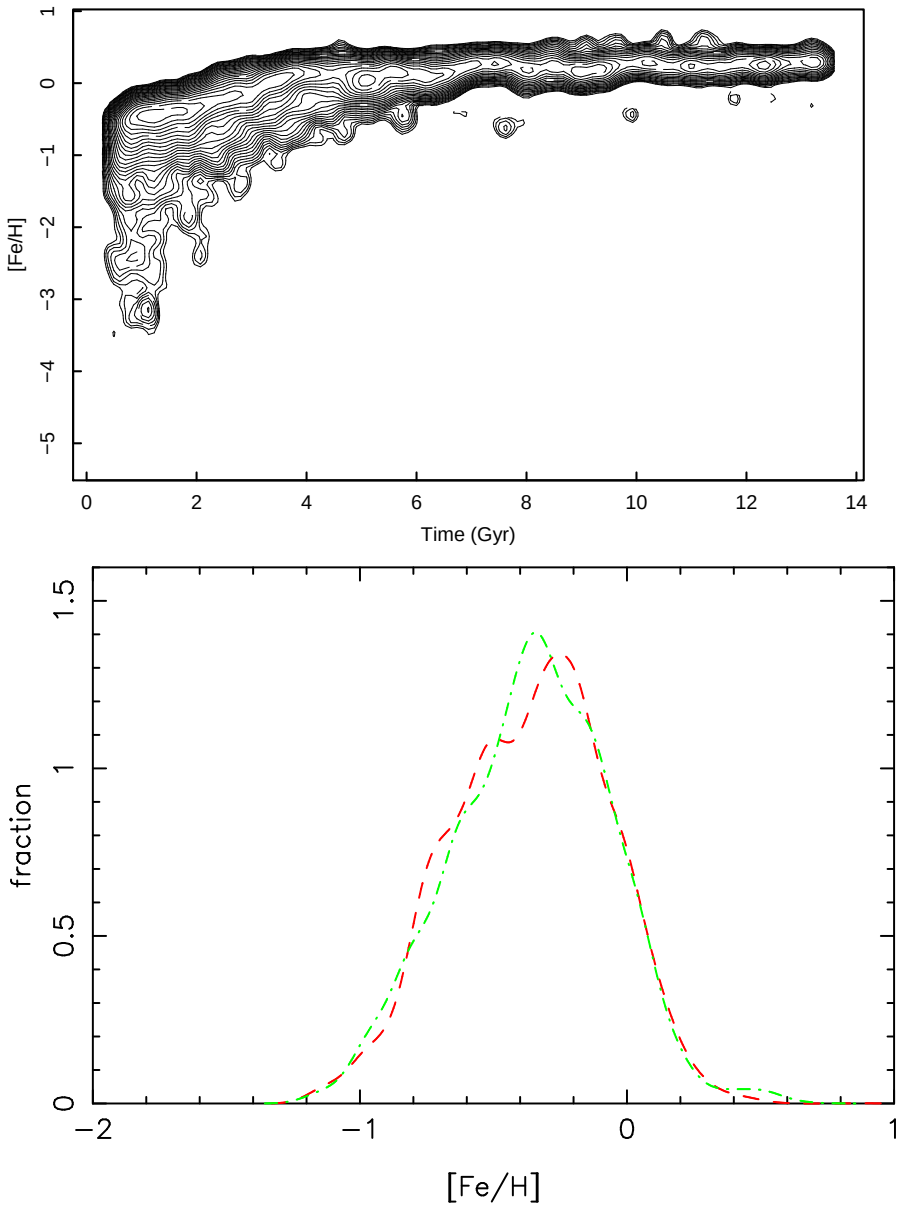

Figure 3.11: Chemical distribution for the most massive ELO in our simulation. The upper panel shows the age-metallicity relation as a contour plot. Only the ζ-cooling run is displayed since there are virtually no differences between the relations arising from both cooling methods. The lower panel shows the stellar metallicity distribution function (number fraction of stars with a given metallicity) obtained in the ζ-cooling (dashed line) and $Z_{\rm tot}$-cooling runs (dashed-dotted line) for RGB stars in the halo (see Harris et al. 2007 for an observational counterpart).

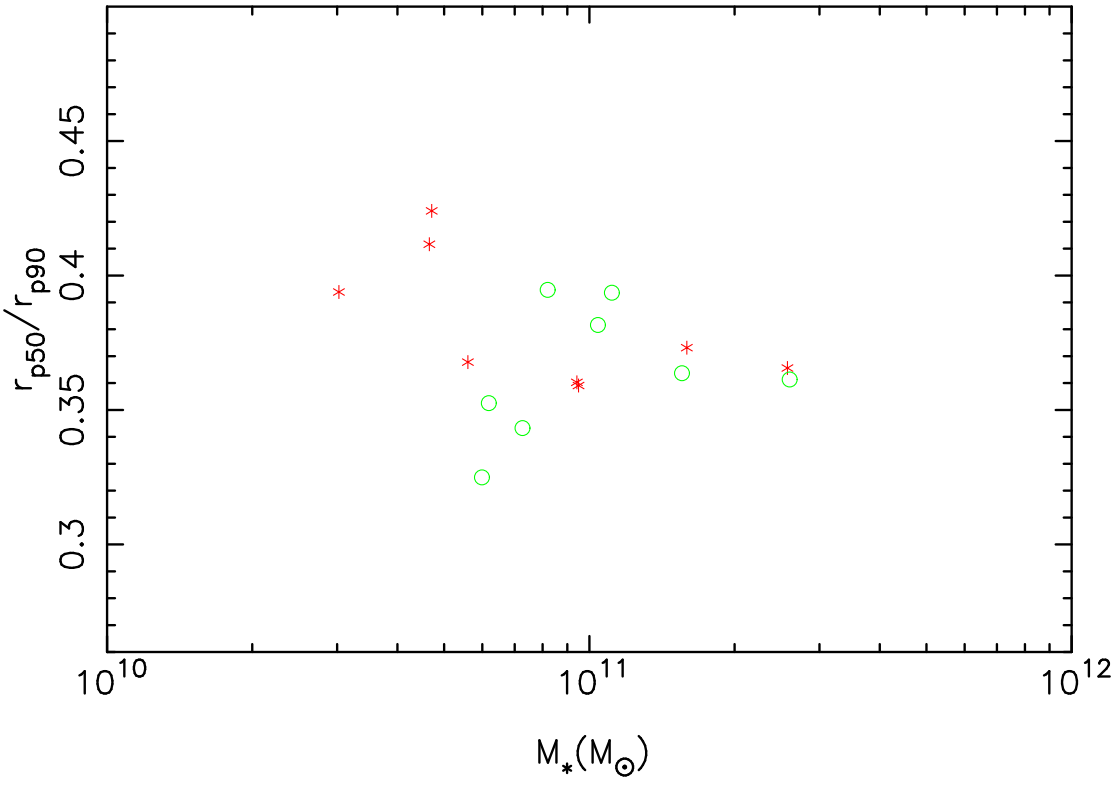

Figure 3.12: Inverse concentration index $C^{-1} = r_{p50}/r_{p90}$ as a function of total stellar mass of the ELOs found in the $Z_{\rm tot}$-cooling (circles) and ζ-cooling (stars) runs.

given by the eq. (3) of Thomas et al. (2005)

In less massive ELOs, some significant differences appear between the results obtained from the ζ and $Z_{\rm tot}$ cooling runs. Figure 3.12 shows the inverse concentration index $C^{-1} = r_{p50}/r_{p90}$ (i.e., the ratio of the half-mass Petrosian radius to the 90% mass Petrosian radius). It can be seen from this figure that the $Z_{\rm tot}$-cooling method produces objects that are more concentrated and with a higher stellar content than those found in the ζ-cooling run. Such differences are small for the most massive objects but become important as we consider less massive ELOs. They are probably due to the fact that the $Z_{\rm tot}$ method has some tendency to overestimate the cooling rate of particles not having solar abundance ratios (see Figure 3.2).

The effects of using the Q_{ij} formalism in cosmological simulations are shown in Figure 3.13. Such a figure displays, for the most massive ELO, the time evolution of the

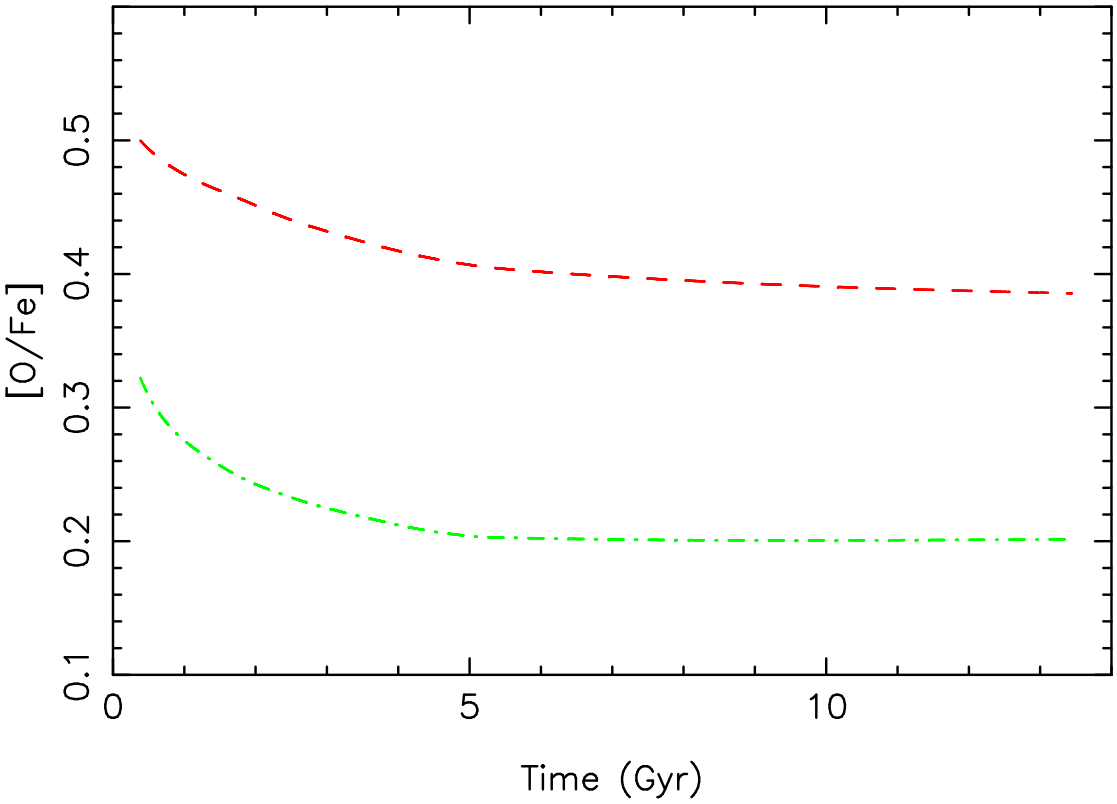

Figure 3.13: Time evolution of the stellar [O/Fe] ratio in the most massive ELO. The dashed line corresponds to the result obtained from the Q_{ij} formalism, whereas the dotted-dashed line displays the result obtained in the no-Q_{ij} run. In both cases, the ζ-cooling method was used.

[O/Fe] ratio of stellar particles with radial distances $r < 15$ kpc. The dotted-dashed line corresponds to the result obtained from the no-Q_{ij} run, whereas the dashed line displays the result obtained when using the Q_{ij} formalism and the same cooling method as in the no-Q_{ij} run (i.e., the ζ-cooling run discussed above). We see from this figure that, just like in the multi-zone test of § 3.4.1, the assumption of solar proportions leads to a significant underestimation of the [O/Fe] ratio.

3.5 Summary and Conclusions

In this paper we have introduced an SPH model for chemical enrichment and radiative cooling in cosmological simulations of structure formation. Particular attention has been

paid to including, by means of fast algorithms, the full dependence of both processes on the detailed chemical composition of star and gas particles.

As compared with previous implementations in N-body simulations codes, the main features of our SPH-model for chemical evolution and cooling are:

i) Our model takes into account the delayed gas restitution from stars by means of a probabilistic approach that shares many aspects with that proposed by LPC02, except that the stellar yields are progressively distributed through the neighbouring gas (Eq. 3.10). The tests described in § 3.4.1 and 3.4.1 show that our scheme, as well as that of LPC02 (based on Eq. 3.9), provides a fair representation of the chemical production of an SSP and reproduces the expected trends for both one-zone and multi-zone models of galaxies. Nevertheless, a scheme based on our Eq. (3.10) reduces the statistical noise and, at low particle numbers, degrades sensibly better than one based on Eq. (3.9), which becomes noise-dominated due to the lack of enough sampling data.

ii) The full dependence of the metal production on the detailed chemical composition of stellar particles is taken into account by means of the Q_{ij} formalism (Talbot & Arnett, 1973), that relates each nucleosynthetic product to its sources. Therefore, the assumption of solar proportions is relaxed in our model. Although the Q_{ij} formalism has been previously considered in chemical evolution models (e.g., Ferrini et al., 1992; Gavilán et al., 2005), this is the first time that it is used in N-body simulation codes. Releasing the assumption of solar proportions is important to accurately follow the evolution of abundance ratios like, e.g., the enhanced [α/Fe] ratio observed in elliptical galaxies and in spiral galaxy bulges. This ratio, as well as its dependence on the central velocity dispersion, could provide us with important constraints on galaxy formation models. Indeed, the tests performed in this paper for both multi-zone models (§ 3.4.1) and cosmological simulations (§ 3.4.2) suggest that the assumption of solar proportions leads to a significant underestimation of the [α/Fe] ratio in simulated galaxy-like objects.

iii) In the same way, the full dependence of radiative cooling on the detailed chemical composition of gas particles has been implemented through a fast algorithm based on a metallicity parameter, $\zeta(T)$, that takes into account the weight of the different elements on the total cooling function. We have compared the results obtained when such a composition-dependent cooling is used (referred as ζ-cooling runs) and those found from the total metallicity cooling tables of SD93 (referred as $Z_{\rm tot}$-cooling runs). To that end, we have carried out (§ 3.4.2) different simulations of galaxy formation in the framework of a concordance cosmological model. For the most massive elliptical-like objects (ELOs), we have found that the differences between the ζ and $Z_{\rm tot}$-cooling runs were

small. Such massive ELOs are characterised by strong and short bursty star formation events at early times, where most gas is exhausted and, therefore, where dynamics soon becomes dissipationless. However, for less massive ELOs, some important differences appear between the results obtained from the ζ and $Z_{\rm tot}$-cooling runs. Probably due to the fact that the $Z_{\rm tot}$ method has some tendency to overestimate the cooling rate of particles not having solar abundance ratios, such a method produces ELOs that are more concentrated and with a higher stellar content than those obtained in the ζ-cooling run. Such differences become larger as we consider ELOs with smaller stellar masses.

The above scheme for chemical enrichment and cooling has been implemented in the parallel-OpenMP version of DEVA (Serna et al., 2003), a Lagrangian code particularly designed to study galaxy assembly in a cosmological context. In this code, gravity is computed through an AP3M-like method, while hydrodynamics is computed through an SPH technique with algorithms and correction terms ensuring an accurate implementation of conservation laws (energy, entropy and angular momentum). The DEVA code has already been able to produce both elliptical (Domínguez-Tenreiro et al., 2004, 2006; Oñorbe et al., 2005, 2006, 2007) and spiral (Sáiz et al., 2002) galaxy-like objects with realistic structural, kinematic and dynamical properties. Using this model for chemical evolution and cooling, we will analyse in forthcoming papers some important chemical properties like, e.g., the metallicity distribution functions (MDF) and abundance gradients within individual objects of different morphologies and environments, as well as the fundamental metallicity relations (mass-metallicity and mass-[α/Fe] ratio) for large samples of ELOs obtained in cosmological simulations.

Appendix A: Analytical MDF for a closed box model without instantaneous recycling

Following Pagel (1997), we consider a closed box filled with primordial gas. We assume a Chabrier (2003a) IMF, $\Phi(M)$, and the star-forming law $\Psi(t)$ given by Eq. (3.25). We denote the gas and star fractions by $g(t)$ and $s(t)$, respectively. The mass conservation then implies that

$$g(t) + s(t) = 1 \ , \tag{3.35}$$

and therefore

$$\frac{{\rm d}s}{{\rm d}t} = -\frac{{\rm d}g}{{\rm d}t} = \Psi(t) - e(t) \ , \tag{3.36}$$

where $e(t)$ is the ejection rate of gas:

$$e(t) = \int_{M_\tau(t)}^{M_u} (M - M_r(M))\Psi(t - \tau(M))\frac{\Phi(M)}{M}\mathrm{d}M \ . \tag{3.37}$$

Here $\tau(M)$ and $M_\tau(t)$ represent the lifetime of a star of mass M and its inverse, respectively.

Finding the MDF is equivalent to expressing the star formation rate as a function of the metallicity. We must then obtain the time dependence of the gas composition, $Z(t)$, and invert such a function to find $t(Z)$. By substituting the latter function into the star formation rate $\Psi(t)$, we will have $\Psi(Z)$.

To find $Z(t)$, we notice that the time derivative of the total content of metals $g(t)Z(t)$ must be equal to the total ejections by dying stars $e_Z(t)$ minus the mass of metals that gets trapped in newly formed stars $\Psi(t)Z(t)$:

$$\frac{\mathrm{d}(Zg)}{\mathrm{d}t} = e_Z(t) - \Psi(t)Z(t) \ . \tag{3.38}$$

Using Eq. 3.36 we can simplify this expression:

$$g(t)\frac{\mathrm{d}Z}{\mathrm{d}t} = e_Z(t) - e(t)Z(t) \ . \tag{3.39}$$

The expression for $e_Z(t)$ is similar to that of $e(t)$:

$$\begin{aligned} e_Z(t) \quad = \quad & \int_{M_\tau(t)}^{M_u} \{[M - M_r(M)]\, Z(t - \tau(M)) + M\, q_Z(M)\} \\ & \Psi(t - \tau(M))\frac{\Phi(M)}{M}\mathrm{d}M \ , \end{aligned} \tag{3.40}$$

where $q_Z(M)$ is in our case the oxygen yield for a star of mass M. This equation involves $Z(t)$ inside the integral, so we end up with two integro-differential coupled equations. To solve them we run an iterative procedure assuming an initial value for $Z(t)$, namely $Z(t) = 0$, obtaining an expression for $e_Z(t)$, and recomputing the value of $Z(t)$ until it converges. Since both $M_r(M)$ and $q_Z(M)$ are specified in the yield tables described in section 3.2.3 and do not have a simple analytical expression, all the procedure has to be run numerically, using interpolating functions for both functions and a suitable integrator.

Once $Z(t)$ and its inverse $t_Z(Z)$ are known, we compute the final MDF as

$$\begin{aligned} \mathrm{MDF}(\log_{10}(Z)) \quad = \quad & \Psi(t_Z(Z))\,[1 - E(t_1 - t_Z(Z))] \\ & \frac{\mathrm{d}t_Z(Z)}{\mathrm{d}Z}\frac{\mathrm{d}Z}{\mathrm{d}(\log_{10}(Z))} \ . \end{aligned} \tag{3.41}$$

This is simply the aforementioned star formation expressed as a function of metallicity $\Psi(t_Z(Z))$, with suitable variable exchange terms, and a correction term $[1 - E(t_1 - t_Z(Z))]$ similar to that already introduced in Eqs. (3.4, 3.10). This term accounts for the mass fraction of stars formed with a given metallicity that died before the final time limit t_1 (i.e. the most massive ones).

Appendix B: Cooling function tables

Table 3.1

$\log_{10}$(T)	C	O	N	Ne	Mg	Si	S	Ca	Fe	ζ_0	ζ_1
4.0	2.23e-02	4.53e-01	6.13e-02	-4.55e-02	3.30e-02	1.58e-01	-8.91e-02	1.08e-01	5.33e-01	6.66e-06	3.80e+01
4.1	1.45e-02	1.47e-03	-1.31e-02	-2.80e-03	1.21e-01	-7.55e-02	3.04e-01	-9.40e-01	3.91e-02	4.46e-07	1.57e+03
4.2	2.61e-03	-2.93e-03	-1.15e-02	4.87e-05	8.46e-02	-6.21e-02	2.33e-01	-9.66e-01	8.49e-03	1.98e-08	8.69e+03
4.3	1.87e-02	7.87e-03	-4.55e-03	-5.84e-03	4.49e-02	-6.73e-02	2.68e-01	-9.58e-01	1.43e-02	3.64e-07	1.51e+03
4.4	2.12e-01	8.39e-02	6.78e-02	-3.14e-02	-1.87e-01	1.39e-01	2.16e-01	-9.13e-01	7.61e-02	4.28e-06	1.70e+02
4.5	9.08e-02	3.65e-02	4.01e-02	-1.34e-02	-1.59e-01	1.34e-01	-2.36e-01	9.41e-01	2.35e-02	1.83e-06	4.46e+02
4.6	6.87e-02	3.10e-02	3.59e-02	-1.06e-02	-1.37e-01	1.12e-01	-2.35e-01	9.51e-01	1.87e-02	1.42e-06	5.50e+02
4.7	4.13e-02	2.45e-02	2.91e-02	-8.16e-03	-1.12e-01	9.77e-02	-2.40e-01	9.57e-01	1.16e-02	9.30e-07	7.58e+02
4.8	3.47e-02	2.48e-02	3.32e-02	-6.86e-03	-1.02e-01	8.68e-02	-2.30e-01	9.61e-01	1.18e-02	8.51e-07	7.50e+02
4.9	3.33e-02	2.58e-02	3.81e-02	-6.08e-03	-1.09e-01	7.53e-02	-2.34e-01	9.60e-01	1.13e-02	8.32e-07	7.54e+02
5.0	2.40e-02	2.41e-02	3.52e-02	-4.16e-03	-1.03e-01	6.41e-02	-2.25e-01	9.65e-01	9.18e-03	6.67e-07	8.37e+02
5.1	5.90e-03	2.59e-02	3.44e-02	-3.44e-03	-1.13e-01	5.59e-02	-2.12e-01	9.68e-01	7.72e-03	4.11e-07	8.65e+02
5.2	4.36e-04	3.16e-02	3.60e-02	-1.79e-03	-1.22e-01	6.08e-02	-2.21e-01	9.64e-01	8.87e-03	3.79e-07	6.90e+02
5.3	-2.21e-03	3.71e-02	2.40e-02	3.62e-03	-1.09e-01	7.86e-02	-2.56e-01	9.54e-01	7.16e-03	3.26e-07	5.36e+02
5.4	-2.14e-03	3.84e-02	1.34e-02	9.12e-03	-9.65e-02	8.33e-02	-2.71e-01	9.52e-01	7.75e-03	3.10e-07	4.83e+02
5.5	-1.21e-03	2.47e-02	9.45e-03	2.16e-02	-7.99e-02	8.94e-02	-2.72e-01	9.53e-01	4.32e-03	2.37e-07	6.21e+02
5.6	-9.93e-04	1.07e-02	6.16e-03	2.91e-02	-6.56e-02	7.52e-02	-2.40e-01	9.65e-01	2.31e-03	1.55e-07	9.87e+02
5.7	-6.68e-04	7.54e-03	5.72e-03	4.18e-02	-5.83e-02	7.71e-02	-2.35e-01	9.66e-01	3.69e-03	1.72e-07	8.87e+02
5.8	-1.05e-03	7.79e-03	8.13e-03	4.74e-02	-5.31e-02	8.66e-02	-2.37e-01	9.65e-01	1.11e-02	2.45e-07	7.64e+02
5.9	-1.64e-03	1.02e-02	7.11e-03	2.46e-02	-1.56e-02	1.35e-01	-2.57e-01	9.54e-01	4.40e-02	5.10e-07	7.61e+02
6.0	3.08e-03	9.11e-03	9.36e-03	1.30e-02	6.56e-02	2.62e-01	-2.68e-01	8.75e-01	1.55e-01	1.47e-06	5.16e+02
6.1	3.64e-03	8.29e-03	1.24e-02	8.67e-04	-2.71e-02	2.08e-01	-1.76e-01	8.88e-01	1.65e-01	1.49e-06	7.27e+02
6.2	3.72e-03	1.08e-02	1.56e-02	4.35e-04	-4.39e-02	2.79e-01	-1.04e-01	7.83e-01	2.83e-01	2.41e-06	4.88e+02
6.3	3.51e-03	1.02e-02	1.17e-02	-1.11e-03	-4.37e-02	2.33e-01	-1.44e-01	9.00e-01	1.57e-01	1.49e-06	6.54e+02
6.4	1.88e-03	1.52e-02	8.75e-03	-9.09e-04	-8.42e-02	1.96e-01	-1.29e-01	9.47e-01	1.04e-01	1.09e-06	6.76e+02

Continued on next page

Table 3.1 – continued from previous page

$\log_{10}$(T)	C	O	N	Ne	Mg	Si	S	Ca	Fe	ζ_0	ζ_1
6.5	1.13e-03	1.81e-02	1.31e-02	1.10e-02	-6.55e-02	2.18e-01	-1.28e-01	9.03e-01	1.87e-01	1.70e-06	4.63e+02
6.6	1.34e-03	1.21e-02	8.44e-03	1.32e-02	-4.33e-02	1.22e-01	-1.35e-01	9.53e-01	1.74e-01	1.45e-06	6.46e+02
6.7	2.60e-03	1.27e-02	1.27e-02	2.20e-02	-2.92e-02	1.40e-01	-1.52e-01	9.07e-01	2.53e-01	2.03e-06	5.04e+02
6.8	4.29e-03	1.65e-02	2.09e-02	2.78e-02	-4.33e-03	1.83e-01	-1.48e-01	7.94e-01	3.95e-01	3.10e-06	3.56e+02
6.9	3.97e-03	1.52e-02	2.42e-02	2.66e-02	2.76e-02	1.94e-01	-9.23e-02	6.20e-01	5.66e-01	4.27e-06	3.09e+02
7.0	1.18e-02	1.27e-02	2.76e-02	2.47e-02	6.48e-02	1.71e-01	4.97e-02	2.48e-03	7.01e-01	5.26e-06	2.84e+02
7.1	1.06e-02	1.85e-02	2.92e-02	2.22e-02	1.49e-02	1.85e-01	-3.01e-04	3.97e-01	6.81e-01	5.16e-06	2.74e+02
7.2	7.80e-03	2.34e-02	2.80e-02	1.88e-02	-1.84e-02	1.73e-01	-4.31e-02	6.52e-01	5.47e-01	4.24e-06	2.92e+02
7.3	7.61e-03	2.15e-02	1.98e-02	2.02e-02	-6.51e-03	1.42e-01	-4.50e-02	7.87e-01	4.14e-01	3.29e-06	3.30e+02
7.4	9.91e-03	2.80e-02	1.80e-02	2.13e-02	-3.79e-02	1.37e-01	-5.00e-02	8.14e-01	4.01e-01	3.26e-06	3.04e+02
7.5	1.37e-02	3.87e-02	1.52e-02	3.14e-02	-3.30e-02	1.76e-01	-4.85e-02	7.47e-01	5.04e-01	4.11e-06	2.24e+02
7.6	1.13e-02	3.94e-02	1.08e-02	2.86e-02	-6.82e-02	1.77e-01	-1.24e-01	8.45e-01	4.34e-01	3.56e-06	2.45e+02
7.7	1.50e-02	6.76e-02	1.28e-02	5.85e-02	-5.65e-02	2.77e-01	-5.40e-02	5.18e-01	7.45e-01	6.02e-06	1.36e+02
7.8	2.16e-02	7.98e-02	7.41e-03	7.25e-02	-2.17e-03	2.99e-01	3.78e-02	-4.54e-02	8.52e-01	6.93e-06	1.13e+02
7.9	2.00e-02	6.52e-02	4.17e-03	5.68e-02	-3.31e-02	2.70e-01	-1.34e-01	6.26e-01	6.21e-01	5.19e-06	1.45e+02
8.0	1.98e-02	6.66e-02	-1.28e-03	6.68e-02	4.44e-02	2.20e-01	1.16e-01	-5.75e-01	6.37e-01	5.26e-06	1.34e+02
8.1	1.54e-02	5.59e-02	1.15e-03	4.29e-02	-3.62e-03	9.26e-02	2.16e-01	-8.28e-01	4.37e-01	3.65e-06	1.82e+02
8.2	1.61e-02	6.35e-02	-6.72e-04	3.80e-02	-1.82e-02	3.22e-02	2.94e-01	-8.25e-01	4.34e-01	3.63e-06	1.75e+02
8.3	1.00e-02	3.93e-02	-3.32e-03	2.82e-02	4.48e-03	8.93e-03	2.60e-01	-9.18e-01	2.69e-01	2.24e-06	2.71e+02
8.4	7.80e-03	2.82e-02	-7.31e-03	2.38e-02	2.61e-02	-3.57e-03	2.47e-01	-9.46e-01	1.98e-01	1.64e-06	3.56e+02
8.5	6.08e-03	2.13e-02	-7.85e-03	2.08e-02	4.32e-02	-1.34e-02	2.41e-01	-9.56e-01	1.57e-01	1.28e-06	4.41e+02

Table 3.1: DRR $\mathbf{c} = (c_{He}, c_C, ..., c_{Fe})$ coefficients as a function of temperature

Table 3.2

$\log_{10}$(T)	ζ=0	ζ=0.01	ζ=0.02	ζ=0.03	ζ=0.04	ζ=0.1	ζ=0.2	ζ=0.4	ζ=0.6	ζ=0.8	ζ=1
4.0	21.22	21.50	21.66	21.78	21.88	22.21	22.48	22.75	22.90	22.99	23.07
4.1	23.80	23.80	23.80	23.81	23.81	23.84	23.88	23.95	24.00	24.04	24.08
4.2	25.21	25.21	25.21	25.21	25.21	25.22	25.23	25.25	25.26	25.28	25.29
4.3	25.30	25.30	25.31	25.31	25.32	25.35	25.39	25.45	25.50	25.54	25.57
4.4	25.09	25.11	25.13	25.14	25.16	25.24	25.35	25.50	25.60	25.67	25.72
4.5	24.93	24.98	25.03	25.07	25.10	25.27	25.46	25.67	25.81	25.90	25.97
4.6	24.77	24.89	24.98	25.06	25.12	25.38	25.62	25.88	26.03	26.13	26.21
4.7	24.70	24.90	25.04	25.14	25.23	25.54	25.80	26.07	26.22	26.33	26.41
4.8	24.97	25.13	25.25	25.35	25.43	25.72	25.98	26.24	26.40	26.50	26.58
4.9	25.24	25.37	25.47	25.55	25.62	25.89	26.13	26.39	26.55	26.65	26.73
5.0	25.16	25.35	25.48	25.59	25.67	25.98	26.24	26.51	26.67	26.78	26.86
5.1	24.94	25.27	25.46	25.59	25.69	26.04	26.32	26.60	26.76	26.87	26.96
5.2	24.71	25.25	25.48	25.63	25.75	26.12	26.41	26.69	26.86	26.97	27.06
5.3	24.52	25.25	25.51	25.67	25.79	26.18	26.47	26.75	26.92	27.03	27.12
5.4	24.27	25.21	25.49	25.66	25.78	26.17	26.46	26.75	26.91	27.02	27.11
5.5	24.27	24.97	25.22	25.38	25.50	25.88	26.17	26.46	26.62	26.74	26.83
5.6	24.20	24.77	25.01	25.16	25.27	25.65	25.94	26.22	26.39	26.50	26.59
5.7	24.14	24.72	24.97	25.12	25.24	25.62	25.91	26.19	26.36	26.47	26.56
5.8	24.09	24.64	24.88	25.03	25.15	25.52	25.81	26.10	26.26	26.38	26.47
5.9	24.12	24.43	24.61	24.74	24.84	25.18	25.46	25.74	25.90	26.02	26.11
6.0	24.12	24.34	24.48	24.59	24.68	24.99	25.26	25.54	25.70	25.82	25.90
6.1	24.12	24.30	24.43	24.53	24.61	24.92	25.18	25.45	25.62	25.73	25.82
6.2	24.12	24.30	24.42	24.52	24.60	24.90	25.16	25.44	25.60	25.71	25.80
6.3	24.12	24.27	24.38	24.46	24.54	24.82	25.07	25.34	25.50	25.62	25.70
6.4	24.13	24.22	24.30	24.36	24.42	24.66	24.89	25.15	25.30	25.41	25.50

Continued on next page

Table 3.2 – continued from previous page

$\log_{10}$(T)	ζ=0	ζ=0.01	ζ=0.02	ζ=0.03	ζ=0.04	ζ=0.1	ζ=0.2	ζ=0.4	ζ=0.6	ζ=0.8	ζ=1
6.5	24.15	24.21	24.26	24.31	24.35	24.54	24.74	24.97	25.12	25.23	25.30
6.6	24.17	24.22	24.25	24.29	24.32	24.48	24.66	24.88	25.02	25.12	25.20
6.7	24.20	24.23	24.26	24.29	24.32	24.45	24.60	24.80	24.94	25.03	25.11
6.8	24.23	24.26	24.28	24.30	24.32	24.43	24.56	24.75	24.87	24.96	25.03
6.9	24.27	24.29	24.31	24.33	24.34	24.44	24.56	24.73	24.84	24.93	25.00
7.0	24.30	24.32	24.34	24.35	24.37	24.45	24.57	24.72	24.84	24.92	24.99
7.1	24.34	24.35	24.37	24.38	24.39	24.46	24.55	24.69	24.80	24.88	24.94
7.2	24.38	24.39	24.40	24.41	24.42	24.47	24.54	24.66	24.75	24.82	24.87
7.3	24.42	24.42	24.43	24.44	24.45	24.49	24.54	24.64	24.71	24.78	24.83
7.4	24.46	24.46	24.47	24.48	24.48	24.51	24.56	24.64	24.71	24.76	24.81
7.5	24.50	24.51	24.51	24.52	24.52	24.55	24.59	24.66	24.71	24.76	24.80
7.6	24.54	24.55	24.55	24.56	24.56	24.58	24.62	24.68	24.73	24.77	24.81
7.7	24.59	24.59	24.60	24.60	24.60	24.62	24.65	24.71	24.76	24.79	24.83
7.8	24.63	24.64	24.64	24.64	24.65	24.66	24.69	24.74	24.78	24.82	24.86
7.9	24.68	24.68	24.68	24.69	24.69	24.71	24.73	24.78	24.82	24.85	24.88
8.0	24.72	24.73	24.73	24.73	24.74	24.75	24.77	24.82	24.85	24.88	24.91
8.1	24.77	24.77	24.78	24.78	24.78	24.79	24.82	24.85	24.89	24.92	24.95
8.2	24.82	24.82	24.82	24.82	24.83	24.84	24.86	24.90	24.93	24.96	24.98
8.3	24.87	24.87	24.87	24.87	24.87	24.89	24.90	24.94	24.97	24.99	25.02
8.4	24.91	24.92	24.92	24.92	24.92	24.93	24.95	24.98	25.01	25.03	25.06
8.5	24.96	24.96	24.96	24.97	24.97	24.98	25.00	25.03	25.05	25.08	25.10

Table 3.2: Cooling function $\log_{10}(\Lambda_N)$ as a function of temperature T and the metallicity parameter ζ

Chapter 4

Disk galaxies with broken luminosity profiles from cosmological simulations[1]

> The nice thing about quotes is that there are so many to choose from!
>
> ANONYMOUS

4.1 Introduction

There is a growing body of observations that show that the classical picture of spiral galaxies with a purely exponential disk does not match most galaxies found in the local (Pohlen et al., 2002; Pohlen & Trujillo, 2006; Pohlen et al., 2007; van der Kruit, 2007; Bakos et al., 2008) or distant universe (Pérez, 2004; Trujillo & Pohlen, 2005; Azzollini et al., 2008b). Indeed, galactic disks with a single exponential surface brightness profile (Type-I, in the classification of Freeman, 1970) are relatively rare ($\lesssim 15\%$). Most profiles are better fitted by two exponentials separated at a well-defined break radius, with the outer exponential being either downbending (Type-II, the majority) or upbending (Type-III, first discovered by Erwin et al., 2005). The profiles with an upbending break could be explained (Pohlen & Trujillo, 2006, PT06 hereafter) either from a disturbed morphology due to interactions with neighboring galaxies or, in some cases, by the presence of an $R^{1/4}$ bulge component that rises over the exponential disk in the outer region. The origin of Type-II profiles, more frequent in late-type galaxies, is instead much more poorly understood.

[1] This work is published as Martínez-Serrano, F. J., Serna, A., Doménech-Moral, M., & Domínguez-Tenreiro, R. 2009, ApJ, 705, L133, arXiv:0906.1118.

Several authors have investigated how galaxy disks develop a downbending break, mainly through non-cosmological N-body simulations of isolated objects (Debattista et al., 2006; Bournaud et al., 2007; Roškar et al., 2008a,b; Foyle et al., 2008), but also from cosmological simulations (Abadi et al., 2003; Governato et al., 2007). All these works agree in explaining the observed break in the surface brightness profile as the result of an intrinsic break in the mass profile for the stellar component. In the most widely considered scenario, the break in the stellar mass profile develops as a consequence of a cutoff in the star formation (Elmegreen & Parravano, 1994). In such a scenario, the outer exponential disk would be formed by stars that migrate from the inner disk toward the regions beyond the star formation cutoff, prompted by secular instabilities such as spiral arms (Roškar et al., 2008a,b) or clump disruptions (Bournaud et al., 2007). An alternative model has been suggested by Foyle et al. (2008) after simulations starting from an already formed single exponential disk. In their simulations, the inner disk forms when the bulge draws mass from the inner regions, thus making the inner disk profile shallower while the outer region stays almost unaltered and fixed by the initial conditions.

All the above models fail however to match recent observational evidence provided by Bakos et al. (2008)[2]. These latter authors have analyzed a sample of late-spirals and found that galaxies with a Type-II surface brightness profile generally have a "U-shaped" color profile with its minimum nearly located at the luminosity break radius. When this color profile was taken into account to calculate the stellar surface mass density, they obtained almost purely exponential mass profiles. Consequently, the observed luminosity break in Type-II galaxies does not seem to be necessarily related to an intrinsic break in the stellar mass profile. A downbending of the luminosity profile could also be caused by differences between the stellar populations of the inner and outer disks, even with no breaks in the mass profile at all. However, stellar counts of red giant branch stars in the outskirts of M33 (Ferguson et al., 2007) or NGC 4244 (de Jong et al., 2007) indicate that this may not always be the case.

The aim of this Chapter is to study whether numerical simulations can naturally predict the above-observed features: downbending broken luminosity profiles in galactic disks with a purely exponential mass distribution. We will use cosmological simulations where galaxies form after the collapse of primordial instabilities and where their final

[2]A work by Sánchez-Blázquez et al. (2009) appeared about the time this work was submitted showing that, in agreement with our work, broken luminosity profiles can appear in simulated galaxies with exponential mass profiles.

structure arises from a hierarchical sequence of mass aggregation and from the interaction with their environments.

4.2 The simulations

The N-Body + Smoothed Particle Hydrodynamics (SPH) simulations have been performed using an OpenMP parallel version of DEVA code (Serna et al., 2003) and the methods for star formation, chemical feedback, and abundance-dependent cooling described in Martínez-Serrano et al. (2008). In this code, particular attention has been paid that the conservation laws hold as accurately as possible. Star formation is implemented through a Kennincutt–Schmidt-like law with a density threshold of $\rho_{\rm thres} = 6.75 \times 10^{-26}$ g cm^{-3} and a star formation efficiency of $c_* = 0.1$ that implicitly account for energy feedback[3]. Each simulation is a cosmological *zoom-in* that includes high-resolution gas and dark matter for the flow converging region that generates the main object. The rest of the simulation box is sampled by low-resolution dark matter particles that account for tidal forces over the flow converging region. As a first step we consider a concordance cosmological model and generate three high-resolution initial conditions in a box of 10 Mpc per side.[4] After degrading these conditions, we perform the corresponding full box simulations at lower resolution. In each of these three simulations, we selected one object (the most massive one with a prominent gas disk at $z = 0$ not clearly disrupted from a very recent major merger) and traced back the particles inside its virial radius until the initial redshift $z_{\rm init}$. We then computed the convex hull (Barber et al., 1996) enclosing these particles at $z_{\rm init}$ and substituted all the particles inside the convex hull by their high-resolution counterparts. Gas particles outside the hull are eliminated and their masses added to the low-resolution dark matter component, thus obtaining the initial conditions for each simulation. The galaxies obtained in this way have a full history of mergers and accretion in a cosmological context, without any assumptions made for their initial conditions beyond the cosmology and the initial conditions generator used (Prunet et al., 2008). The mass resolution for baryonic particles used in each simulation is specified in Table 4.1.

[3] We use this simple model for subresolution physics because our aim in this work is to test the minimal conditions for the formation of realistic disks.

[4] Although this box side implies a lack of very massive objects and environments, it has little effect on the internal properties of the haloes (Power & Knebe, 2006).

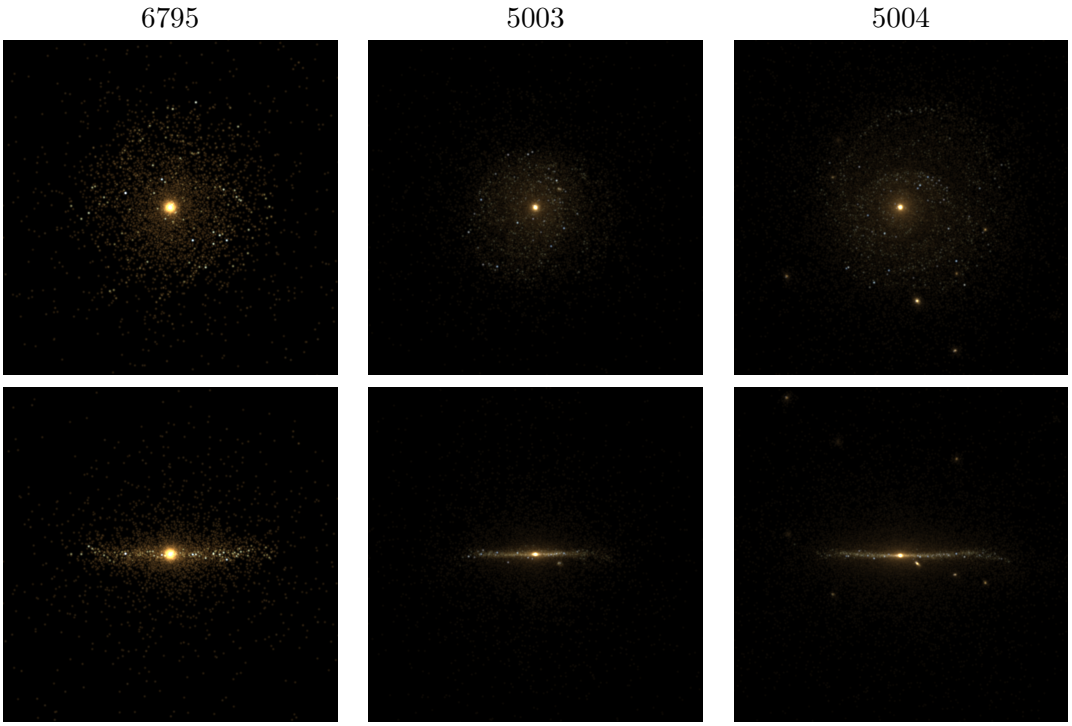

Figure 4.1: Face-on and edge-on synthetic images obtained using Bruzual & Charlot (2003) models. All images are 50 kpc side.

4.3 Disk object properties

4.3.1 Consistency with observational data

Object properties are summarized in Table 4.1, where we can see a remarkable consistency with observational data (Fig. 4.1 displays their face-on and edge-on images). They span a range of stellar masses from 1.71 to 3.86 $\times$ 10^{10} $M_{\odot}$. Their luminosity profiles have been obtained and fitted by following the procedures described in §4.3.2 below (see also the notes of Table 1). A first remarkable feature of our simulations is that we obtain objects with bulge sizes comparable to those recently obtained by Governato et al. (2008). Indeed, two out of the three simulated objects have D/T ratios implying rather small bulges, consistent with those observed for late-type spirals (*e.g.* Balcells et al., 2007; Gadotti, 2009). This is an interesting property because, although Type-II breaks appear in all spiral types, they are more abundant in late Hubble types (PT06, Erwin et al., 2008). Note also that the disks are rather thin with vertical scales of $\sim$ 0.4 – 0.6 kpc for the thin disk and $\sim$ 1.5– 2.2 kpc for the thick disk. We also display in

Table 4.1 the I-band absolute magnitude and the gas rotation velocity of each object. They are found to be in good agreement with the observed Tully-Fisher relation (*e.g.* Giovanelli et al., 1997; Springob et al., 2007, see Fig. 6 of the latter reference). In the same way, through Sérsic fits to the total light distribution we have determined the r-band absolute Sérsic magnitude $M_{r,s}$ and the half-light radius $r_{50,s}$ (see Table 4.1). The obtained values are again in good agreement with both the luminosity-size and stellar mass-size relations for disk galaxies given by Shen et al. (2003) (see their Figs. 6 and 11, respectively).

Galaxy	m_{bar}[1]	M_{star}[2]	D/T[3]	r_e[3]	r_b[3]	$M_I - 5\log(h)$[4]	h_{z1}[5]	$M_{r,s}$[6]
	ϵ	M_{gas}[2]	r_s[3]	n[3]	r_c[3]	V_{rot}[4]	h_{z2}[5]	$r_{50,s}$[6]
	[$M_\odot$]	[$10^{10} M_\odot$]		[kpc]	[kpc]		[kpc]	
	[kpc]	[$10^9 M_\odot$]	[kpc]		[kpc]	km/s	[kpc]	[kpc]
6795	2.92×10^6	3.86	0.39	0.45	10.75	-20.75	0.50	-20.82
	0.55	9.59	4.42	0.87	18.1	203.6	1.53	2.32
5003	3.82×10^5	1.71	0.67	0.26	9.83	-20.14	0.42	-20.23
	0.40	4.15	2.92	0.91	12.1	133.2	1.99	1.22
5004	3.82×10^5	3.46	0.64	0.31	12.60	-20.78	0.59	-20.88
	0.40	7.25	3.92	2.33	20.2	162.2	2.14	2.66

Table 4.1: Analyzed objects

4.3.2 Broken face-on profile

In the first row of Figure 4.2 we plot the azimuthally averaged surface luminosity profiles in both the g and r bands for the three simulated galaxies, along with an approximate limit surface luminosity μ_{lim} beyond which Sloan Digital Sky Survey observations such

[1] Mass of a single baryonic particle (gas or star).

[2] This value was computed using the particles inside ten times the disk radius r_s for each object.

[3] r_s is the inner disk scale length or e-folding length. r_e is the effective radius of the bulge. r_b is the break radius. r_c is the cutoff radius. n is the Sérsic parameter for the bulge. The fits are for the r-band luminosity profile, obtained using the models of Bruzual & Charlot (2003).

[4] Total I-band luminosity and gas rotation speed.

[5] Vertical mass profile scaleheights for the thin and thick stellar disks. Obtained using particles with $r_e < r < r_b$.

[6] Sérsic fits to the total light distribution. Given are Sérsic's half-light radius and total r-band luminosity.

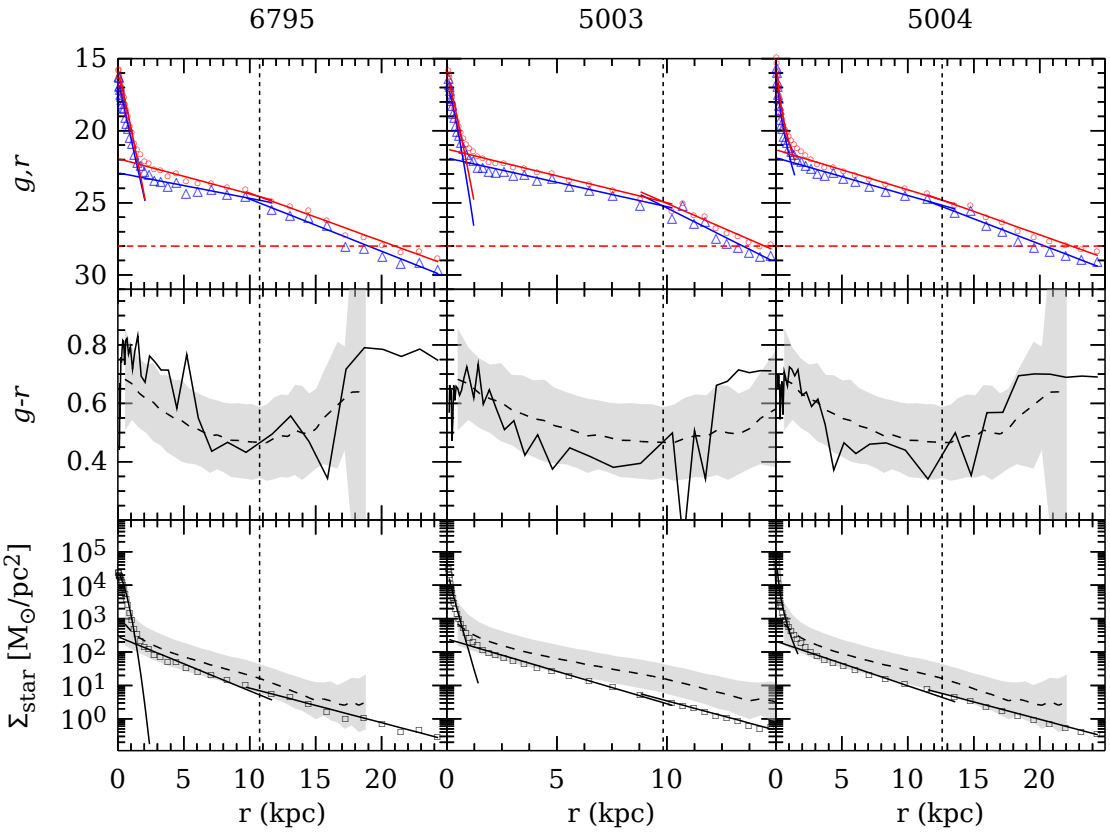

Figure 4.2: Observational properties of the galaxies presented in this letter. The top panels show the face-on luminosity profile for each galaxy in the r (circles) and g (triangles) bands, together with fits to the bulge and both disk components. Units are mag/$\Box''$. The break radius for each galaxy separating the inner and outer exponential components is shown as a dashed vertical line and an approximate critical surface brightness of $\mu_{\rm lim} = 28.0$ r-mag/$\Box''$. The middle row shows the g-r color profile (compare with Bakos et al., 2008). The bottom row shows the mass profile which unlike the luminosity profile is either exponential anti-trucated. For reference, we have overplotted the Bakos et al. (2008) data for the color and mass plots as dashed lines with the scatter of the observational data shown as a gray shaded area.

as those of PT06 become background-dominated. These profiles were obtained by computing the luminosity of each stellar particle, essentially a single stellar population (SSP) with known age and metallicity, and interpolating in the Bruzual & Charlot (2003) tables. We note that all these profiles can indeed be considered as broken exponentials. The slope in the outer disk region is in all cases steeper than in the inner disk and, hence, the three simulated objects can be classified as Type-II galaxies. We have then fitted each profile by means of a Levenberg–Marquardt algorithm based on a double exponential + bulge model. In order to reduce noise, the fits were computed by using the integrated luminosity profiles instead of the surface luminosity profiles. The resulting bulge and disk scale lengths are given in Table 4.1, as well as the break radius (defined by the intersection of the inner and outer exponentials) of each galaxy. We find that the average ratio between the break radius and the inner exponential disk scale is $r_b/r_s = 3.0 \pm 0.5$, in agreement with the value found by PT06.

We also note that the g and r profiles have different slopes, both before and after the break radius. This results in characteristic "U-shaped" $g - r$ profiles such as those depicted in the second row of Figure 4.2. These color profiles are very similar to those observed in many spiral galaxies with broken profiles (Azzollini et al., 2008a; Bakos et al., 2008). The stellar mass profiles however do not show any downbending trend. In contrast, as row 3 of Figure 4.2 shows, mass profiles can be considered as Type I (no break) in all the simulated galaxies, or even with a very slightly upbending trend (Type III). This result agrees with the findings of Bakos et al. (2008) who used the M/L ratio provided by Bell et al. (2003) to derive a mass profile from observational data. In any case, outside the luminosity break we do not find any lack of stellar mass respect to a single exponential decline.

In order to progress in understanding the nature of the above downbending luminosity profiles, we have analyzed the possible connection between the break radius and the cutoff radius for star formation. In the first row of Figure 4.3, we represent the surface gas density for each galaxy. For all of them the profile shows a plateau that extends from the center of the galaxy with a shallow slope until the break radius, marked with a dotted vertical line. Given the Schmidt–Kennicutt star formation recipe implemented in our code (Martínez-Serrano et al., 2008), the star formation rate (SFR) is expected to follow the gas density at a power 1.5 and increase toward the center. Indeed, in the second row we depict the instantaneous SFR at $z = 0$, which follows a similar trend, with a steeper slope, especially for $r > r_b$. On the same row, it is also represented the fraction of gas particles above the density threshold for star formation, and the fraction

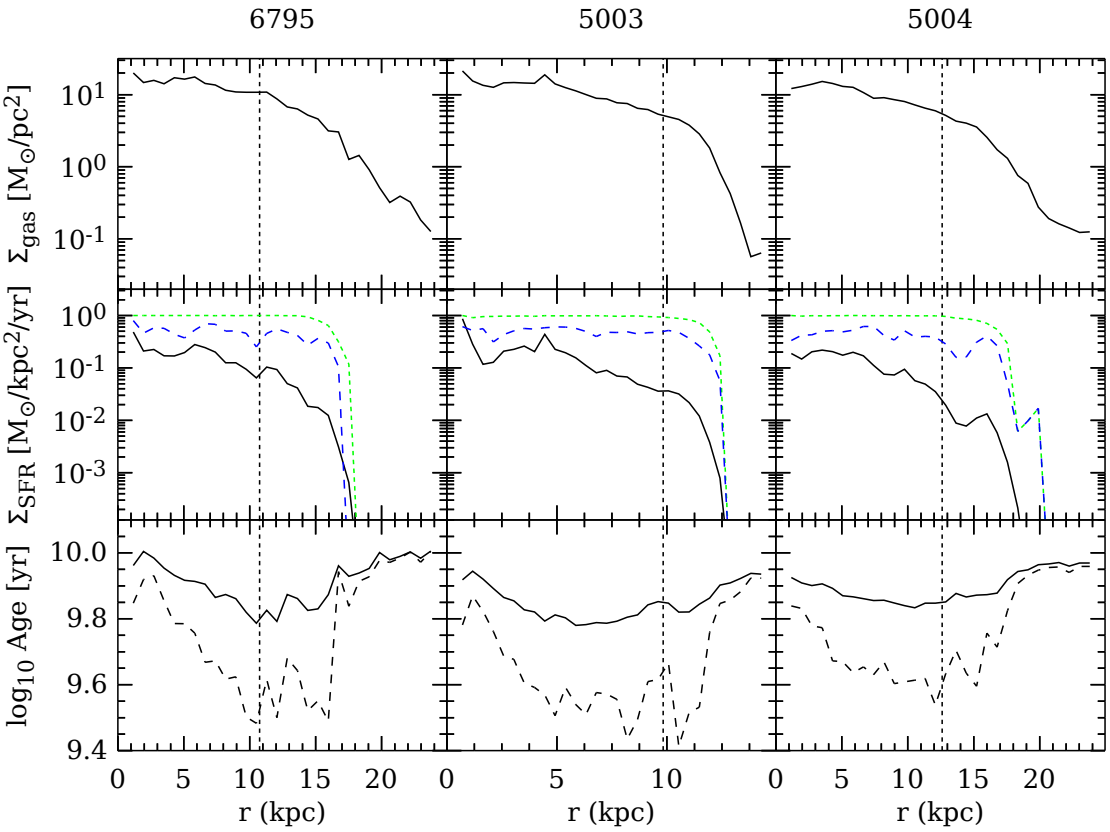

Figure 4.3: Dynamical properties of the galaxies presented in this work as a function of radius. The top panels show the gas column-density profile. As in Figure 4.2, the dashed vertical line shows the computed break radius for each galaxy in the r band. The middle row shows the instantaneous star formation rate derived from the Schmidt law implemented in the code as a continuous line, with the fraction of gas particles able to form stars according to the $\rho_{\rm thres}$ limit and both the $\rho_{\rm thres}$ and $\nabla\cdot\mathbf{v} < 0$ criterion shown as a dotted and dashed lines respectively. The bottom row shows the mean stellar age weighted by stellar mass (continuous line) and r-band luminosity (dashed line).

of gas particles eligible to form stars according to both the density criterion and the convergent flow ($\nabla \cdot \mathbf{v} < 0$) criterion. As it can be seen, the density criterion effectively imposes a cutoff radius for the star formation, while the convergent flow criterion does not impose any significant restriction on the amount of gas particles able to form stars at a given radius, appearing just as some oscillations due to the spiral arm structure of the objects that compresses and rarefies the gas. The position of the $\rho_{\rm thres}$ cutoff is always well outside the break radius, implying that our choice of $\rho_{\rm thres}$ does not directly impose the position of the luminosity break, but it rather appears well within the zone where star formation is allowed. Note also that the cutoff position coincides approximately with a surface gas density (first row of Fig. 4.3) of ~ 1 $M_\odot/pc^2$, while the density at the break is ~ 10 $M_\odot/pc^2$, coinciding with the value given by Martin & Kennicutt (2001) for the threshold of star formation.

In the works of Roškar et al. (2008b,a), a break in the mass profile appears in the same position where a significant drop in the SFR happens, with the stars beyond the break being transported there by migrations from the inner parts of the galaxy. Our galaxies instead do not show such a steep break for the SFR and consistently do not present a break on the stellar mass profile, so that the only interpretation for this fact is a difference in the stellar populations in each region. Indeed, as row 3 of Fig. 4.3 shows, there is a "U-shape" profile for the mean stellar age, very similar in shape to the color profile. The break on the profile appears to be at the minimum of the stellar age profile for galaxies 6795 and 5004, while 5003 presents a larger minimum. The coincidence between the break radius and the minimum of the age profile was already noted by Roškar et al. (2008b). Given that young stellar populations are brighter than old ones, the age decrease until the break radius makes the light profile shallower than the mass profile, while the increase after the break radius makes it steeper. This fact alone would explain the luminosity break. It also readily accounts for the color profile, since younger populations are bluer.

4.3.3 Edge-on profiles and the cutoff

Even though the outer disk profiles remain exponential until the faintest observational limit $\mu_{\rm lim}$, a final cutoff should exist in a Schmidt-Kennicutt law with a threshold gas density $\rho_{\rm thres}$ for star formation and is clearly apparent in the second row of Fig. 4.2. This cutoff is better seen in the edge on profiles, which we represent in Fig. 4.4 and give in Table 4.1. Despite their similarity with the observed profiles reported by van der Kruit (1988, 2007), the inner parts of our profiles must be regarded with caution

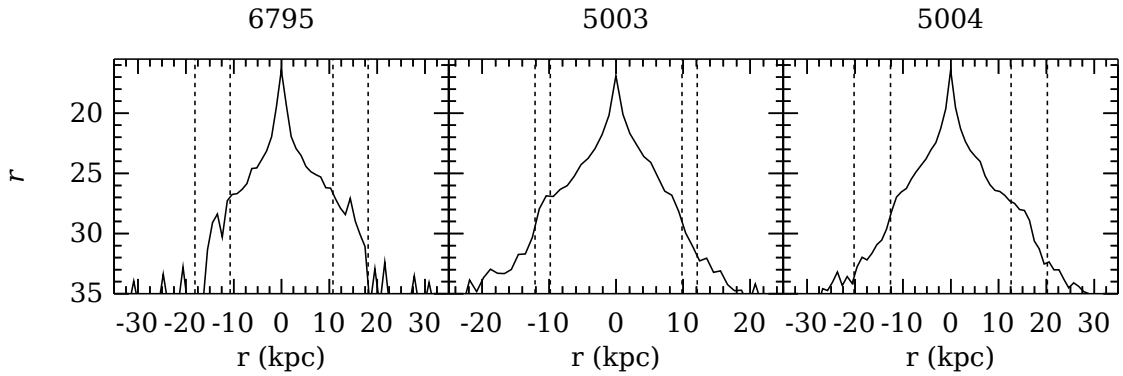

Figure 4.4: Edge-on r-band luminosity for the three objects presented in this work. The Y-axis units are mag/$\Box''$. We have selected stars to be included in this plot by imposing a cutoff of 1 kpc below and above the disk plane. No dust effects have been taken into account, so data for the inner part of the galaxy should be considered with caution. We also depict the break and cutoff radii as vertical lines.

because in edge-on profiles dust extinction is important, while the stellar population synthesis model we use in this work does not include dust effects. Nevertheless, these profiles allow us to analyze the existence of a final cutoff in the outer part of the disk, where gas density is already low. While the face-on profiles of Fig. 4.1 showed no signs of a cutoff radius, the edge-on profiles do show signs of such cutoff. We find that the ratio of the cutoff radius to the inner disk scale has a value of $r_c/r_s = 4.3 \pm 0.4$, in rough agreement with the values found by van der Kruit (1988) for the cutoff radius of classical truncations in edge-on galaxies. Our data are thus consistent with both views: face-on profiles show a change of slope in the exponential profile at the break radius and then extend up to the faintest limit, while edge-on profiles present a steeper downwards trend up to a final cutoff that approximately coincides with the $\rho_{\rm thres}$ imposed cutoff for the star formation. While this was expected on a purely geometrical basis, it is noteworthy that we recover for a cosmological simulation the results of Pohlen et al. (2007).

4.4 Origin of the stars in the outer disk and discussion

Our interpretation of the appearance of a break in the luminosity profile is related with the interplay between the slope of the stellar mass profile, exponential without any significant change, and that of the gas profile, which is shallower in the inner part and

drops rather abruptly beyond the break radius. The shallow inner profile of the gas can be attributed to angular momentum transfer from the inner particles toward the outer parts, possibly due to spiral arm instabilities (Kaufmann et al., 2007) or viscosity effects. The steeper profile of the inner stellar disk is likely due to the inside-out grow mode of our disks: the smaller the radius the longer star formation has been going on there. Going from the center toward the break radius, the ratio of gas mass to stellar mass, and consequently, the ratio of SFR to stellar mass increases. This explains the coincidence of the break radius with the minimum of mean stellar age. Once we reach the break radius, there is a change in the slope of the gas density profile that can be interpreted as an ending of the gas disk. This is likely to be due to cosmological effects such as inflow of gas with angular momentum not aligned with the disk rotation.

Independently of the mechanism that leads to a cutoff of the gaseous disk at large radii, there is a transition zone between the break and the cutoff radius where star formation is still possible, but the slope of the SFR is steeper than that of the stellar disk. There must be a mechanism that brings stars to this area, since star formation alone cannot account for all the stars present there. We have analysed the origin of the stars present in the outer disk ($r > r_b$) at $z = 0$ by tracing them back in time. We divide the volume of each simulation into three regions at $z = 0.9$. We assume a disk height of 2 kpc and define the inner disk as a cylinder with $r < r_b$ and the outer disk as a volume with $r_b < r < r_c$. The rest of the volume is considered to be external. In the top-right panel of Figure 4.5 we show the fraction of the outer disk stars that belong to each of these volumes, separated also into gas and stars (likely old and moderately old stars at $z = 0$, respectively). As it can be seen, most stars (64%–78%) in the outer disk were residing in the inner disk at $z = 0.9$, either as gas (the majority), or stars. This indicates that stellar migrations play a relevant role in the build up of the outer disk, as Roškar et al. (2008a) pointed out. Few of the particles (2%–6%) were already present in the outer disk, this is expected since the disk size is significantly smaller at that time, and by no means should be taken as an indication that the present SFR in the outer disk has such a little weight. The rest (20%–34%) were located outside of the galaxy either in smaller objects that merged in or diffuse gas. The fact that most of the stars in the outer disk originate in the inner disk means that the star formation taking place in the outer disk is sub-dominant when compared with the stars that got transported there by secular processes, possibly driven by spiral arms, or got scattered there in a merger process. In the rest of panels of Figure 4.5 we show for one of the galaxies the radial distances of different types of particles at $z = 0.9$ versus their corresponding distances at $z = 0$. The

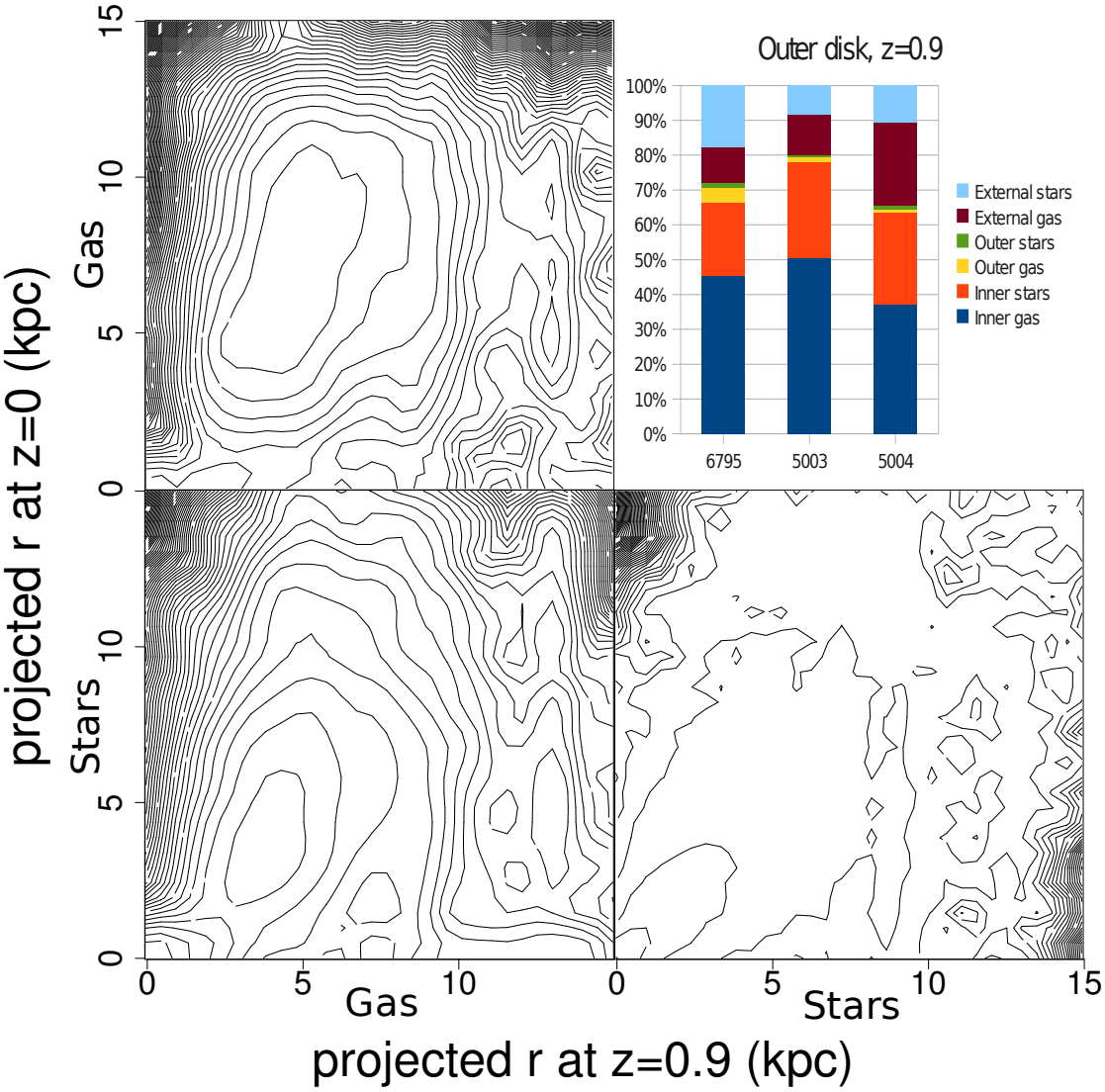

Figure 4.5: Top-right panel: Location at $z = 0.9$ of the outer disk stars at $z = 0$. As an example, the other panels contain contour plots of the evolution of the radial position of particles from $z = 0.9$ to $z = 0$.

bottom-right panel displays stellar particles born before $z = 0.9$ (old-star migrations), while the bottom-left shows particles that become stellar after $z = 0.9$ (younger star progenitor migrations). Finally, in the top-left panel we give results for gas particles. We can clearly see that old stellar particles have migrated to the outer region. The trend for stars born after $z = 0.9$ and with $r <$3 kpc at $z = 0.9$ is even clearer, although these are a minority. Gaseous particles also migrate. We then conclude that such migrations are likely the main origin of the U-shaped age profile and, therefore, of the luminosity break.

Chapter 5

Ongoing applications, summary and discussion

> There is a theory which states that if
> ever anyone discovers exactly what
> the Universe is for and why it is here,
> it will instantly disappear and be
> replaced by something even more
> bizarre and inexplicable.
> There is another theory which states
> that this has already happened.
>
> *The Restaurant at the End of the Universe*
> Douglas Adams

There are many open subjects in the field of galaxy formation and evolution to which P-DEVA can be (and is already) applied. This Chapter is devoted to detail further applications of the P-DEVA code that are not detailed in this text, along with a brief summary of the results presented in this PhD thesis and discussion of future prospects.

5.1 Ongoing applications of the P-DEVA code

This work has begun with a technical development, namely the parallelization of a highly sophisticated AP^{3}M+SPH code such as DEVA. While this is an arid task, it opens the door to much better simulations that make possible more detailed studies of the galaxy formation process. This is analogous to the construction of a new telescope: it takes lots of time and resources and is not astrophysically interesting by itself, but allows to obtain scientifically interesting results in the upcoming years. We believe the P-DEVA

code will produce significant results in the future. In this section we detail some of the ongoing work that uses P-DEVA to undertake several problems in galaxy formation.

5.1.1 GALFOBs series of simulations

The largest simulations undertaken so far with the P-DEVA code are those run in the fall and winter of 2008-2009 on the HLRB-II SGI Altix 4700 system (see Section 2.7) during the fall and winter of 2008-2009. The simulations are all based on a full box of 80 Mpc (56 Mpc/h) per side, with initial conditions based on the latest cosmological data from the WMAP5 site with the lcdm+sz+lens+run model and the wmap5+bao+snall+lyapost data[1].

In order to generate the initial conditions, we used the parallel MPgrafic code (Prunet et al., 2008). This code has some advantages over alternatives such as DEVA's own INITDEVA, IC (Sirko, 2005) or the original non-parallel version of grafic (Bertschinger, 2001) that make its use desirable for this project. Besides its speed and parallel nature that make it able to generate much larger initial conditions much faster, it also allows for the *a posteriori* increase of the resolution of the already-generated initial conditions. With minor modifications to the MPgrafic code, this would open the possibility for the re-simulation of selected objects with improved resolution and/or physics without having to generate full box high-resolution initial conditions that effectively limit the achievable maximum resolution to that of the initial conditions first generated.

The full box of 80 Mpc per side with 2×512^3 particles was run for the whole period using 64 cpus and without any chemical evolution or gas feedback. Given the poor scalability of the code beyond that number of CPUs, it was established that such simulation would several months in order to reach $z = 0$. In order to be able to obtain galaxies at $z = 0$, several sub-boxes extracted from the full box were run. These sub-boxes consisted of instances of the full box where the gas and dark matter particles had been replaced for coarser (at an effective resolution of 256 particles per box side) non-collisional particles, except for selected cubic regions where the original particles remained. This allows for the selected sub-volume to reach $z = 0$ in a much shorter time interval at the cost of computing gravity for particles that later will be of no interest for the formation of galaxies in the selected sub-volume, but that are required in order to incorporate the effect of tidal forces in the sub-volume.

In this way, the full volume was partitioned into eight 40 Mpc and sixty four 20 Mpc

[1]Parameters available at: `http://cmbdata.gsfc.nasa.gov/product/map/current/params/lcdm_sz_lens_run_wmap5_bao_snall_lyapost.cfm`

Sim id.	L [Mpc]	z_{end}
2000	80	3.503
2017	40	0.742
2010	40	1.877
2011	40	1.749
2012	40	6.218
2013	40	6.378
2100	20	0.000
2108	20	0.637
2109	20	0.000
2110	20	0.010
2111	20	0.632
2112	20	1.586
2113	20	1.038
2114	20	0.174
2115	20	0.162

Table 5.1: Simulations ran as part of the GALFOBs project

per side sub-boxes[2], and initial conditions corresponding to each of these sub-boxes were generated. Five of the 40 Mpc and nine of the 20 Mpc sub-boxes were run. The list of simulations, including the achieved redshift when the run period ended is listed on Table 5.1.

These simulations are similar in resolution and physics to those already presented in previous works described in section 5.1.2, but the simulated volume is several times larger and provides more statistics on the studies of the mass assembly process in galaxy formation.

Additionally, in order to complement the previous large-scale simulations with no chemical evolution, a full-box simulation with half the box size (40 Mpc) of the full box and sharing the same cosmological parameters and resolution, was run until $z = 1$ and is currently still running until $z = 0$ in another supercomputer. This simulations includes all the physics described in Chapter 3 of this work and is the largest volume simulated so far using the P-DEVA code. Another complementary simulation, with much higher resolution (2×256^3 particles in a 10 Mpc per side box) is also running in a local computer. This latest simulation has the same resolution and physics of galaxies 5003 and 5004 described in Chapter 4, but has the full box instead and should be able to provide much more statistics and varieties of galaxies at such resolutions.

5.1.2 Work on the formation of elliptical galaxies and the fundamental plane

As part of his Thesis work at UAM, José Oñorbe (2009) analysed several simulations in order to study the formation process of elliptical galaxies and the build up of the fundamental plane, together with the reasons for its tilt with respect to the virial relations. Many of the simulations employed in this work were performed with P-DEVA.

The thorough study, and the results described in this work provide us with a comprehensive model for the formation and evolution of elliptical galaxies. It also explains most of their properties and trends such as the aforementioned fundamental plane, profiles, missing baryons, formation timescales and its dependence with mass (downsizing), gas accretion modes, or shape and size evolution with redshift. It also relates them only to very simple physics, such as gravity and hydrodynamics and cosmological conditions. Moreover, it shows how all those properties are, for the most part, independent of the particular choice of sub-resolution physics parameters, modeled in this work only with

[2] An additional "buffer zone" of 2.8 Mpc was added in each direction in order to have full volumes that could be later trimmed and used for analysis.

a simple prescription for star formation (that described in Chapter 3 of this work), but no gas or energy feedback.

5.1.3 Further work on the formation and properties of spiral galaxies

A Thesis currently being developed by Mariola Doménech-Moral at UMH will extend the work presented here and study in more depth, and more systematically, the process of formation and evolution of spiral galaxies. For this purpose, high-resolution cosmological resimulations of individual objects such as the ones presented in Chapter 4 of this work will be used.

The new study will include enough galaxies to have statistical significance. To this end, more galaxies, in addition to those presented in Chapter 4, will be simulated. It will also detail more properties, such as chemical abundance profiles, redshift evolution, accretion rates of gas and satellites, or merger processes, which have not been studied in this Thesis.

Resolution should be enough to study the double structure of thin and thick disks present in observed disk galaxies, as well as the main drivers behind the formation of both components and the survival of the thin disk after mergers happen.

5.1.4 Study of the satellite systems of disk galaxies

Another important study performed using P-DEVA (and DEVA) is the study of satellites of spiral galaxies (Benjouali et al. submitted). This work has been mainly performed by Latifa Benjouali, Mari Ángeles Gómez-Flechoso and Héctor Artal. In this work, the satellite orbital structure of a sample of virtual disk-satellite systems, identified at $z = 0$, has been statistically analysed both in three-dimensions (3D) and in projection along random directions, mimicking observational strategies. Systems have been classified into different categories: rich and poor systems. The study has found that satellite orbit distributions are polar for rich systems and planar for poor systems, resulting in an isotropic distribution on average.

5.1.5 Study of groups of galaxies in simulations

The Master Thesis by Paola Alpresa at La Laguna, used P-DEVA simulations as a fundamental tool. There she studied several simulations performed with P-DEVA and studied the clustering of galaxies in low density and high density environments. To that end she used group-finding algorithms and both physical and observational criteria in

order to identify isolated galaxies and groups. This is the first time that a specific study of galaxy groups has been performed on galaxies obtained in cosmologically significant volumes simulated including baryonic physics. Although the work is still in progress, it has already produced several results, for example: (i) multiple galaxy systems sample denser environments at any redshift and isolated galaxies sample the lower ones; (ii) more massive galaxies tend to live in groups and in denser environments and tend to be supported by velocity dispersion; and (iii) the isolated or non-isolated character of a given galaxy tends to be conserved along cosmic time; (iv) mass-aggregation trees depict a two-phase process, a fast phase at high-redshift and a slow phase at lower redshift; (v) the secondary-to-primary galaxy distance indicator shows that well-balanced groups are stable, as it does not change significantly since capture happens.

5.1.6 Dust extinction and re-emission from P-DEVA simulated galaxies

As part of his PhD Thesis at INAF/SISSA in Trieste, Andrew Schurer (GRASIL-3D Schurer, 2009, in collaboration with A. Serna and R. Domínguez-Tenreiro), has adapted the GRASIL code (Silva et al., 1998) to high-resolution galaxies obtained with the P-DEVA code. This allows to compute the effects of dust in the emitted light of galaxies using some assumptions that relate gas properties and abundances to its dust content. Dust processing of ultraviolet light emitted by young stars has a non-negligible effect on galaxy spectra, decreasing the UV output and obtain synthetic spectra generated from simulated galaxies from sub-mm wavelength until the UV, opening the window for a new whole range of observed parameters that can be modeled with simulations and compared in order to find consistency. Results so far are encouraging. Synthetic spectra obtained from P-DEVA simulated disk galaxies, such as the ones presented in Chapter 4, are able to closely match spectra of disk galaxies such as M51 or high-redshift ($z = 2$) galaxies observed in the sub-millimetric.

5.2 Summary and discussion

In this work we have presented an almost self-contained study of some aspects of the formation of galaxies using hydrodynamical cosmological simulations. Briefly, starting with the sequential version of the DEVA code (Serna et al., 2003), our main tasks were:

1. Restructuring and parallelizing the code, making it both more efficient and able to run on machines with several processors. This provides the opportunity of running

simulations with larger boxes and with a higher resolution.

2. Developing a model that allows us to include the effects of star formation feedback into the simulation. Since the chemical composition of the gas affects its cooling rate, this in turn has an effect on the global properties of the objects. Both the chemical feedback and the cooling rate have been modeled taking into account the detailed chemical abundances.

3. Applying the improved code and newly developed algorithms to simulate the formation of realistic spiral galaxies and study the origin of their broken luminosity profiles.

Diverse methods and codes exist in the literature that solve the equations of gravity and hydrodynamics in an expanding universe, and that hence can tackle the problem of galaxy formation in a cosmological context. As was explained in Chapter 1, the methods used to solve the equations of gravity can be roughly classified in three main categories: (i) Particle-Mesh (PM), (ii) Tree, and (iii) Adaptive Mesh Refinement (AMR); while the methods used to solve they equations of fluid dynamics can be classified in two: (i) Lagrangian (SPH-like), and (ii) Eulerian. There are many parallel codes that use Tree methods[3] combined with SPH such as Gadget (Springel, 2005), Gasoline (Wadsley et al., 2004), GCD+ (Kawata & Gibson, 2003), or VINE (Wetzstein et al., 2009); and also many parallel eulerian codes such as RAMSES (Teyssier, 2002), AMIGA (Knebe et al., 2001), Enzo (O'Shea et al., 2004) or ART (Kravtsov, 1999). However, there is only one parallel code that uses AP^3M combined with SPH, Hydra, with MPI (Pringle et al., 2001; Thacker, 2003) and OpenMP (Thacker & Couchman, 2006) versions. Since diversity of codes is good, both as competition, and as a way to test their correctness, there was clearly a need for another parallel code in the AP^3M+SPH niche, a void that we hope has been partially fulfilled by the P-DEVA code.

Since its inception, the DEVA code has been successfully used to study the formation of galaxies, both spiral (Sáiz, 2003; Sáiz et al., 2002; Domínguez-Tenreiro et al., 2003, 2008; Martínez-Serrano et al., 2009) and elliptical (Domínguez-Tenreiro et al., 2003; Sáiz et al., 2003, 2004; Domínguez-Tenreiro et al., 2004; Oñorbe et al., 2005; Domínguez-Tenreiro et al., 2006; Oñorbe et al., 2006, 2007; González-García et al., 2009) and has consistently proved to be able to reproduce galaxies with realistic individual and ensemble

[3] Although the latest tree codes typically combine a PM evaluation of the long-range forces with a tree for the short-range ones. This also offers the advantage of automatically taking care of periodic conditions.

properties. The parallel version of DEVA allows for much more detailed studies both of individual galaxies and ensembles of galaxies, while retaining the desirable conformance with conservation laws of the original DEVA code.

As described in Chapter 2, the parallelization has been introduced incrementally, by means of OpenMP directives and code reshaping where it was necessary or advantageous. The main positive aspects of this approach are its relative simplicity and the possibility of reusing the preexisting code while incrementally parallelizing parts of the code and always retaining its functionality, thus allowing to test its correctness after each section is parallelized. The downsides are related to the lack of control over the identities of particles assigned to each node, a fact that hampers the ability of the code to scale beyond ~ 60 CPUs. Significant improvements on the scalability of the P-DEVA code are thus required, if we want to be able to run the code on hundreds of CPUs, and hence be able to tackle much larger cosmological volumes with enough resolution to study the formation of individual galaxies. To that end, future work will also include the development from the ground up of a new version of the code that is parallelized with the more explicit MPI library instead of OpenMP. This will allow for a finer control over the load distribution and to achieve a better scalability.

Besides the rather technical task of parallelizing the code, another important part of this work deals with improvements in the sub-resolution physics model included in the DEVA code. In Chapter 3, we describe a new model for chemical feedback and cooling. The techniques applied in order to do so are rather novel and (to the best of our knowledge) are used here for the first time in the context of astrophysical simulations (the case of cooling and dimension reduction regression) or in the context of SPH (Q_{ij} matrices and the computation of yields). The underlying philosophy behind this model is to include the dependence of both processes not only on the total metallicity, as do most models currently in use, but also on the individual abundance of each isotope traced by the code. Furthermore we do so without significantly hampering the speed of the code[4]. The dependence of the gas dynamics on the cooling rate justifies the inclusion of such an elaborate model, even for studies not focused on the chemical evolution.

When compared with other currently used implementations of chemical evolution (e.g. Lia et al., 2002; Kawata & Gibson, 2003; Sommer-Larsen et al., 2005; Scannapieco et al., 2005; Kobayashi et al., 2007; Tornatore et al., 2007; Wiersma et al., 2009b) our "Q_{ij} method" is more complex, but most of its complexity is hidden in the Q_{ij} matrix com-

[4]There is an unavoidable slowdown in the total wallclock time required by simulations due to the reduction in the timestep imposed by an enhanced cooling rate combined with Courant's condition.

putation itself. Therefore interpreting its results can be difficult in some cases. However, its foundations are solid and the matrices that we use have been used in many synthetic studies (see e.g. Ferrini et al., 1992, and the succesive series of papers). We have shown that the dependence of chemical evolution on the detailed abundances plays an important role in determining the evolution of the relative abundances (such as α-element to Fe ratios) in the gas and stellar populations. Previous works (Tassis et al., 2008; Brooks et al., 2007; de Rossi et al., 2007; Mouhcine et al., 2008; Finlator & Davé, 2008) have studied the formation of the mass-metallicity or luminosity-metallicity relations in populations of galaxies with cosmological simulations. While they succeed in reproducing such relations (albeit for reportedly different reasons), none of them has so far studied the relative abundances of elements and their relation with mass. Our current implementation based on the Q_{ij} matrices takes into account the influence of non-solar ratios in the stellar yields. Hence, we believe that is better suited to reproduce and provide clues of the origin of such relation.

The implementation of the cooling also takes into account non-solar ratios for the cooling rate. We found that among other improvements (see Chapter 3), it alleviates the problem of overcooling since the solar pattern of abundances is not "typical" and most gas particles show less cooling when all the full abundances are taken into account. However, while our model is detailed for the case it was designed for, is lacking in two main areas: (i) it doesn't include the effects of a UV/X-ray photoionizing background at the epoch of reionization, as some recent studies that also include detailed dependence on the abundance of each element do (Wiersma et al., 2009a) and hence assumes that the gas is in collisional ionization equilibrium at all times; (ii) it limits the cooling temperature to 10^4 K, an assumption that would need to be relaxed if higher-resolution simulations, resolving the cool component of disks, are to be run. There are works that already try to include such effects (Maio et al., 2007).

As discussed in Section 3.2.5, we do not explicitly include energy feedback from supernovae explosions in our simulations, these are however implicitly taken into account through the Schmidt–Kennicutt law as a mechanism for the self-regulation of star-formation.

Finally, our code is being applied to several open problems in the field of galaxy formation and evolution. As was explained above (see Section 5.1), the fundamental plane of ellipticals, the formation of disks, the satellite systems of disk galaxies, groups of galaxies, or the influence of dust on the spectra of simulated galaxies are being studied with simulations performed with the P-DEVA. Particularly, as was explained in Chapter

4, in this Thesis we have applied the methods and code developed in the previous chapters in a study of the formation of spiral galaxies. The simulations performed in our study are able to produce realistic objects with properties such as radial sizes, vertical profiles, luminosity, color profiles, and rotation curves that are compatible with observations. They also follow the Tully-Fischer relation, and show a comparatively high disk-to-total ratio. This feature is particularly difficult to achieve in simulations that do not include explicit energy feedback. These tend to generate disks with more massive bulges than disks (see Piontek & Steinmetz, 2009, for a recent discussion on the subject), and require the inclusion of additional processes (such as the aforementioned explicit energy feedback from supernova) in order to expel the gas and reduce the mass of the bulge.

The study of the simulated galaxies has shown that they present a broken luminosity profile with no apparent break on the mass profile. This has only recently been suspected to occur in most type-II spiral galaxies (Bakos et al., 2008). We have investigated the origin of this behavior, and have found it to be related to a sudden reduction in the star formation rate (SFR) $\sim$ 1 disk scalelenghts beyond the break. This result, combined with an exponential stellar mass profile, suggests that a significant fraction of the stars located in the outer part of the galaxies was formed elsewhere and later redistributed into the outer parts. The explicit study of this possibility in this Thesis shows that this is indeed the case: stellar migrations play a main role in populating the outer disks of the galaxies. We plan on extending the study of such galaxies to include the evolution of their properties with redshift, the role of mergers vs inflows in their formation process, or the metallicity distribution and its evolution.

Finally we plan to extend our work to ensembles of galaxies, and study the global distribution of their properties over several orders of magnitude in mass. Global trends such as the mass-metallicity, the color-luminosity or the mass-[α/Fe] relations are known to be reproduced by our code in some preliminary simulations. We plan to systematically study such trends and their origin with the help of the tools presented in this work.

Appendix A

Resumen y discusión

En este trabajo hemos presentado un estudio prácticamente autocontenido de algunos aspectos de la formación de galaxias, usando para ello simulaciones cosmológicas que incluyen la dinámica del gas y la formación estelar. De forma breve, a partir de la versión secuencial del código DEVA (Serna et al., 2003), nuestra tarea ha consistido principalmente en:

1. Reestructurar y paralelizar el código, haciéndolo más eficiente a la vez que capaz de correr en máquinas con más de un procesador. Esto permite realizar simulaciones con cajas más grandes y mayor resolución.

2. Desarrollar un modelo que nos permite incluir efectos del feedback de la formación estelar en la simulación tales como el enriquecimiento químico. Dado que la composición química del gas afecta a su tasa de enfriamiento, esto al final tiene un efecto en las propiedades globales de los objetos. Tanto el feedback de elementos químicos como la tasa de enfriamiento han sido modelados teniendo en cuenta la composición química detallada del gas y las estrellas.

3. Aplicar el código mejorado y los algoritmos desarrollados para simular la formación de galaxias espirales realistas y estudiar el origen de sus perfiles de luminosidad rotos.

Existen en la literatura varios métodos y códigos que resuelven las ecuaciones de la gravedad y la hidrodinámica en un universo en expansión, y que, por tanto, pueden abordar el problema de la formación de galaxias en un contexto cosmológico. Como explicamos en el Capítulo 1, los métodos usados para resolver las ecuaciones de la gravedad pueden ser clasificados en tres categorías principales: (i) Particle-Mesh (PM), (ii) Tree, y (iii) Adaptive Mesh Refinement (AMR); mientras que los métodos usados para resolver

las ecuaciones de la dinámica de fluidos pueden ser clasificados en dos: (i) Lagrangianos (tipo smoothed particle hydrodynamics, SPH), y (ii) Eulerianos. Hay varios códigos paralelos que usan métodos Tree[1] combinados con SPH tales como Gadget (Springel, 2005), Gasoline (Wadsley et al., 2004), GCD+ (Kawata & Gibson, 2003), o VINE (Wetzstein et al., 2009); también hay varios códigos eulerianos tales como RAMSES (Teyssier, 2002), AMIGA (Knebe et al., 2001), Enzo (O'Shea et al., 2004) or ART (Kravtsov, 1999). Sin embargo, tan sólo hay un código paralelo que use AP^3M combinando con SPH, Hydra, con versiones MPI (Pringle et al., 2001; Thacker, 2003) y OpenMP (Thacker & Couchman, 2006). Dado que la diversidad de códigos es es buena, bien incentivando la competitividad, bien como un método de comprobar la corrección de los mismos, había una necesidad clara de otro código paralelo en el nicho AP^3M+SPH, un vacío que esperamos sea parcialmente rellenado por el código P-DEVA.

Desde su concepción, el código DEVA se ha aplicado de forma exitosa al estudio de la formación de galaxias, tanto espirales (Sáiz, 2003; Sáiz et al., 2002; Domínguez-Tenreiro et al., 2003, 2008; Martínez-Serrano et al., 2009) como elípticas (Domínguez-Tenreiro et al., 2003; Sáiz et al., 2003, 2004; Domínguez-Tenreiro et al., 2004; Oñorbe et al., 2005; Domínguez-Tenreiro et al., 2006; Oñorbe et al., 2006, 2007; González-García et al., 2009) y ha demostrado de forma consistente su capacidad de reproducir en las simulaciones galaxias con propiedades realistas tanto a nivel individual como en conjunto. La versión paralela de DEVA permite estudios mucho más detallados tanto de galaxias individuales como de conjuntos de galaxias, a la vez que retiene las deseables propiedades tales como el cumplimiento de las leyes de conservación de su predecesor.

Tal como describimos en el Capítulo 2, la paralelización ha sido introducida de forma incremental, mediante directivas OpenMP y reorganización del código allí donde era necesario o ventajoso. Los principales aspectos positivos de esta estrategia son la posibilidad de reutilizar partes del código y el conservar la funcionalidad original en todas las fases del desarrollo, permitiendo así comprobar su corrección después de la paralelización de cada sección. Las desventajas están relacionadas con la falta de control del número de partículas asignadas a cada nodo, un hecho que limita la capacidad del código para escalar más allá de $\sim$ 60 CPUs. Se requieren, por tanto, mejoras significativas en la escalabilidad del código P-DEVA si queremos ser capaces de correr el código en cientos de procesadores para poder abordar volúmenes cosmológicos mucho más grandes con

[1]Nótese que los códigos Tree recientes combinan una evaluación PM para las fuerzas de larga distancia y un Tree para las distancias cortas. Esto también tiene la ventaja de incluir de forma natural las condiciones periódicas.

resolución suficiente como para estudiar la formación de galaxias individuales. Para tal fin, el trabajo futuro incluye el desarrollo de una nueva versión partiendo de cero que estará paralelizada con la librería MPI (más explícita) en lugar de OpenMP. Esto permitirá un control más fino en la distribución de carga y la consecución de una mayor escalabilidad.

Además de la tarea más técnica de la paralelización del código, otra importante parte de este trabajo se ocupa de las mejoras en el modelo de la física a escalas subrresolución incluido en el código de Deva. En el Capítulo 3, describimos un nuevo modelo para la retroalimentación química y el enfriamiento. Las técnicas aplicadas son novedosas y (hasta donde sabemos) se utilizan aquí por primera vez en el contexto de las simulaciones de de formación de galaxias (el caso de el enfriamiento y la regresión con reducción de dimensiones), o en el contexto de SPH (matrices Q_{ij} matrices y el cálculo de yields estelares). La filosofía que subyace detrás de este modelo es el incluir la dependencia de los dos procesos no sólo en la metalicidad total, como hacen la mayoría de modelos actualmente en uso, sino también en la abundancia individual de cada isótopo trazado por el código. Además, lo hacemos sin obstaculizar en exceso la velocidad del código[2]. La dependencia de la dinámica del gas en la tasa de enfriamiento justifica la la inclusión de este modelo un tanto elaborado, incluso para los estudios no se centran en la evolución química.

En comparación con otras implementaciones de la evolución química que se utilizan actualmente (por ejemplo Lia et al., 2002; Kawata & Gibson, 2003; Sommer-Larsen et al., 2005; Scannapieco et al., 2005; Kobayashi et al., 2007; Tornatore et al., 2007; Wiersma et al., 2009b) nuestros "método Q_{ij}" es más complejo, pero la mayoría de sus complejidad se oculta en el cálculo de la matriz Q_{ij} en sí. Por tanto la interpretación de sus resultados puede ser difícil en algunos casos. Sin embargo, su cimientos son sólidos y las matrices que utilizamos han sido usados en muchos estudios sintéticos de formación de galaxias (véase, por ejemplo Ferrini et al., 1992, y la serie sucesiva de artículos). Hemos demostrado que la dependencia de la evolución química en las abundancias detalladas desempeña un papel importante en la determinación de la la evolución de las abundancias relativas (por ejemplo, cocientes de elementos α respecto al Fe) en el gas y en las poblaciones estelares. Trabajos anteriores (Tassis et al., 2008; Brooks et al., 2007; de Rossi et al., 2007; Mouhcine et al., 2008; Finlator & Davé, 2008) han estudiado la formación de

[2]Hay una desaceleración inevitable en el tiempo total requerido por las simulaciones, debido a la reducción del paso de tiempo impuesta por una mayor tasa de enfriamiento combinado con la condición de Courant.

la relación masa-metalicidad o masa-luminosidad de las relaciones en poblaciones de galaxias con simulaciones cosmológica. Si bien tienen éxito en la reproducción de esas relaciones (aunque por por diferentes razones), ninguno de ellos hasta el momento ha estudiado la relación entre los cocientes de abundancias de elementos y su relación con la masa. Nuestra implementación actual basada en las matrices Q_{ij} tiene en cuenta la influencia de los cocientes no solares en los yields estelares. Por lo tanto, creemos que se adapta mejor a reproducir y proporcionar pistas sobre el origen de dicha relación.

En la implementación del enfriamiento también se tienen en cuenta las proporciones no solares para la la velocidad de enfriamiento. Encontramos que entre otras mejoras (véase el Capítulo 3, se alivia el problema del sobreenfriamiento, ya que el patrón de abundancias solar es "típico", y la mayoría de las partículas de gas muestran menos de enfriamiento cuando todas la abundancias se tienen en cuenta. Sin embargo, mientras que nuestro modelo es detallado para el caso que fue diseñado, le falta más detalle en los dos principales áreas: (i) no incluye los efectos de una fondo fotoionizante de UV/rayos X en la época de re-ionización, como algunos estudios recientes que también incluyen la dependencia detallada sobre la abundancia de cada elemento (Wiersma et al., 2009a), y por lo tanto asume que el gas está en ionizado en equilibrio colisional en todo momento; (ii) limita la temperatura de refrigeración a 10^{4} K, un supuesto que tendría ser relajado, si se quieren hacer simulaciones de mayor resolución que resuelvan la componente fría de los discos. Hay trabajos que ya tratar de incluir a tales efectos (Maio et al., 2007).

Como se discutió en la Sección 3.2.5, no incluimos explícitamente el feedback explícito de energía liberada en explosiones de supernovas en nuestras simulaciones, este es, sin embargo tenido implícitamente en cuenta a través de la ley de Schmidt–Kennicutt como un mecanismo de autorregulación de la formación de estelar.

Por último, nuestro código se aplica a varios problemas abiertos en el ámbito de la la formación de galaxias y su evolución. Como se ha explicado anteriormente (véase la Sección 5.1), el plano fundamental de las elípticas, la formación de discos, los sistemas de satélites de galaxias de disco, los grupos de galaxias, o la influencia del polvo en los espectros de las galaxias simuladas se están estudiando con las simulaciones realizadas con el código P-DEVA. En particular, como se explicó en Capítulo 4, en esta Tesis se han aplicado los métodos y el código desarrollados en los capítulos anteriores en un estudio de la formación de las galaxias espirales. Las simulaciones realizadas en nuestro estudio son capaces de producir objetos realistas con propiedades tales como el tamaño radial, perfiles verticales, luminosidad, perfiles de color, y curvas de rotación que son compatibles con las observaciones. También siguen la relación Tully-Fischer, y muestran

una relación disco a total relativamente alta. Esta característica es particularmente difícil de lograr en simulaciones que no incluyen un feedback de energía explícito. Estas tienden a generar discos con bulbos más masivos que los discos (ver Piontek & Steinmetz, 2009, para una reciente discusión sobre el tema), y exigir la inclusión de procesos adicionales (como el ya mencionado feedback explícito de energía) para expulsar el gas y reducir la masa del bulbo.

El estudio de las galaxias simuladas ha demostrado que presentan un perfil de luminosidad roto sin aparente ruptura en el perfil de masa. Esto sólo ha Recientemente se ha propuesto que dicha rotura se produce en la mayoría de las galaxias espirales de tipo II (Bakos et al., 2008). Hemos investigado el origen de este comportamiento, y hemos encontrado que está relacionado con una disminución repentina de la tasa de formación estelar (SFR) ~ 1 escalas características del disco más allá de la rotura. Este resultado, combinado con perfil exponencial para la masa estelar, sugiere que una fracción significativa de la las estrellas, situadas en la parte externa de las galaxias se formó en otros lugares y después fueron redistribuidas en las partes exteriores. El estudio explícito de este posibilidad en esta Tesis muestra que este es el caso: las migraciones estelares juegan un papel principal en la formación de los discos estelares externos de las galaxias. En el futuro, planeamos de ampliar el estudio de las galaxias de disco para incluir la evolución de sus las propiedades con el redshift, el papel de las fusiones frente a la acrección de gas en su proceso de formación, o la distribución de metalicidad y su evolución.

Por último, tenemos previsto ampliar nuestro trabajo a conjuntos de galaxias, y estudiar la distribución global de sus propiedades a lo largo de varios órdenes de magnitud en la en masa. Relaciones globales tales como la masa-metalicidad, el color o la luminosidad (masa)-[α/Fe] son reproducidas por nuestro código en algunas simulaciones preliminares. Tenemos la intención de estudiar sistemáticamente estas tendencias y sus de origen con la ayuda de las herramientas presentadas en este trabajo.

Bibliography

Aarseth, S. J. 1963, MNRAS, 126, 223

Abadi, M. G., Navarro, J. F., Steinmetz, M., & Eke, V. R. 2003, ApJ, 591, 499, arXiv:astro-ph/0211331

Abazajian, K. et al. 2003, AJ, 126, 2081, arXiv:astro-ph/0305492

Agertz, O. et al. 2007, MNRAS, 380, 963, arXiv:astro-ph/0610051

Alimi, J.-M., Serna, A., Pastor, C., & Bernabeu, G. 2003, Journal of Computational Physics, 192, 157

Alpher, R. A., Bethe, H., & Gamow, G. 1948, Physical Review, 73, 803

Alpher, R. A., & Herman, R. C. 1949, Physical Review, 75, 1089

Anders, E., & Grevesse, N. 1989, Geochim. Cosmochim. Acta, 53, 197

Antonioletti, M., Jenkins, A., & Nelson, A. 1994, Memorie della Societa Astronomica Italiana, 65, 1213

Azzollini, R., Trujillo, I., & Beckman, J. E. 2008a, ApJ, 679, L69, 0804.2336

——. 2008b, ApJ, 684, 1026, 0805.2259

Bader, D. A., & JáJá, J. 1999, J. Parallel Distrib. Comput., 58, 92

Bagla, J. S. 2002, Journal of Astrophysics and Astronomy, 23, 185, arXiv:astro-ph/9911025

Bakos, J., Trujillo, I., & Pohlen, M. 2008, ApJ, 683, L103, 0807.2776

Balcells, M., Graham, A. W., & Peletier, R. F. 2007, ApJ, 665, 1104, arXiv:astro-ph/0404381

Barber, C. B., Dobkin, D. P., & Huhdanpaa, H. 1996, ACM Trans. Math. Softw., 22, 469

Barnes, J., & Hut, P. 1986, Nature, 324, 446

Battaglia, M., de Roeck, A., Ellis, J., Gianotti, F., Matchev, K. T., Olive, K. A., Pape, L., & Wilson, G. 2001, European Physical Journal C, 22, 535, arXiv:hep-ph/0106204

Bell, E. F., McIntosh, D. H., Katz, N., & Weinberg, M. D. 2003, ApJS, 149, 289

Berczik, P. 1999, A&A, 348, 371

Berczik, P. P., & Petrov, M. I. 2001, Kinematika i Fizika Nebesnykh Tel, 17, 213, arXiv:astro-ph/0106093

Bernardi, M. et al. 2003, AJ, 125, 1866, arXiv:astro-ph/0301626

Bertschinger, E. 2001, ApJS, 137, 1, arXiv:astro-ph/0103301

Bethe, H. A. 1939, Physical Review, 55, 434

Bially, T. 1969, IEEE Transactions on Information Theory, 15, 658

Bircsak, J., Craig, P., Crowell, R., Cvetanovic, Z., Harris, J., Nelson, C., & Offner, C. 2000, in ACM/IEEE 2000 Conference on Supercomputing, 48–48

Bode, P., Ostriker, J. P., & Turok, N. 2001, ApJ, 556, 93, arXiv:astro-ph/0010389

Boissier, S., & Prantzos, N. 1999, MNRAS, 307, 857

——. 2000, MNRAS, 312, 398

Bond, J. R., Centrella, J., Szalay, A. S., & Wilson, J. R. 1984, MNRAS, 210, 515

Borgani, S., Governato, F., Wadsley, J., Menci, N., Tozzi, P., Quinn, T., Stadel, J., & Lake, G. 2002, MNRAS, 336, 409, arXiv:astro-ph/0205471

Bournaud, F., Elmegreen, B. G., & Elmegreen, D. M. 2007, ApJ, 670, 237, 0708.0306

Bowen, I. S., & Wyse, A. B. 1939, Lick Observatory Bulletin, 19, 1

Brook, C. B., Kawata, D., Gibson, B. K., & Freeman, K. C. 2004, ApJ, 612, 894, arXiv:astro-ph/0405306

Brooks, A. M., Governato, F., Booth, C. M., Willman, B., Gardner, J. P., Wadsley, J., Stinson, G., & Quinn, T. 2007, ApJ, 655, L17, arXiv:astro-ph/0609620

Bruzual, G., & Charlot, S. 2003, MNRAS, 344, 1000

Bryan, G. L., & Norman, M. L. 1995, in Bulletin of the American Astronomical Society, Vol. 27, Bulletin of the American Astronomical Society, 1421–+

Bryan, G. L., Norman, M. L., Stone, J. M., Cen, R., & Ostriker, J. P. 1995, Computer Physics Communications, 89, 149

Burstein, D., Bertola, F., Buson, L. M., Faber, S. M., & Lauer, T. R. 1988, ApJ, 328, 440

Burstein, D., Faber, S. M., Gaskell, C. M., & Krumm, N. 1984, ApJ, 287, 586

Butz, A. 1969, Journ. Computer and System Sciences, 3, 128

Cano, B., & Sanz-Serna, J. 1997, SIAM Journal on Numerical Analysis, 1391

Carollo, C. M., Danziger, I. J., & Buson, L. 1993, MNRAS, 265, 553

Carraro, G., Lia, C., & Chiosi, C. 1998, MNRAS, 297, 1021

Cen, R., & Ostriker, J. P. 1992, ApJ, 399, L113

——. 1999, ApJ, 519, L109, arXiv:astro-ph/9903207

Cen, R. Y., Ostriker, J. P., Jameson, A., & Liu, F. 1990, ApJ, 362, L41

Chabrier, G. 2003a, PASP, 115, 763

——. 2003b, ApJ, 586, L133

Chiappini, C., Matteucci, F., & Gratton, R. 1997, ApJ, 477, 765

Clayton, D. D. 1987, ApJ, 315, 451

Colella, P., & Woodward, P. R. 1984, Journal of Computational Physics, 54, 174

Cooley, J. W., & Tukey, J. W. 1965, Mathematics of Computation, 19, 297

Couchman, H. M. P. 1986, PhD thesis, King's College, Cambridge

——. 1991, ApJ, 368, L23

Couchman, H. M. P., Pearce, F. R., Thomas, P. A., & Thacker, R. J. 2002, Hydra 4.2

Couchman, H. M. P., Thomas, P. A., & Pearce, F. R. 1995, ApJ, 452, 797, arXiv:astro-ph/9409058

Curtis, H. D. 1920, JRASC, 14, 317

Dalla Vecchia, C., & Schaye, J. 2008, MNRAS, 387, 1431, 0801.2770

Dave, R., Dubinski, J., & Hernquist, L. 1997, New Astronomy, 2, 277, arXiv:astro-ph/9701113

Davidge, T. J., & Clark, C. C. 1994, AJ, 107, 946

Davis, M., Huchra, J., Latham, D. W., & Tonry, J. 1982, ApJ, 253, 423

de Jong, R. S. et al. 2007, ApJ, 667, L49, 0708.0826

de Rossi, M. E., Tissera, P. B., & Scannapieco, C. 2007, MNRAS, 374, 323, arXiv:astro-ph/0609243

Debattista, V. P., Mayer, L., Carollo, C. M., Moore, B., Wadsley, J., & Quinn, T. 2006, ApJ, 645, 209, arXiv:astro-ph/0509310

Díaz, A. I., & Tosi, M. 1986, A&A, 158, 60

Domínguez, A. 2000, Phys. Rev. D, 62, 103501, arXiv:astro-ph/0009414

Domínguez-Tenreiro, R., Martínez-Serrano, F. J., Serna, A., Mollá, M., & Oñorbe, J. 2008, in IAU Symposium, Vol. 245, IAU Symposium, ed. M. Bureau, E. Athanassoula, & B. Barbuy, 71–74

Domínguez-Tenreiro, R., Oñorbe, J., Sáiz, A., Artal, H., & Serna, A. 2006, ApJ, 636, L77

Domínguez-Tenreiro, R., Sáiz, A., & Serna, A. 2004, ApJ, 611, L5, arXiv:astro-ph/0407110

Domínguez-Tenreiro, R., Serna, A., Sáiz, A., & Sierra-Glez. de Buitrago, M. M. 2003, Ap&SS, 284, 397

Dubois, Y., & Teyssier, R. 2008, A&A, 477, 79, 0707.3376

Efstathiou, G., Fall, S. M., & Hogan, C. 1979, MNRAS, 189, 203

Elmegreen, B. G. 2002, ApJ, 577, 206, arXiv:astro-ph/0207114

——. 2003, Ap&SS, 284, 819, arXiv:astro-ph/0212166

Elmegreen, B. G., & Parravano, A. 1994, ApJ, 435, L121+

Erwin, P., Beckman, J. E., & Pohlen, M. 2005, ApJ, 626, L81, arXiv:astro-ph/0505216

Erwin, P., Pohlen, M., & Beckman, J. E. 2008, AJ, 135, 20, 0709.3505

Evrard, A. E. 1988, MNRAS, 235, 911

Evrard, A. E., Silk, J., & Szalay, A. S. 1990, ApJ, 365, 13

Fall, S. M. 1978, MNRAS, 185, 165

Ferguson, A., Irwin, M., Chapman, S., Ibata, R., Lewis, G., & Tanvir, N. 2007, Resolving the Stellar Outskirts of M31 and M33, ed. R. S. de Jong, 239–+

Ferrini, F., Matteucci, F., Pardi, C., & Penco, U. 1992, ApJ, 387, 138

Ferrini, F., Mollá, M., Pardi, M. C., & Díaz, A. I. 1994, ApJ, 427, 745

Ferrini, F., Penco, U., & Palla, F. 1990, A&A, 231, 391

Finlator, K., & Davé, R. 2008, MNRAS, 385, 2181, 0704.3100

Foyle, K., Courteau, S., & Thacker, R. J. 2008, MNRAS, 386, 1821, 0803.2716

Freeman, K., & Bland-Hawthorn, J. 2002, ARA&A, 40, 487

Freeman, K. C. 1970, ApJ, 160, 811

Frenk, C. S. et al. 1999, ApJ, 525, 554, arXiv:astro-ph/9906160

Friedman, A. 1922, Zeitschrift fur Physik, 10, 377

Frigo, M., & Johnson, S. G. 2005, Proceedings of the IEEE, 93, 216, special issue on "Program Generation, Optimization, and Platform Adaptation"

Fryxell, B. et al. 2000, ApJS, 131, 273

Fuhrmann, K. 1999, Ap&SS, 265, 265

Gadotti, D. A. 2009, MNRAS, 393, 1531, 0810.1953

Galli, D., Palla, F., Ferrini, F., & Penco, U. 1995, ApJ, 443, 536

Gavilán, M., Buell, J. F., & Mollá, M. 2005, A&A, 432, 861

Gavilán, M., Mollá, M., & Buell, J. F. 2006, A&A, 450, 509

Gelato, S., Chernoff, D. F., & Wasserman, I. 1997, ApJ, 480, 115, arXiv:astro-ph/9607156

Gingold, R. A., & Monaghan, J. J. 1977, MNRAS, 181, 375

Giovanelli, R., Haynes, M. P., Herter, T., Vogt, N. P., Wegner, G., Salzer, J. J., da Costa, L. N., & Freudling, W. 1997, AJ, 113, 22, arXiv:astro-ph/9610117

Gnedin, N. Y. 1995, ApJS, 97, 231

Gnedin, N. Y., & Bertschinger, E. 1996, ApJ, 470, 115, arXiv:astro-ph/9602063

González-García, A. C., Oñorbe, J., Domínguez-Tenreiro, R., & Gómez-Flechoso, M. Á. 2009, A&A, 497, 35

Governato, F. et al. 2008, ArXiv e-prints, 0812.0379

Governato, F., Willman, B., Mayer, L., Brooks, A., Stinson, G., Valenzuela, O., Wadsley, J., & Quinn, T. 2007, MNRAS, 374, 1479, arXiv:astro-ph/0602351

Gurbatov, S. N., & Saichev, A. I. 1984, Radiofizika, 27, 456

Guzman, R., Lucey, J. R., & Bower, R. G. 1993, MNRAS, 265, 731

Harris, W. E., Harris, G. L. H., Layden, A. C., & Stetson, P. B. 2007, AJ, 134, 43

Heideman, M., Johnson, D., & Burrus, C. 1984, ASSP Magazine, IEEE, 1, 14

Hernquist, L., & Katz, N. 1989, ApJS, 70, 419

Hockney, R. W., & Eastwood, J. W. 1981, Computer Simulation Using Particles (New York: McGraw-Hill)

Hoffman, Y., & Ribak, E. 1991, ApJ, 380, L5

Holmberg, E. 1941, ApJ, 94, 385

Hoyle, F. 1948, MNRAS, 108, 372

Hu, Y., Cox, A., & Zwaenepoel, W. 2000, in ACM/IEEE 2000 Conference on Supercomputing, 33–33

Hu, Y., & Johnsson, S. 1999, Algorithms for Parallel Processing, 213

Hubble, E. 1929, Proceedings of the National Academy of Science, 15, 168

Hut, P., Makino, J., & McMillan, S. 1995, ApJ, 443, L93

Inutsuka, S.-I. 2002, Journal of Computational Physics, 179, 238, arXiv:astro-ph/0206401

Iwamoto, K., Brachwitz, F., Nomoto, K., Kishimoto, N., Umeda, H., Hix, W. R., & Thielemann, F.-K. 1999, ApJS, 125, 439

Jessop, C., Duncan, M., & Chau, W. Y. 1994, Journal of Computational Physics, 115, 339

Jungwiert, B., Carraro, G., & dalla Vecchia, C. 2004, Ap&SS, 289, 441

Jungwiert, B., Combes, F., & Palouš, J. 2001, A&A, 376, 85

Kang, H., Ostriker, J. P., Cen, R., Ryu, D., Hernquist, L., Evrard, A. E., Bryan, G. L., & Norman, M. L. 1994, ApJ, 430, 83, arXiv:astro-ph/9404014

Katz, N. 1992, ApJ, 391, 502

Katz, N., & Gunn, J. E. 1991, ApJ, 377, 365

Kaufmann, T., Mayer, L., Wadsley, J., Stadel, J., & Moore, B. 2007, MNRAS, 375, 53, arXiv:astro-ph/0601115

Kawata, D., & Gibson, B. K. 2003, MNRAS, 340, 908

Kay, S. T., Pearce, F. R., Frenk, C. S., & Jenkins, A. 2002, MNRAS, 330, 113, arXiv:astro-ph/0106462

Kennicutt, Jr., R. C. 1998, ApJ, 498, 541

Klein, R. I., Fisher, R. T., McKee, C. F., & Truelove, J. K. 1999, in Astrophysics and Space Science Library, Vol. 240, Numerical Astrophysics, ed. S. M. Miyama, K. Tomisaka, & T. Hanawa, 131–+

Klessen, R. S., & Lin, D. N. 2003, Phys. Rev. E, 67, 046311

Knebe, A., Green, A., & Binney, J. 2001, MNRAS, 325, 845, arXiv:astro-ph/0103503

Knebe, A., Kravtsov, A. V., Gottlöber, S., & Klypin, A. A. 2000, MNRAS, 317, 630, arXiv:astro-ph/9912257

Knollmann, S. R., & Knebe, A. 2009, ApJS, 182, 608, 0904.3662

Kobayashi, C. 2004, MNRAS, 347, 740

Kobayashi, C., Springel, V., & White, S. D. M. 2007, MNRAS, 376, 1465

Kokubo, E., Yoshinaga, K., & Makino, J. 1998, MNRAS, 297, 1067

Kolb, E. W., Marra, V., & Matarrese, S. 2008, Phys. Rev. D, 78, 103002, 0807.0401

Komatsu, E. et al. 2009, ApJS, 180, 330, 0803.0547

Kravtsov, A. V. 1999, PhD thesis, AA(NEW MEXICO STATE UNIVERSITY)

Kravtsov, A. V., Klypin, A. A., & Khokhlov, A. M. 1997, ApJS, 111, 73, arXiv:astro-ph/9701195

Kroupa, P. 1998, MNRAS, 298, 231

Kuntschner, H., Ziegler, B. L., Sharples, R. M., Worthey, G., & Fricke, K. J. 2002, A&A, 395, 761

Lacey, C. G., & Fall, S. M. 1983, MNRAS, 204, 791

——. 1985, ApJ, 290, 154

Larsen, S. S., Brodie, J. P., Beasley, M. A., & Forbes, D. A. 2002, AJ, 124, 828

Larson, R. B. 1969, MNRAS, 145, 405

Lemaître, G. 1927, in Annales de la Société scientifique de Bruxelles, série A, XLVII

Leveque, R. J. 1992, Numerical Methods for Conservation Laws (Basel: Birkhäuser-Verlag)

Li, K. C. 1991, Journ. Amer. Stat. Assoc., 86, 316

Li, Y., Mac Low, M., & Klessen, R. S. 2005a, ApJ, 620, L19, arXiv:astro-ph/0407247

——. 2005b, ApJ, 626, 823, arXiv:astro-ph/0501022

Lia, C., & Carraro, G. 2001, Ap&SS, 276, 1049, arXiv:astro-ph/9904006

Lia, C., Portinari, L., & Carraro, G. 2002, MNRAS, 330, 821

Löf, H., & Holmgren, S. 2005, in ICS '05: Proceedings of the 19th annual international conference on Supercomputing (New York, NY, USA: ACM), 387–392

Lucy, L. B. 1977, AJ, 82, 1013

Lynden-Bell, D. 1975, Vistas in Astronomy, 19, 299

Madau, P., Diemand, J., & Kuhlen, M. 2008, ApJ, 679, 1260, 0802.2265

Maio, U., Dolag, K., Ciardi, B., & Tornatore, L. 2007, MNRAS, 379, 963, 0704.2186

Makino, J., Taiji, M., Ebisuzaki, T., & Sugimoto, D. 1997, ApJ, 480, 432

Mannheim, P. D. 2006, Progress in Particle and Nuclear Physics, 56, 340, arXiv:astro-ph/0505266

Marigo, P. 2001, A&A, 370, 194

Marri, S., & White, S. D. M. 2003, MNRAS, 345, 561, arXiv:astro-ph/0207448

Martin, C. L., & Kennicutt, Jr., R. C. 2001, ApJ, 555, 301, arXiv:astro-ph/0103181

Martínez-Serrano, F. J., Serna, A., Doménech-Moral, M., & Domínguez-Tenreiro, R. 2009, ArXiv e-prints, 0906.1118

Martínez-Serrano, F. J., Serna, A., Domínguez-Tenreiro, R., & Mollá, M. 2008, MNRAS, 388, 39, 0804.3766

Matteucci, F., & Francois, P. 1989, MNRAS, 239, 885

Matteucci, F., & Tornambe, A. 1987, A&A, 185, 51

Mellor-Crummey, J., Whalley, D., & Kennedy, K. 2001, International Journal of Parallel Programming, 29, 217

Merlin, E., & Chiosi, C. 2007, A&A, 473, 733, arXiv:0706.3308

Merz, H., Pen, U.-L., & Trac, H. 2005, New Astronomy, 10, 393, arXiv:astro-ph/0402443

Metzler, C. A., & Evrard, A. E. 1994, ApJ, 437, 564, arXiv:astro-ph/9309050

Milgrom, M. 2008, ArXiv e-prints, 0801.3133

Mollá, M., & Díaz, A. I. 2005, MNRAS, 358, 521

Molla, M., Ferrini, F., & Diaz, A. I. 1996, ApJ, 466, 668

Mollá, M., Vílchez, J. M., Gavilán, M., & Díaz, A. I. 2006, MNRAS, 372, 1069

Monaghan, J. J. 1992, ARA&A, 30, 543

——. 1997, Journal of Computational Physics, 136, 298

——. 2005, Reports of Progress in Physics, 68, 1703

Monaghan, J. J., & Gingold, R. A. 1983, Journal of Computational Physics, 52, 374

Moore, D. 2000, Hilbert Curve Generator, "http://ild-fa07.googlecode.com/svn/trunk/a3/src/hilbert.c"

Moore, G. E. 1965, Electronics, 38, 114

Mosconi, M. B., Tissera, P. B., Lambas, D. G., & Cora, S. A. 2001, MNRAS, 325, 34

Mouhcine, M., Gibson, B. K., Renda, A., & Kawata, D. 2008, A&A, 486, 711

Nakasato, N., Mori, M., & Nomoto, K. 1997, ApJ, 484, 608, arXiv:astro-ph/9704029

Navarro, J. F., & White, S. D. M. 1993, MNRAS, 265, 271

Nelson, R. P., & Papaloizou, J. C. B. 1993, MNRAS, 265, 905

——. 1994, MNRAS, 270, 1, arXiv:astro-ph/9406053

Nikolopoulos, D. S., Artiaga, E., Ayguadé, E., & Labarta, J. 2003, Sci. Program., 11, 143

Nikolopoulos, D. S., Papatheodorou, T. S., Polychronopoulos, C. D., Labarta, J., & Ayguadé, E. 2000, Parallel Processing, International Conference on, 0, 95

Norman, M. L., & Bryan, G. L. 1999, in Astrophysics and Space Science Library, Vol. 240, Numerical Astrophysics, ed. S. M. Miyama, K. Tomisaka, & T. Hanawa, 19–+

Oñorbe, J. 2009, PhD thesis, Universidad Autónoma de Madrid

Oñorbe, J., Domínguez-Tenreiro, R., Sáiz, A., Artal, H., & Serna, A. 2006, MNRAS, 373, 503, arXiv:astro-ph/0609499

Oñorbe, J., Domínguez-Tenreiro, R., Sáiz, A., & Serna, A. 2007, MNRAS, 376, 39, arXiv:astro-ph/0612732

Oñorbe, J., Domínguez-Tenreiro, R., Sáiz, A., Serna, A., & Artal, H. 2005, ApJ, 632, L57, arXiv:astro-ph/0511533

Okamoto, T., Eke, V. R., Frenk, C. S., & Jenkins, A. 2005, MNRAS, 363, 1299, arXiv:astro-ph/0503676

Oppenheimer, B. D., & Davé, R. 2006, MNRAS, 373, 1265, arXiv:astro-ph/0605651

O'Shea, B. W., Bryan, G., Bordner, J., Norman, M. L., Abel, T., Harkness, R., & Kritsuk, A. 2004, ArXiv Astrophysics e-prints, arXiv:astro-ph/0403044

Ostriker, J. P., & Peebles, P. J. E. 1973, ApJ, 186, 467

Pagel, B. E. J. 1997, Nucleosynthesis and Chemical Evolution of Galaxies (Nucleosynthesis and Chemical Evolution of Galaxies, by Bernard E. J. Pagel, pp. 392. ISBN 0521550610. Cambridge, UK: Cambridge University Press, October 1997.)

Pagel, B. E. J., & Patchett, B. E. 1975, MNRAS, 172, 13

Peacock, J. A. et al. 2001, Nature, 410, 169, arXiv:astro-ph/0103143

Pearce, F. R., & Couchman, H. M. P. 1997, New Astronomy, 2, 411, arXiv:astro-ph/9703183

Peebles, P. J. E., & Groth, E. J. 1976, A&A, 53, 131

Pen, U.-L. 1995, ApJS, 100, 269

Penzias, A. A., & Wilson, R. W. 1965, ApJ, 142, 419

Pérez, I. 2004, A&A, 427, L17, arXiv:astro-ph/0410250

Perlmutter, S. et al. 1999, ApJ, 517, 565, arXiv:astro-ph/9812133

Persic, M., Salucci, P., & Stel, F. 1996, MNRAS, 281, 27

Pfrommer, C., Springel, V., Enßlin, T. A., & Jubelgas, M. 2006, MNRAS, 367, 113, arXiv:astro-ph/0603483

Piontek, F., & Steinmetz, M. 2009, ArXiv e-prints, 0909.4167

Pohlen, M., Dettmar, R.-J., Lütticke, R., & Aronica, G. 2002, A&A, 392, 807

Pohlen, M., & Trujillo, I. 2006, A&A, 454, 759, arXiv:astro-ph/0603682

Pohlen, M., Zaroubi, S., Peletier, R. F., & Dettmar, R.-J. 2007, MNRAS, 378, 594, arXiv:astro-ph/0703768

Portinari, L., Chiosi, C., & Bressan, A. 1998, A&A, 334, 505

Power, C., & Knebe, A. 2006, MNRAS, 370, 691, arXiv:astro-ph/0512281

Press, W. H., & Schechter, P. 1974, ApJ, 187, 425

Pringle, G. J., Booth, S. P., Couchman, H. M. P., Pearce, F. R., & Simpson, A. D. 2001, in Proceedings of the 8th European PVM/MPI Users' Group Meeting on Recent Advances in Parallel Virtual Machine and Message Passing Interface (London, UK: Springer-Verlag), 360–369

Prunet, S., Pichon, C., Aubert, D., Pogosyan, D., Teyssier, R., & Gottloeber, S. 2008, ApJS, 178, 179, 0804.3536

Puzia, T. H., Kissler-Patig, M., Thomas, D., Maraston, C., Saglia, R. P., Bender, R., Goudfrooij, P., & Hempel, M. 2005, A&A, 439, 997

Quinlan, G. D., & Tremaine, S. 1990, AJ, 100, 1694

Quinn, T., Katz, N., Stadel, J., & Lake, G. 1997, ArXiv Astrophysics e-prints, arXiv:astro-ph/9710043

Raiteri, C. M., Villata, M., & Navarro, J. F. 1996, A&A, 315, 105

Reetz, J. 1999, Ap&SS, 265, 171

Riess, A. G. et al. 1998, AJ, 116, 1009, arXiv:astro-ph/9805201

Romeo, A. D., Portinari, L., & Sommer-Larsen, J. 2005, MNRAS, 361, 983

Romeo, A. D., Sommer-Larsen, J., Portinari, L., & Antonuccio-Delogu, V. 2006, MNRAS, 371, 548

Roškar, R., Debattista, V. P., Quinn, T. R., Stinson, G. S., & Wadsley, J. 2008a, ApJ, 684, L79, 0808.0206

Roškar, R., Debattista, V. P., Stinson, G. S., Quinn, T. R., Kaufmann, T., & Wadsley, J. 2008b, ApJ, 675, L65, 0710.5523

Ruiz-Lapuente, P., Blinnikov, S., Canal, R., Mendez, J., Sorokina, E., Visco, A., & Walton, N. 2000, Memorie della Societa Astronomica Italiana, 71, 435

Ryu, D., Vishniac, E. T., & Chiang, W.-H. 1990, ApJ, 354, 389

Sáiz, A. 2003, PhD thesis, Universidad Autónoma de Madrid

Sáiz, A., Domínguez-Tenreiro, R., & Serna, A. 2002, Ap&SS, 281, 309

——. 2003, Ap&SS, 284, 411

——. 2004, ApJ, 601, L131, arXiv:astro-ph/0403629

Salpeter, E. E. 1955, ApJ, 121, 161

Sánchez-Blázquez, P., Courty, S., Gibson, B., & Brook, C. 2009, ArXiv e-prints, 0905.4579

Sandage, A. 1968, ApJ, 152, L149+

Sansom, A. E., Peace, G., & Dodd, M. 1994, MNRAS, 271, 39

Scannapieco, C., Tissera, P. B., White, S. D. M., & Springel, V. 2005, MNRAS, 364, 552

——. 2008, MNRAS, 389, 1137, 0804.3795

Schaller, G., Schaerer, D., Meynet, G., & Maeder, A. 1992, A&AS, 96, 269

Schmidt, M. 1959, ApJ, 129, 243

——. 1963, ApJ, 137, 758

Schurer, A. 2009, PhD thesis, SISSA

Scott, D. W. 1992, Multivariate Density Estimation (Multivariate Density Estimation, Wiley, New York, 1992)

Semelin, B., & Combes, F. 2002, A&A, 388, 826, arXiv:astro-ph/0204240

Serna, A., Domínguez-Tenreiro, R., & Sáiz, A. 2003, ApJ, 597, 878

Shandarin, S. F., & Sunyaev, R. A. 2009, A&A, 500, 19

Shapiro, P. R., Martel, H., Villumsen, J. V., & Owen, J. M. 1996, ApJS, 103, 269

Shapiro, P. R., & Struck-Marcell, C. 1985, ApJS, 57, 205

Shapiro, P. R., Struck-Marcell, C., & Melott, A. L. 1983, ApJ, 275, 413

Shen, S., Mo, H. J., White, S. D. M., Blanton, M. R., Kauffmann, G., Voges, W., Brinkmann, J., & Csabai, I. 2003, MNRAS, 343, 978, arXiv:astro-ph/0301527

Shirokov, A. V. 2005, PhD thesis, Massachusetts Institute of Technology, Cambridge MA

Silk, J. 2001, MNRAS, 324, 313

Silva, L., Granato, G. L., Bressan, A., & Danese, L. 1998, ApJ, 509, 103

Sirko, E. 2005, ApJ, 634, 728, arXiv:astro-ph/0503106

Smith, S. 1936, ApJ, 83, 23

Smoot, G. F. et al. 1992, ApJ, 396, L1

Sommer-Larsen, J., Gelato, S., & Vedel, H. 1999, ApJ, 519, 501, arXiv:astro-ph/9801094

Sommer-Larsen, J., Götz, M., & Portinari, L. 2003, ApJ, 596, 47, arXiv:astro-ph/0204366

Sommer-Larsen, J., Romeo, A. D., & Portinari, L. 2005, MNRAS, 357, 478

Sommer-Larsen, J., & Yoshii, Y. 1989, MNRAS, 238, 133

Sotiriou, T. P., & Faraoni, V. 2008, ArXiv e-prints, 0805.1726

Springel, V. 2005, MNRAS, 364, 1105

——. 2009, ArXiv e-prints, 0901.4107

Springel, V., & Hernquist, L. 2002, MNRAS, 333, 649, arXiv:astro-ph/0111016

——. 2003, MNRAS, 339, 289, arXiv:astro-ph/0206393

Springob, C. M., Masters, K. L., Haynes, M. P., Giovanelli, R., & Marinoni, C. 2007, ApJS, 172, 599

Steinmetz, M., & Muller, E. 1994, A&A, 281, L97

——. 1995, MNRAS, 276, 549

Stinson, G., Seth, A., Katz, N., Wadsley, J., Governato, F., & Quinn, T. 2006, MNRAS, 373, 1074, arXiv:astro-ph/0602350

Suisalu, I., & Saar, E. 1995, MNRAS, 274, 287, arXiv:astro-ph/9412043

Sutherland, R. S., & Dopita, M. A. 1993, ApJS, 88, 253

Talbot, Jr., R. J., & Arnett, W. D. 1973, ApJ, 186, 51

Tasker, E. J., Brunino, R., Mitchell, N. L., Michielsen, D., Hopton, S., Pearce, F. R., Bryan, G. L., & Theuns, T. 2008, MNRAS, 390, 1267, 0808.1844

Tassis, K., Kravtsov, A. V., & Gnedin, N. Y. 2008, ApJ, 672, 888

Taylor, G. 1921, Proc. Lond. Math. Soc, 20, 196

Teyssier, R. 2002, A&A, 385, 337, arXiv:astro-ph/0111367

Thacker, R. 2003, in Proceedings of the 17th Annual International Symposium on High Performance Computing Systems and Applications and the OSCAR Symposium: May 11-14, 2003, Sherbrooke, Quebec, Canada, NRC Research Press, 23

Thacker, R. J., & Couchman, H. M. P. 2001, ApJ, 555, L17, arXiv:astro-ph/0106060

——. 2006, Computer Physics Communications, 174, 540, arXiv:astro-ph/0512030

Thomas, D., Maraston, C., Bender, R., & Mendes de Oliveira, C. 2005, ApJ, 621, 673

Thomas, P. A., & Couchman, H. M. P. 1992, MNRAS, 257, 11

Timmes, F. X., Woosley, S. E., & Weaver, T. A. 1995, ApJS, 98, 617

Tinsley, B. M. 1980, Fundamentals of Cosmic Physics, 5, 287

Tornatore, L., Borgani, S., Dolag, K., & Matteucci, F. 2007, MNRAS, 382, 1050, 0705.1921

Trujillo, I., & Pohlen, M. 2005, ApJ, 630, L17, arXiv:astro-ph/0507533

Valle, G., Ferrini, F., Galli, D., & Shore, S. N. 2002, ApJ, 566, 252

van den Bergh, S. 1999, PASP, 111, 657, arXiv:astro-ph/9904251

van den Hoek, L. B., & Groenewegen, M. A. T. 1997, A&A Supl.Series, 123, 305

van der Kruit, P. C. 1988, A&A, 192, 117

——. 2007, A&A, 466, 883, arXiv:astro-ph/0702486

Vergassola, M., Dubrulle, B., Frisch, U., & Noullez, A. 1994, A&A, 289, 325

von Hoerner, S. 1960, Zeitschrift fur Astrophysik, 50, 184

——. 1963, Zeitschrift fur Astrophysik, 57, 47

Wada, K., & Norman, C. A. 2001, ApJ, 547, 172

——. 2007, ApJ, 660, 276, arXiv:astro-ph/0701595

Wadsley, J. W., Stadel, J., & Quinn, T. 2004, New Astronomy, 9, 137, arXiv:astro-ph/0303521

Weisberg, S. 2002, Journ. Statistical Software, 7

Wetzstein, M., Nelson, A. F., Naab, T., & Burkert, A. 2008, ArXiv e-prints, 0802.4245

——. 2009, ApJS, 184, 298, 0802.4245

Wiersma, R. P. C., Schaye, J., & Smith, B. D. 2009a, MNRAS, 393, 99, 0807.3748

Wiersma, R. P. C., Schaye, J., Theuns, T., Dalla Vecchia, C., & Tornatore, L. 2009b, MNRAS, 399, 574, 0902.1535

Woosley, S. E., & Weaver, T. A. 1995, ApJS, 101, 181

Worthey, G. 1994, ApJS, 95, 107

Worthey, G., Faber, S. M., & Gonzalez, J. J. 1992, ApJ, 398, 69

Yepes, G., Kates, R., Khokhlov, A., & Klypin, A. 1997, MNRAS, 284, 235, arXiv:astro-ph/9605182

Yoshikawa, K., & Fukushige, T. 2005, PASJ, 57, 849, arXiv:astro-ph/0504095

Yuan, W., Centrella, J. M., & Norman, M. L. 1991, ApJ, 376, L29

Zel'dovich, Y. B. 1970, A&A, 5, 84

Zwicky, F. 1933, Helvetica Physica Acta, 6, 110